

# Turbulent Particle Transport in H-mode Plasmas on DIII-D

Xin Wang

Williamsburg, Virginia

Master of Science, College of William and Mary, 2013  
Bachelor of Science, University of Science and Technology of China, 2012

A Dissertation presented to the Graduate Faculty  
of the College of William and Mary in Candidacy for the Degree of  
Doctor of Philosophy

Department of Physics

The College of William and Mary  
August 2016

©2016  
Xin Wang  
All rights reserved.

## APPROVAL PAGE

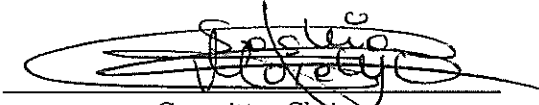
This Dissertation is submitted in partial fulfillment of  
the requirements for the degree of

Doctor of Philosophy



Xin Wang

Approved by the Committee, June, 2016

  
Committee Chair

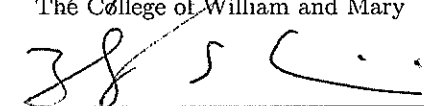
Research Assistant Professor Saskia Mordijk, Computer Science  
The College of William and Mary



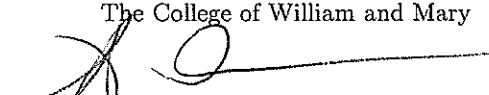
Professor George Vahala, Physics  
The College of William and Mary

  
Associate Professor Konstantinos Orginos, Physics

The College of William and Mary

  
Professor Shiwei Zhang, Physics

The College of William and Mary

  
Associate Professor Steven Shannon, External, Nuclear Engineering

North Carolina State University

## ABSTRACT

Particle transport is an important topic in plasma physics. It determines the density profile of a burning plasma within a tokamak – a magnetic confinement device. Microscopic turbulent particle transport is two orders of magnitude larger than other transport mechanisms for electrons and small ions. In order to confine a plasma in a tokamak with a core density that exceeds the fusion criteria [1], it is essential to study turbulent particle transport. This thesis investigates how different plasma parameters such as the toroidal rotation and microscopic instabilities affect turbulent particle transport in the DIII-D tokamak. First, we show how toroidal rotation can indirectly affect particle transport, through its contribution to the radial electric field and thus the  $E \times B$  shearing rate. The plasma discharge which has best confinement is the one whose  $E \times B$  shearing rate is larger than or at least similar to the growth rates that drive turbulent transport at the plasma edge. Second, for the first time on DIII-D, we observe a correlation between electron density gradient and instability mode frequency in the plasma core. We find that, when the turbulence is driven by the ion temperature gradient (ITG), the local density gradient increases as the absolute frequency of the dominant unstable mode decreases. Once the dominant unstable mode switches over to the trapped electron mode (TEM) regime, the local density gradient decreases again. As a result the density gradient reaches a maximum when the mode has zero frequency, which corresponds to the cross over from ITG to TEM. This correlation opens a new opportunity for future large burning plasma devices such as ITER to increase the core density by controlling the turbulence regime. Finally, we show that, in low density regime, a reduction in core density is observed when electron cyclotron heating (ECH) is applied. This reduction is not the result of a change in turbulence regime nor the result of a change in the density gradient in the core. Through detailed time-dependent experimental analysis, linear gyro-kinetic simulations, and comparison to turbulence measurements we show that this reduction in core density is the result of an increase in turbulence drive at the plasma edge.

## TABLE OF CONTENTS

Acknowledgments . . . . .	v
Dedication . . . . .	vii
List of Tables . . . . .	viii
List of Figures . . . . .	ix
CHAPTER	
1 Introduction . . . . .	2
1.1 Fusion energy . . . . .	2
1.2 Magnetic confinement and tokamak . . . . .	6
1.3 Structure of dissertation . . . . .	9
2 Particle transport in tokamak . . . . .	13
2.1 Classical and neoclassical particle transport . . . . .	14
2.1.1 Classical processes . . . . .	14
2.1.2 Neoclassical processes . . . . .	16
2.1.3 The need for anomalous processes . . . . .	20
2.2 Turbulence . . . . .	21
2.2.1 General introduction to turbulence . . . . .	21
2.2.2 $E \times B$ shear stabilization . . . . .	25
2.2.3 Types of turbulence: ITG & TEM . . . . .	28
2.3 Particle transport . . . . .	34
2.3.1 Effect on density profile . . . . .	34
2.3.2 The full transport matrix . . . . .	38

2.4	Summary	42
3	Methods	43
3.1	Theoretical simulation codes	43
3.1.1	ONETWO: One-and-a-half-dimensional transport code	44
3.1.2	TGLF: Quasi-linear kinetic code	48
3.2	Diagnostics	54
3.2.1	Thomson Scattering System	54
3.2.2	Reflectometer	56
3.2.3	Electron Cyclotron Emission	58
3.2.4	Charge Exchange Recombination	59
3.2.5	Beam Emission Spectroscopy	61
3.2.6	Doppler Backscattering	63
3.3	Summary	65
4	Turbulent particle transport as a function of toroidal rotation	66
4.1	Introduction	66
4.2	Experiment setup	69
4.3	Experimental particle transport changes	74
4.3.1	Particle flux	74
4.3.2	Perturbed transport coefficients	75
4.4	Turbulence and $E \times B$ shear	78
4.4.1	Role of toroidal rotation in deciding $E \times B$ shearing rate	78
4.4.2	Growth rate versus $E \times B$ shearing rate	80
4.4.3	Density fluctuations	83
4.5	Comparison with theory	84
4.5.1	Growth rate and frequency spectrum	84

4.5.2	Quasi-linear turbulent particle flux . . . . .	85
4.5.3	Density fluctuations versus growth rate . . . . .	87
4.6	Discussion . . . . .	88
4.7	Conclusion . . . . .	90
5	The determination of local density gradient by the local turbulence regime .	92
5.1	Introduction . . . . .	92
5.2	Experiment set-up . . . . .	95
5.3	Data fitting . . . . .	98
5.3.1	Exponential fitting . . . . .	98
5.3.2	Linear fitting . . . . .	100
5.3.3	Polynomial fitting . . . . .	101
5.4	Changes in electron density gradient . . . . .	103
5.4.1	2D plot of $R/L_n$ . . . . .	103
5.4.2	Dominant mode frequency . . . . .	104
5.4.3	Inverse density scale length versus unstable mode frequency . .	106
5.5	Changes in electron particle flux . . . . .	109
5.5.1	Time dependent electron flux . . . . .	109
5.5.2	$\Gamma_e$ versus unstable mode frequency . . . . .	111
5.6	Discussion . . . . .	112
5.7	Conclusion . . . . .	115
6	Understanding the ECH pump-out process on DIII-D . . . . .	116
6.1	Introduction . . . . .	116
6.2	Experimental measurement . . . . .	118
6.3	Density pump-out . . . . .	122
6.3.1	2D plot of $dn/dt$ and $dT_e/dt$ . . . . .	122

6.3.2	Change in turbulence drive . . . . .	124
6.3.3	Change in dominant unstable mode . . . . .	125
6.3.4	Density fluctuations . . . . .	127
6.4	Density pump-in . . . . .	128
6.4.1	Changes in Profiles . . . . .	128
6.4.2	Change in dominant mode . . . . .	130
6.5	Discussion . . . . .	131
6.6	Conclusion . . . . .	133
7	Conclusion and Outlook . . . . .	135
7.1	Conclusions . . . . .	135
7.2	Future work . . . . .	138
APPENDIX A		
	Frequently used physical symbols . . . . .	142
	Bibliography . . . . .	148
	Vita . . . . .	171

## ACKNOWLEDGMENTS

I have spent the past four years as a graduate student at the College of William and Mary. The Experience has been nothing short of amazing. I fell in love with Williamsburg – a beautiful, peaceful and historical town. On the campus, one can always find lots of gifted students and excellent scientists – many of whom have helped me a countless number of times along my journey. I would never have been able to finish my dissertation without their broad knowledge and extreme patience. Thus I would like to take this opportunity to thank all those who have ever offered their help to this work, and to apologize, if one of their names does not appear in this short acknowledgement; I am thankful to you, too.

First and foremost, I would like to express my deepest gratitude to my advisor, Dr. Saskia Mordijk, who enabled me to experience the research of plasma physics in the field and practical issues beyond the textbook, guided me academically and emotionally through the rough road to finish this thesis, patiently corrected my writing and financially supported my research. She taught me a vast variety of things, starting with how to think like a scientist. Real world research is never like doing a homework problem. Most of the time we are dealing with questions that nobody knows the answers to. It is only through numerous trying, motivated self-reflection, and rigorous validating that we may approach the possible solution. Understanding the importance of communication is another important lesson I learned from Saskia. I owe her a great debt for her continuous trust in me and tireless help to my work. Thank you Saskia.

Next I want to thank all my committee members, who guided me for the past several years. Thank you George Vahala for being my co-advisor in the physics department. I learned to appreciate the beauty of math-physics in your classes and I tried to use them in my work. You always pushed me to further understand the basics of plasma physics so that a solid foundation can be laid before I rushed to pursue an innovative result. Thank you Kostas Orginos and Shiwei Zhang for being my general committees, thesis readers, and an inspiration in many ways. I also need to thank Steven Shannon, who was willing to look over my thesis in his precious time and who drove three hours early in the morning to attend my defense.

I would also like to thank all my collaborators. I enjoyed working in the big DIII-D family. Everyone is so helpful and essential to this dissertation. Thank you Orso and Sterling for teaching me every details of using OMFIT, I appreciate your patience. Gary, your consistent help brought my understanding of the TGLF code and the underlying

physics to a new level. Many thanks to Lei, Max, Brian, Ted, George, and all the other people in the DIII-D diagnostic team, for answering all my stupid questions about the experimental measurement. And there are also a lot of other great people whom I was fortunate to meet during this journey, Rick, Chuck, Craig, Ed, Richard, Lothar, Francesca, Pad, and Keith. I cherish the moments I spent with you guys.

I also offer my sincere thanks to my friends and fellow officemates in the College of William and Mary. Thank you Dun, Guangzhi, Yang, Ji, Mi, Haowei, Guoyang, Lifu, Jie, Shaoyang, Deborah, and Yunhan, you were always to talk since I first came to US. There were numerous weekends we hung out together so that I would not be too homesick. Hope you all are doing great. Next, I would like to record my appreciation of the science soccer team: Martin, Rony, Marco, Charlie, Satrio, Matt, Yudis, Mario, Dachuan, Dylan. Winning two years in a row in the William and Mary soccer championship is one of the most glorious moments of my graduate school life. I would like to thank my mates: Dan, Scott, and Keith, with whom I shared an office cube. Thank you for laughing at my bad jokes. Armen, Chris, I know we were probably the only three graduate students studying plasma physics in the physics department. I enjoyed discussing research with you and wish you the very best for your graduation.

I am grateful for the constant support my parents give to me. Since I was a kid, my parents have given everything they can to enable me to chase my dreams, no matter what the result. What I have achieved so far, and whatever I will achieve in the future, it is all due to them.

Last but not the least, I want to thank my lovely girlfriend, Qi. Thank you for believing in me from the very beginning and for every effort you have devoted to make our relationship what it is today. Thank you for sending me greeting cards from everywhere you travelled, for baking me cookies, for knitting me warm scarf, and for taking an 11-hour train from New York to see me. Thank you for being a good listener when I expressed my frustrations with life as a PhD, for supporting me when I couldn't stand, and for pushing me when I was lazy and demotivated. I really could not have done this without you. Thank you for being my biggest fan, my best friend and the love of my life.

To Qi.

## LIST OF TABLES

2.1	Different directions of off-diagonal terms . . . . .	41
3.1	Diagnostics for different plasma parameters in tokamaks . . . . .	55
A.1	Physical symbols and their units . . . . .	142

## LIST OF FIGURES

1.1	US energy production . . . . .	3
1.2	Petroleum consumption . . . . .	4
1.3	Closed toroidal magnetic confinement . . . . .	7
1.4	Particles drifts under toroidal field . . . . .	8
1.5	Magnetic field lines in tokamak . . . . .	9
2.1	Classical cross-field transport . . . . .	14
2.2	Trapped ions in tokamaks . . . . .	17
2.3	Diffusion coefficient in Classical and Neoclassical transport . . . . .	18
2.4	Core density peaking under ICRF . . . . .	19
2.5	Fast camera imaging of turbulence in laboratory. . . . .	22
2.6	Turbulence eddies' change with corresponding growth rate . . . . .	24
2.7	$E \times B$ shear flow . . . . .	26
2.8	How shear flow tear apart turbulence eddies . . . . .	27
2.9	Fast camera imaging of turbulence suppression by shear flow. . . . .	28
2.10	Pictures of instabilities . . . . .	29
2.11	Summary of ITG and TEM turbulence . . . . .	34
2.12	Local density profile . . . . .	36
3.1	Magnetic flux contours . . . . .	44
3.2	ONETWO calculated source and particle flux. . . . .	47

3.3	Work flow of TGLF code.	54
3.4	Reflectometer cut-off layer	57
3.5	Schematic of CER set up.	61
3.6	Bragg scattering	64
4.1	Geometry of the DIII-D neutral beam injection system.	68
4.2	Time evolution of three DIII-D H-mode discharges	69
4.3	Density profiles at the edge before and after ELM.	70
4.4	Experimental fitted profiles and their inverse gradients	72
4.5	Frequency of the most unstable mode for $0 < k_\theta \rho_s < 1$ by TGLF.	73
4.6	Particle flux and effective diffusion coefficient profiles	75
4.7	Density evolution through two edge gas puffs.	76
4.8	Perturbative transport measurement	78
4.9	Components of radial electric field for the co-current discharge	80
4.10	Correlation plot	81
4.11	$E \times B$ shearing rates	82
4.12	$E \times B$ shearing rates versus the maximum growth rates	82
4.13	Density fluctuation profiles	84
4.14	Frequency and growth rate spectrum	85
4.15	Particle flux profiles for the 3 discharges.	86
4.16	Linear growth rate profiles	87
5.1	Time evolution figures	96
5.2	Measured electron density data.	97

5.3	$dn/dt$ calculated by raw data.	98
5.4	Exponential fitting of normalized electron density	100
5.5	Linear fitting of normalized electron density	101
5.6	Polynomial fitting of normalized electron density	102
5.7	Polynomial fitting quality	103
5.8	Polynomial fitting of electron density	104
5.9	2D plot of $R/L_n$	105
5.10	Frequency of the most unstable mode	106
5.11	Electron density gradient vs the mode frequency	107
5.12	Electron density gradient vs the mode frequency	108
5.13	Electron flux at different time slices.	109
5.14	2D plot of the time dependent electron flux	111
5.15	Electron particle flux vs the mode frequency	112
5.16	Effective diffusion coefficient vs the mode frequency	113
6.1	Density profiles.	119
6.2	Temperature and rotation profiles.	120
6.3	Thomson scattering data <i>vs</i> reflectometer data	121
6.4	Density and temperature change.	123
6.5	Changes in gradient drive.	124
6.6	Growth rate and frequency profiles.	125
6.7	Time evolution of $dn/dt$ , $\gamma$ and $\omega$	126
6.8	Time evolution of density fluctuation measurement.	127
6.9	Density profiles in pump-in process.	129

6.10	Temperature and rotation profiles in pump-in.	130
6.11	Growth rate and frequency profiles in pump-in.	130
6.12	Growth rate and frequency spectrum.	132

## TURBULENT PARTICLE TRANSPORT IN H-MODE PLASMAS ON DIII-D

# CHAPTER 1

## Introduction

### 1.1 Fusion energy

The evolution of human society is always accompanied by the development and need for new energy. The use of fire, the development of the steam engine, and the application of electric and nuclear power represent four important stages in human history. Particularly, the rise of industrial societies is based on the ability to explore and exploit fossil fuel on a larger scale, with increasing efficiency, and in convenient ways. Without this energy source, we cannot imagine products like cars, aeroplanes, and computers, which are indispensable in modern life. As shown in Figure 1.1, in 2015, about 90% of US energy production comes from fossil fuels and nuclear power while fossil fuels alone take 80% of the total energy production (Data from U. S. Energy Information Administration [2]). However, one large problem with the massive use of carbohydrates fuel is that it produces a large amount of greenhouse gases, which is the major cause of global climate change [3]. According to the statistics from the Carbon Dioxide Information Analysis Center (CDIAC, Oak Ridge National Lab) [4], global carbon emissions have increased by 500% since 1950.

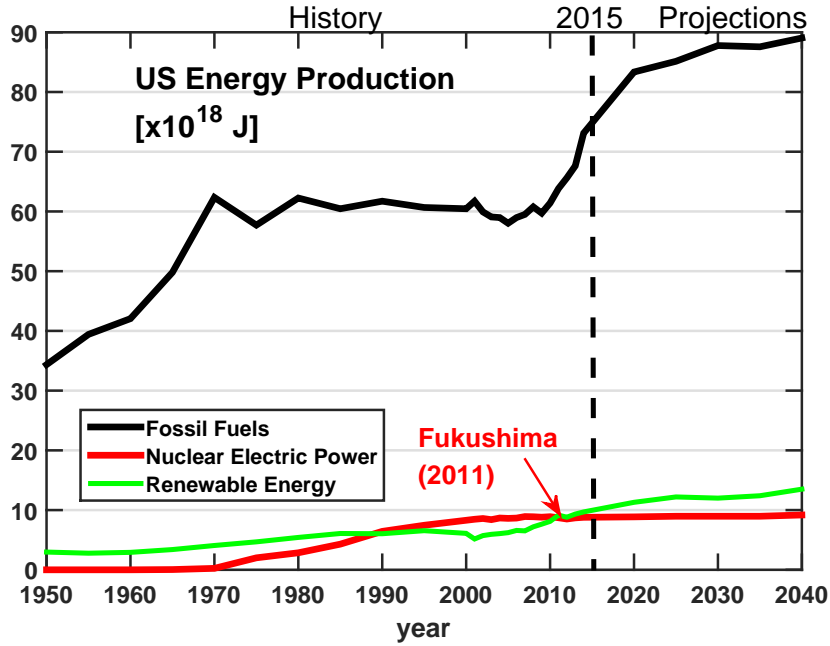


FIG. 1.1: US energy production from 1950 in history to 2040 by anticipation. (Data from U. S. Energy Information Administration [2])

Additionally, in 2014, fossil fuel emissions (including cement production) accounted for about 91% of total  $CO_2$  emissions from all human sources.

Moreover, a high quality of life requires a high use of energy [5]. As more and more developing countries such as China and India try to improve their life quality to match the levels of developed countries, they will need an energy increase of at least 200% in the 21st century [5], providing that the population of developing countries is 6 times larger than the developed countries. We can see from Figure 1.2, the Organization for Economic Co-operation and Development (OECD) (most of which are high-income developed countries) predicts an almost stable consumption in petroleum for developed countries. The requirement of liquid fuel from non-OECD countries will increase more than 200% in the next 25 years (Data from U. S. Energy Information Administration [6]). Considering that the current consumption speed of fossil fuels has far exceeded its reproduction rate, a global

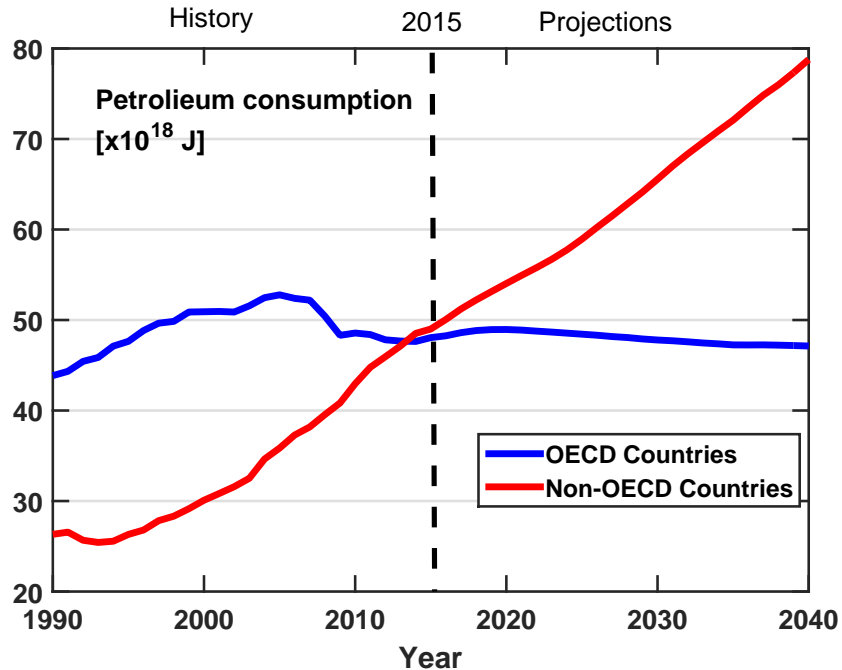


FIG. 1.2: Petroleum consumption from OECD countries (blue) and Non-OECD countries between 1990 and 2040. (Data from U. S. Energy Information Administration [6])

energy crisis will arise from the energy demands of those developing countries somewhere in the foreseeable future.

On the other hand, nuclear fission has proven to be a reliable, carbon-free energy source that can be sustained for centuries based on availability of fissionable materials on earth. The taken share of fission energy in US energy production has been climbing since the 1970s. However, the nuclear disaster in Fukushima [7] (where the tsunami-caused equipment failure led to three nuclear meltdowns and the release of radioactive material) in 2011 brought tremendous fear of the nuclear waste and radiation to the public. Considering the fact that the US has not authorized to build any new nuclear power plant for 34 years since the Three Mile Island event in 1974 [8, 9], this new round of fear after Fukushima will result in more uncertainties in the political future for the nuclear power industry in the United States.

To sum up, it is needed to find an energy source that is environmentally friendly (free of greenhouse gases), economically sustainable (fulfil the increasing energy demand), and operationally safe (less or no nuclear waste).

Nuclear fusion is one of the possible solutions toward future alternative energy systems. For billions of years, fusion reactions have powered the sun. At exceedingly high temperatures such as those in the core of the sun, light nuclei, usually hydrogen isotopes, can collide with each other so that heavier nuclear species are formed and a large amount of their binding energy is released. This is referred to as fusion. Nuclear fusion has two major advantages. The first is clean. It produces no greenhouse gas and has a limited amount of nuclear waste when compared with the fission reaction. The half-life cycle of the fusion by-product is also much shorter than all the current nuclear fission products [10, 11]. Secondly, on our planet, there are a lot more fuels for the fusion reaction than the fission. Both the ocean and the earth provide almost unlimited fuel supply of hydrogen isotopes. For example, it has been recognized that among possible fusion reactions, the most practical one is the Deuterium and Tritium reaction:



since the  $D + T$  reaction has a larger reaction cross section and releases more energy than other fusion reactions such as  $D + D$  [12] (here  $n$  represents a neutron). There is a large amount of Deuterium in the ocean, specifically, in the surface sea water (i.e., upper 3 meters of ocean surface [13]). Every litre of sea water contains about 0.03g Deuterium on average [14]. This 0.03g Deuterium can release fusion energy which equals the energy released by burning 300 litres of gasoline [15]. By comparison, Tritium is radioactive and

is actually non-existent in nature (it has a decay half-life of only 12.3 years). However, we can still use the fission reaction with lithium as an additional raw material to breed enough tritium:



Here  $n$  represents neutron. Therefore, nuclear fusion has become an ideal future energy candidate since the 1950s.

## 1.2 Magnetic confinement and tokamak

Although it is not difficult to obtain enough fuel for fusion energy production, the temperatures needed to trigger the reaction are extremely high. The particles need sufficiently large kinetic energy to overcome the Coulomb barrier before the nuclear force can dominate. Even for the  $D + T$  reaction which has the minimum temperature requirement among all the fusion reactions, it is still necessary to reach 10Kev, which is around the order of  $10^8 K$  [12]. At such high temperatures, the atoms are stripped of their electrons and form an ionized cloud of particles called “plasma”. A plasma can be loosely defined as an electrically neutral medium of unbounded positive and negative particles, which can be achieved by heating a gas to high temperatures [16, 17]. In addition to the required temperatures, the heated plasmas need to be sufficiently dense and these conditions needs to be maintained for a long enough period so that the fusion process can become self-sustained. J. D. Lawson quantized all the above requirements for the  $D + T$  reaction with Lawson Criteria [1] in 1957:

$$n\tau_E T > 3 \times 10^{21} m^{-3} KeVs \quad (1.4)$$

where  $n$ ,  $\tau_E$ ,  $T$  are the plasma density, the energy confinement time, and the plasma temperature respectively. Therefore, how to confine a heated plasma well is an essential problem which will determine the feasibility of fusion.

Currently, there are two promising ways in the laboratory to confine high temperature, high density plasmas. One is called inertial confinement [18] which uses a set of concentric laser beams or X-rays to heat a target pellet. As the outer layer of the pellet ablates off, the inner fusion fuels are compressed and thus a very high density is contained by the pellet's inertia to achieve the fusion burn. The other method is called magnetic confinement. It uses the Lorentz force which acts on ionized particles when they are crossing a magnetic field to confine the plasmas on a much longer time scale than the inertial confinement. Since ionized particles gyrate around a magnetic line while their gyration center moves along the field line, we can build a torus with self-closed toroidal field lines inside it (as shown in Figure 1.3). Thus particles following along the closed field lines can remain within the toroidal confinement chamber. The toroidal magnetic field  $B_\phi$  is generated by external

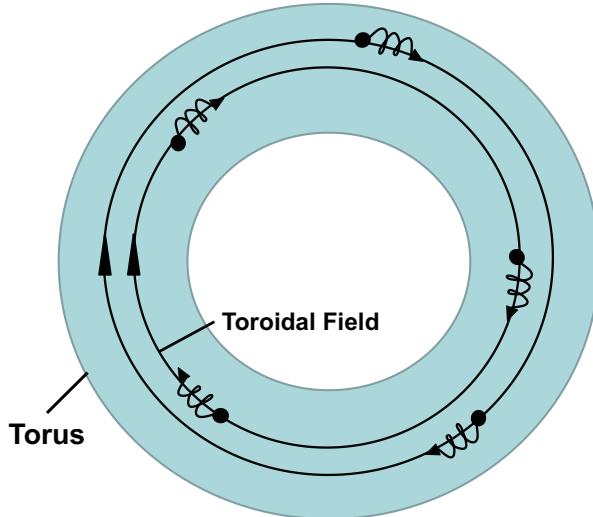


FIG. 1.3: Closed toroidal magnetic confinement .

coils which surround the vacuum vessel of the torus. However, only having a toroidal field results in poor confinement. There exists a vertical drift on those particles which spiral around the field lines. The drift is caused by the outward forces that result from gradients of the magnetic lines as well as its curvature and thus is called  $\nabla B$  and curvature drift respectively [12]. As shown in Figure 1.4's situation where the toroidal magnetic field

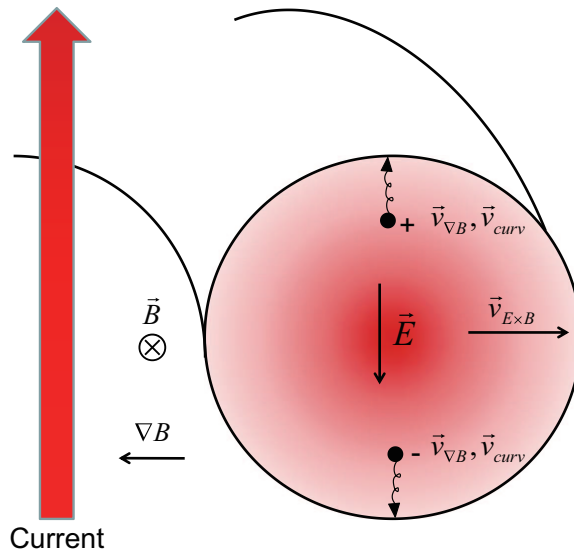


FIG. 1.4: Particles drifts under toroidal field : Vertical  $\nabla B$  and curvature drifts cause charge separation, which then leads to a radially outward  $E \times B$  drift of the plasma particles.

points inside the paper, the  $\nabla B$  drift  $\mathbf{v}_{\nabla B}$  and the curvature drift  $\mathbf{v}_{curv}$  are up for ions and down for electrons. These drifts result in charge separation which produces a downward electric field  $\mathbf{E}$ . The electric field can lead to a radially outward  $E \times B$  drift [17] that carries the plasma to the outer wall and thus breaks the confinement. To prevent the drift loss, we need to create another poloidal magnetic field which is produced by the toroidal plasma current. The poloidal field, although it is typically less than the toroidal field by an order of magnitude, can help to improve the confinement by continuing to bring these outer side drifting particles to the inner side of the 'donut'. The tokamak is one of the most

successful magnetic confinement techniques [12, 17]. It is a torus whose magnetic field,  $\mathbf{B}$ , consists of both poloidal and toroidal components,  $B_\theta$  and  $B_\phi$ , as shown in Figure 1.5. Therefore, the resultant total magnetic fields of tokamaks are helical, with the field lines wrapping around the torus both toroidally and poloidally, forming the nested magnetic flux surfaces within the vacuum vessel (Figure 1.5).

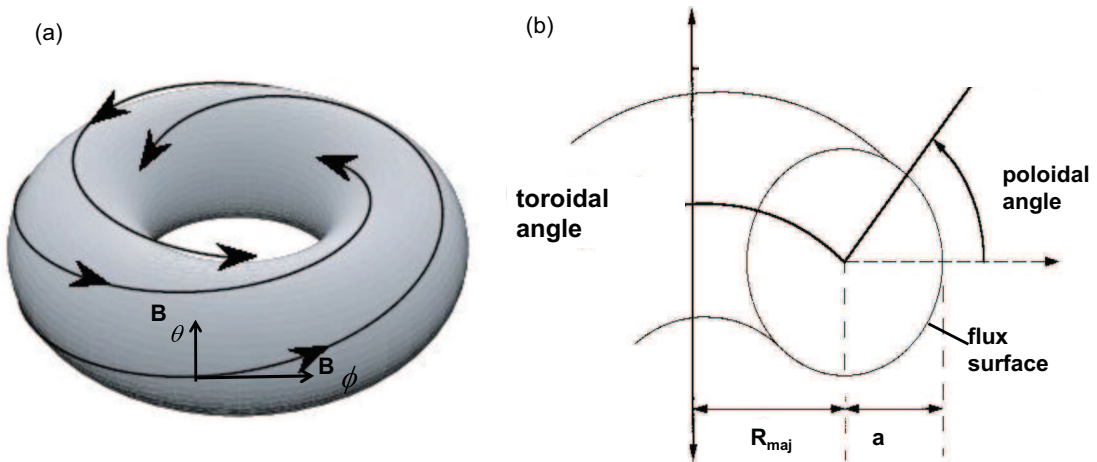


FIG. 1.5: Magnetic field lines in tokamak : There are toroidal direction as well as poloidal direction magnetic fields.

### 1.3 Structure of dissertation

This dissertation investigates how different plasma conditions such as toroidal rotation or instability types can affect the turbulent particle transport in tokamak plasmas. In Chapter 2, we first introduce the concepts of classical and neoclassical transport theories. However, these two theories predict much smaller transport coefficients than the experimental results when it comes to calculating the cross-field transport [17]. This discrepancy between experiment and theory is defined as anomalous transport. Anomalous transport is caused by turbulence and dominates radial transport in a tokamak. In section 2.2, We

describe some basic turbulence properties along with one of its suppression mechanisms through shear flow. Two types of turbulence (i.e., ion temperature gradient mode (ITG) and trapped electron mode (TEM)) are identified by their poloidal wavenumber. Different modes can affect the transport coefficients and thus result in different particle fluxes. Finally, the third section of Chapter 2 discuss how particle transport affects the plasma density profiles. We use a gyrokinetic expression to present the particle flux in the form of its diagonal and off-diagonal terms. The coefficient of each term is analysed so that a qualitative comparison between experiment and theory can be achieved.

Before proceeding to study how different plasma conditions affect turbulent particle transport, we will introduce two theoretical simulation tools as well as the essential diagnostics used in our research in Chapter 3. The first section describes two simulation codes, namely, ONETWO and TGLF. ONETWO solves the transport equations while TGLF solves the linear gyrokinetic equations and thus calculates the growth rates and frequencies of unstable modes in the plasma. The second section of this chapter covers the basic principles of several diagnostics. These diagnostics are used in our particle transport studies to provide experimental data as input to the simulations as well as validation for theoretical models.

In Chapter 4, the study of how controlled changes in toroidal rotation affect particle transport and confinement is presented. The toroidal rotation is altered using the co- and counter Neutral Beam Injection (NBI) in low collisionality H-mode plasmas on DIII-D [19] with dominant Electron Cyclotron Heating (ECH). We find that when the  $E \times B$  shear is less than the linear gyrokinetic growth rate for small wavenumber, which is observed in a balanced torque injected discharge, particle confinement is lower than in cases where the linear growth rate is smaller than the  $E \times B$  shear. In the co- and counter- injected

discharges the  $E \times B$  shear is larger or close to the linear growth rate and both configurations result in better particle confinement. In addition, we observe that the calculated quasi-linear particle flux using TGLF [20] does not agree with experimental observations. To measure particle transport, we use a small periodic perturbative gas puff from which we can extract the perturbed diffusion and inward pinch coefficients. This work is summarized in X. Wang et al. [21]

Next, in Chapter 5, we will introduce how the changes in turbulence characteristics result in changes in turbulent particle transport and thus different electron density profiles. That is, the change from ITG regime to TEM regime causes a change of inward to outward thermal-diffusive electron flux. In an H-mode experiment on DIII-D, the ECH power is modulated with a period of 500 ms on top of steady neutral beam heating. By fitting the density evolution during the ECH pulse, we find that the local density gradient in plasma core agrees with the theoretical gyro-kinetic predictions [22]. Gyro-kinetics predict that when the absolute frequency of the dominant unstable mode decreases in the ion temperature gradient (ITG) regime, local density peaking increases. Once the dominant mode switches over to the trapped electron mode (TEM) regime, the local peaking of the density decreases again, which means that the density gradient reaches a maximum right where the turbulence regime switches over from ITG to TEM. For the first time in DIII-D, we observe this correlation between the changes in density gradient and this change in frequency, in agreement with theoretical prediction [22] and experimental results on AUG [23]. We also find that the experimental particle flux (which is independent of the local gradients) shows a similar correlation. This is a clear indication that particle transport is dominated by changes in turbulence.

Beside the correlation between the electron density gradient and the mode frequency

in Chapter 5, we also observe an electron density pump-out immediately after applying the ECH pulses. In Chapter 6, we use the same fitted density and temperature data as in Chapter 5. We find that the strongest density reduction occurs outside mid-radius in the tokamak, while the initial increase in electron temperature occurs in the plasma core. So while, the ECH is added to the plasma core, the density pump-out originates at the plasma edge. Both the linear gyrokinetic analysis using TGLF [20] and the experimental measured density fluctuations show that the turbulence regime only switches to the trapped electron mode (TEM), after 150ms. So the onset of the density pump-out is not the result of a change in turbulence regime, which is what has been assumed in previous research [24]. The pump-out is the result of an increase in turbulence drive. In addition, when the ECH pulse is turned off, electron density gets “pumped in” from the plasma edge and then the turbulence changes back from TEM to ITG.

Chapter 7 will provide a final summary as well as future research directions.

# CHAPTER 2

## Particle transport in tokamak

Since fusion power scales with the plasma density squared [1], achieving a high central density in a reactor is of particular importance. In tokamaks, cross-field particle transport plays a significant role in deciding the density profiles. Cross-field transport can result in an outward particle loss or an inward particle pinch depending on different plasma parameters. Thus, to obtain a magnetically confined plasma whose core density peaks and exceeds the fusion criteria [1], it is essential to study particle transport within tokamaks. In this chapter, we start from classical and neoclassical collision theory in Section 2.1 to describe cross-field transport. However, these two theories predict smaller diffusion coefficients than the experimental measurements. Thus the importance of including turbulence-caused anomalous transport process is addressed. Next in Section 2.2, the basic properties of turbulence are introduced, along with one of its suppression mechanisms (via  $E \times B$  shear flow). Two types of turbulence (i.e., the ion temperature gradient (ITG) mode and the trapped electron mode (TEM)) are also described from the angle of their driven terms in this section. The last section, Section 2.3, reviews the recent literature on particle transport and its relation in determining density profiles in tokamaks. A full multi-channel transport

matrix will be given to describe both the diagonal and off-diagonal terms of the particle flux.

## 2.1 Classical and neoclassical particle transport

### 2.1.1 Classical processes

Confinement in a closed plasma system is limited by various forms of cross-field transport. Classical transport represents the minimum level of “leakiness” from a confinement system [12]. The underlying physical mechanism involved is binary Coulomb collision which causes the particles to step from one orbit centered on one magnetic surface to another orbit centered on a neighbouring magnetic surface, as shown in Figure 2.1 for a cylindrical system. The general collisional diffusion can be modelled as a random walk

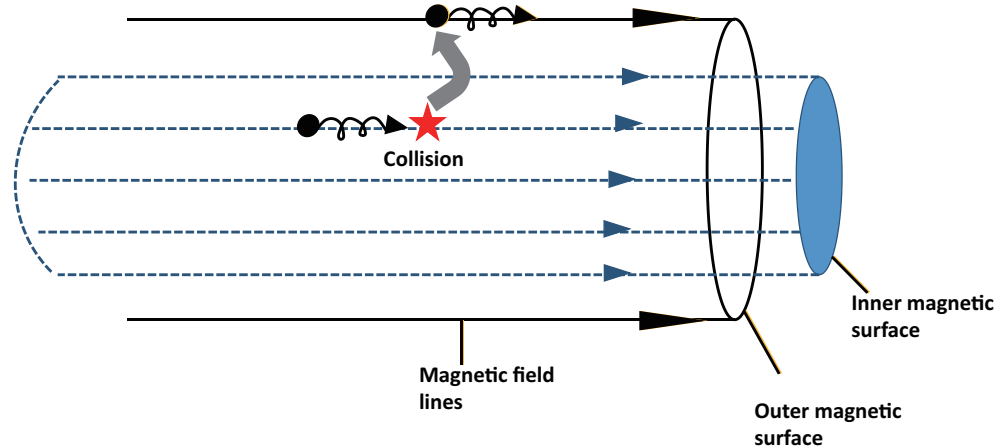


FIG. 2.1: Classical cross-field transport in a cylindrical system.

with a mean free path  $\Delta x$  and a characteristic time  $\tau$ . The diffusion coefficient  $D$  can be

expressed as [12]:

$$D = \frac{\Delta x^2}{\tau} \quad (2.1)$$

In a cylindrical magnetic field system, since a particle excurses from a magnetic surface on the order of its gyro-radius, the mean free path length should be the particle's gyro-radius  $\Delta x = \rho = \frac{mv_{\perp}}{eB}$ , and the characteristic time  $\tau = \frac{1}{\nu}$  is the inverse of the collisional scattering frequency  $\nu$ . Here,  $m$  is the particle mass,  $v_{\perp}$  is the perpendicular velocity to the magnetic field  $B$ ,  $e$  is the unit charge. Thus the diffusion coefficient given by classical transport for an electron-ion collision is:

$$D = \nu_{ei}\rho_e^2 \quad (2.2)$$

where

$$\nu_{ei} = \frac{e^4 n_i \ln \Lambda}{4\pi \epsilon_0^2 m_e^2 v_{th,e}^3} \quad [s^{-1}]$$

is the electron-ion collision frequency [25],  $e$  is electron charge,  $n_i$  is the ion density,  $m_e$  is the electron mass,  $v_{th,e} = \sqrt{\frac{2T_e}{m_e}}$  is the electron thermal velocity ( $T_e$  is the electron temperature),  $\epsilon_0$  the vacuum permittivity, and  $\ln \Lambda$  is the dimensionless plasma parameter defined by  $\Lambda = \frac{4}{3}\pi(\frac{\epsilon_0 T_e}{e^2 n_i})^{3/2}$  [25]. We only consider electron-ion collision, because the classical particle diffusion results from coulomb collisions. The conservation of angular momentum indicates that no shift in the center of mass occurs for like-particles and thus only unlike-particles collisions lead to particle diffusion, implying  $D^{electron} = D^{ion} = D$  [25]. As an example, if we use typical plasma parameters which are obtained in our experiments in the DIII-D tokamak [19] (detailed experiment set up will be introduced in Chapter 4 and Chapter 5). The plasma core electron temperature is around 4 Kev, core ion density  $n_i$  is about  $3 \times 10^{19} m^{-3}$ , and the toroidal magnetic field is  $B \approx 2T$ . Substituting these numbers into equation 2.2, we can estimate the classical transport diffusion coefficient to be of the order of  $10^{-4} \quad [m^2/s]$ .

### 2.1.2 Neoclassical processes

The classical theory was developed in a cylindrical system. However, for a toroidal geometry, the particle orbits can excursion away from a magnetic surface in a considerably larger step size than the gyro-radius. The cross-field transport which is caused by the inhomogeneity of the magnetic fields is called neoclassical transport [12]. In a tokamak, all particles gyrate in small circles along a magnetic field line and the center of this gyration orbit is called the guiding center. For most untrapped particles, the guiding center simply follows the field line around the torus, see Figure 1.5 (similar as in the classical picture). However, in a tokamak, the toroidal field  $B_\phi$  strength is proportional to  $1/R$ :

$$B_\phi(R) = \frac{B_0 R_0}{R} \quad (2.3)$$

where  $B_0$  is the magnetic field strength in the plasma center,  $R_0$  is the major radius, and  $R$  denotes length in the major radii. Thus  $B_\phi$  is larger on the inner side of the torus than the outer side. This causes the guiding center of some particles (trapped particles) to be reflected at a certain poloidal angle, similar to the dynamics in a magnetic mirror, see Figure 2.2. As a first approximation, an ion which has a parallel velocity of  $v_{\parallel} < \sqrt{\frac{r}{R}}v$  will be trapped. Thus the fraction of the trapped particles is  $f \approx \epsilon^{1/2}$ , here  $v$  is the total velocity and the inverse aspect ratio  $\epsilon = \frac{r}{R}$  ( $r$  and  $R$  as shown in Figure 2.2) [26]. As the trapped-particle guiding centers bounce back and forth along the field lines, they are subject to a drift  $\mathbf{v}_D$  arising from the inhomogeneity of the magnetic field (specifically the  $\nabla B$  and the curvature drift as we have discussed in Chapter 1). The drift directed in the vertical direction with the sign depending on the particle charge and magnetic field. The approximate magnitude of this drift is  $v_D \approx mcv^2/eBR$ . For ions, as shown in

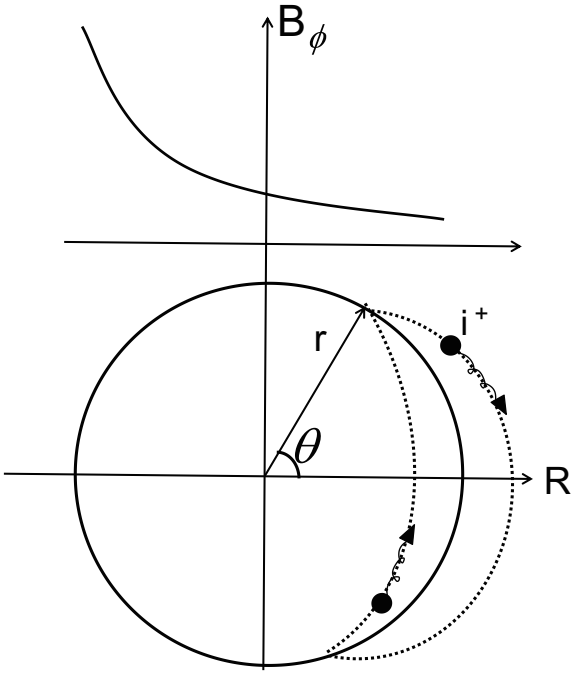


FIG. 2.2: Trapped ions in tokamaks go around a banana orbit in its poloidal projection.

Figure 2.2, at the top of the circular orbit, the vertical drift has an outward component in the radial direction, while at the bottom of the orbit it has an inward component in the radial direction. The result of this component of the drift is that the projection of the guiding center orbit has a “banana” shape in its trapped area, see Figure 2.2. Therefore, the cross-field diffusive step size of these trapped particles should be the banana orbit’s width  $\Delta_b \approx v_D \tau \approx (r/R)^{1/2} \rho_\theta$ , where  $\rho_\theta = mv/eB_\theta$  is ionized particle’s gyro-radius in the poloidal field. On the other hand, since only a small angular deflection is needed, the collisional scattering out of the trapped-particle region will take place with an effective frequency  $\nu_{eff} \approx \nu/\epsilon$ . Thus by the definition in equation 2.1, the diffusion coefficient involving a fraction of  $\epsilon^{1/2}$  trapped particles should be:

$$D_{NC} = \epsilon^{1/2} \nu_{eff} \Delta_b^2 \approx (r/R)^{1/2} \nu \rho_\theta^2 \approx (R/r)^{3/2} q^2 \nu \rho^2 \quad (2.4)$$

Where the safety factor is defined as  $q = \frac{rB_\phi}{RB_\theta}$  [25]. Equation 2.4 indicates that the neoclassical diffusion coefficient is a factor  $(R/r)^{3/2}q^2$  larger than the classical diffusion coefficient in equation 2.2. With our experimental parameters substituted, the calculated neoclassical diffusion coefficient is approximately two orders larger than the classical diffusion coefficient. Lastly, in a low collision frequency regime, a particle can trace out several banana orbits before colliding. However, when the collisionality (define as  $\nu^* = \nu q R / v_{th}$  where  $v_{th}$  is the thermal velocity) increases, collisions are too frequent to permit a trapped particle to complete its banana orbit. Thus both the step size and the collision frequency will be different. Historically, we sort the diffusive coefficients based on collisionality into three regimes, namely, Banana regime  $\nu^* < 1$ , Plateau regime  $1 < \nu^* < (R/r)^{3/2}$ , and Pfirsh-Schluter regime  $(R/r)^{3/2} < \nu^*$  [27]. Figure 2.3 illustrates how the diffusion coefficient changes with collisionality in three regimes.

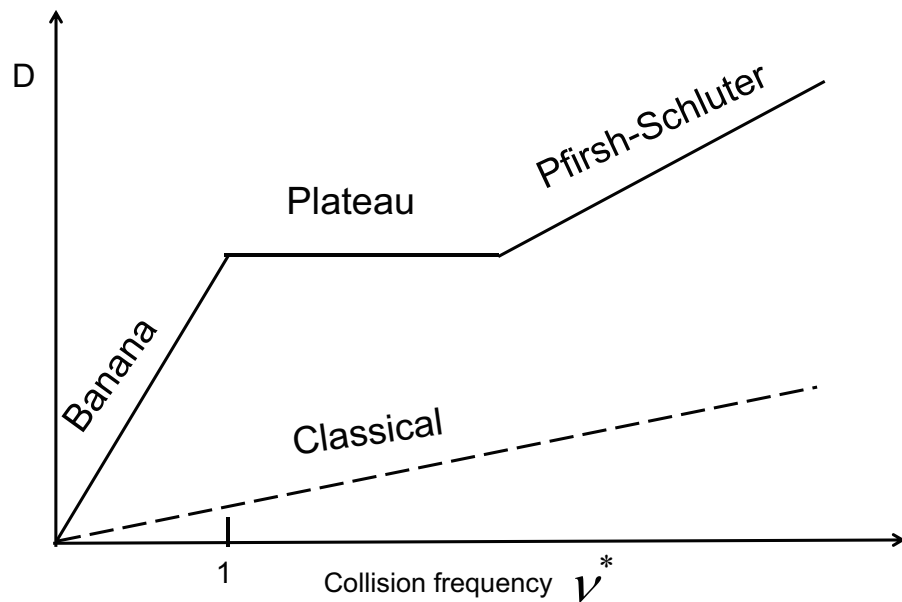


FIG. 2.3: Diffusion coefficient in Classical and Neoclassical transport .

Another implication of the neoclassical transport theory for electrons is that the externally induced toroidal electric field causes inward plasma pinching. It is been observed in the Alcator C-Mod tokamak [28] with ion cyclotron range of frequency (ICRF) heating (a heating method which heats the ions through wave-particle resonance), that an internal transport barrier is formed in the plasma core. This internal transport barrier results in a peaked density profile in the center while keeps a similar density profile outside mid-radius, see Figure 2.4. Since there is no central particle source, the increase in central

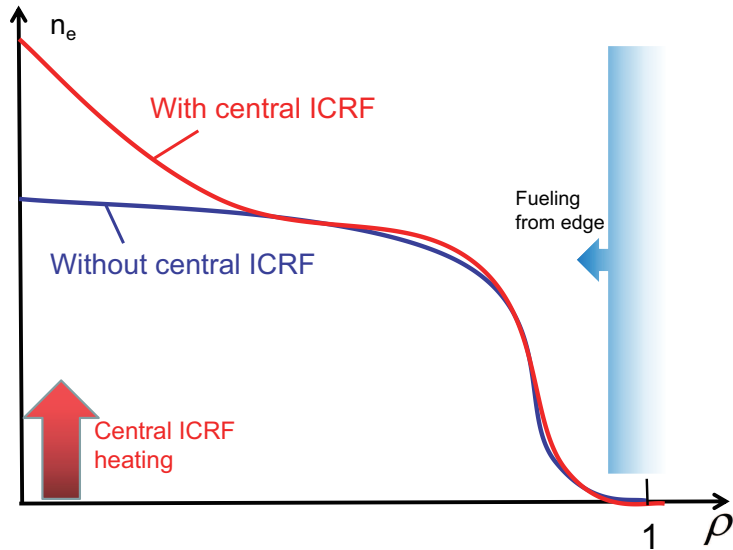


FIG. 2.4: Core density peaking under ICRF .

density suggests that the outward diffusion needs to be balanced by an inward pinch. In 1970, A. A. Ware [29] found that, in toroidal plasmas, collisionless trapped particles can drift inward at a velocity of

$$v_{ware} = cE_\phi/B_\theta$$

which is about 100 times larger than the inward direction's  $\mathbf{E} \times \mathbf{B}$  drift  $v_{E \times B} = \frac{cE_\phi B_\theta}{B_\phi^2}$ . Here  $B_\theta$  is poloidal magnetic field,  $E_\phi, B_\phi$  are toroidal electric and magnetic field, and the  $\mathbf{E} \times \mathbf{B}$  drift is the drift that a particle has when under the electric force that is perpendicular

to the magnetic field (it has the magnitude of  $\mathbf{v}_{E \times B} = \frac{c\mathbf{E} \times \mathbf{B}}{B^2}$  with the direction being perpendicular to both the force and the field). This pinch is later named as the Ware pinch [29, 17] and has been identified experimentally in many tokamaks [30, 31, 32, 33].

### 2.1.3 The need for anomalous processes

The former two sections have introduced the classical and neoclassical theories for the cross-field transport. Although neoclassical theory predicts a diffusion coefficient that is two orders larger than the classical prediction in our experimental conditions, it is still too small compared with the actual experimental measured value. For example, in one of our DIII-D low collisionality discharges [21], the measured electron density is around  $5 \times 10^{19} m^{-3}$  in plasma core, and the electron flux which is calculated by particle balance equation is  $0.5 \times 10^{19} m^{-2}s^{-1}$ . Therefore the actual effective diffusion coefficient should be of the order of  $0.1 m^2/s$ , which is much larger than either the classical prediction ( $D^{electron} = D^{ion} \approx 10^{-4} m^2/s$ ) or the neoclassical prediction ( $\approx 10^{-2} m^2/s$ ). Similar observations are also found in other tokamaks such as ASDEX [34, 30], TFTR [35], and JET [36], where measured electron particle diffusivity (around  $0.1 m^2/s$  for H-mode and  $1 m^2/s$  for L-mode) is of the same order of the electron heat conductivity and is much larger than the neoclassical predictions.

On the other hand, central density peaking which exceeds the Greenwald limit (an empirical scaling which describes the plasma edge density limits in tokamak plasmas at the pedestal [37]) has been regularly observed in many tokamaks around the world [38, 39, 40, 41]. Density peaking in the core can have two causes: fueling or an inward pinch. While the neoclassical Ware pinch has been identified in some experiments [30, 31, 32, 33], in most conditions it is too small to play a role when compared with the

plasma diffusivity (which is assumed to be of the order of electron heat conductivity [30]). The Ware pinch cannot explain the peaking of density profiles in a wide range of conditions.

Therefore, the assumption of some kind of anomalous cross-field transport is an evident necessity for both energy and particle transport in tokamaks. Here the anomalous transport is defined as every other transport phenomena that cannot be explained by classical and neoclassical theories in plasma systems. Historically, the anomalous transport in tokamaks is usually blamed on low-frequency micro-instabilities caused by plasma turbulence. Large amount of research has been done on turbulent transport since the 1970s and significant progress has been made on both theoretical models and diagnostic capabilities during the past decades. We will introduce some basic turbulence concepts as well as the physics of turbulent particle transport in the next two sections.

## 2.2 Turbulence

### 2.2.1 General introduction to turbulence

Turbulence is a common phenomenon in fluid dynamics. The general cause of turbulence in a fluid is that, the inertial effects (mass wanting to keep going in the direction that it's going) grow so large that the fluid's viscous effects can not contain the system in the laminar flow regime anymore. When those viscous effects cannot slow down a whole chunk of fluid, they are acting as an off-axis force to create angular momentum or vortices on the fluid mass. Because turbulence flow possesses vorticity, it is useful to think of the flow as a hierarchy of eddies of different scales. Figure 2.5(a) shows the fast camera image of a neutral white fluid being ejected into a static black background. We can see the turbulence causes the formation of eddies of many different length scales. A turbulent

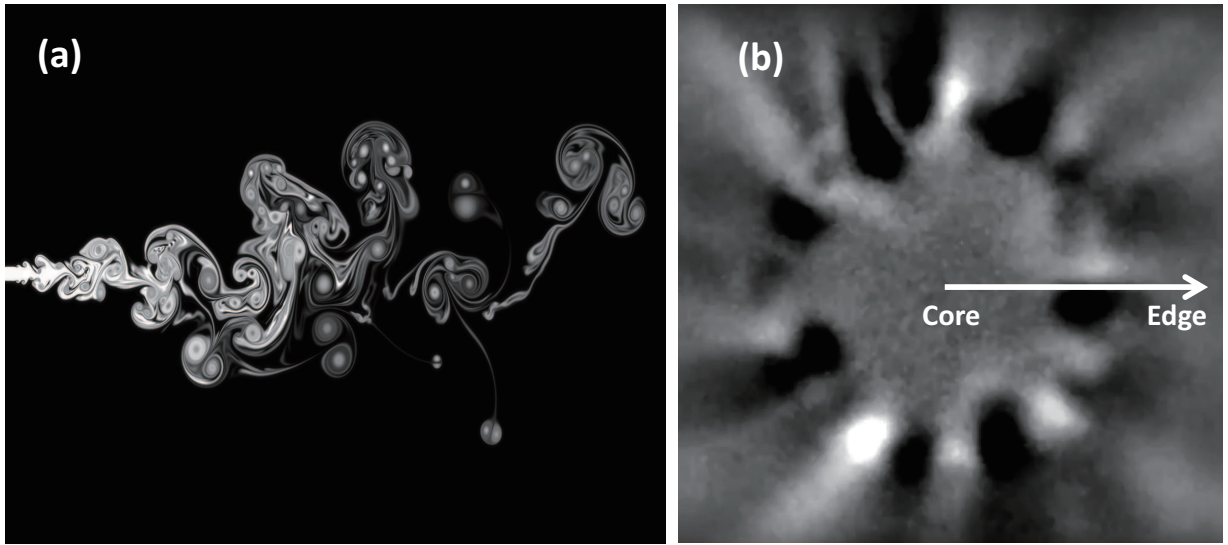


FIG. 2.5: Fast camera imaging of turbulence in laboratory. (a) A single pulse neutral white fluid ejected from a nozzle. (Figure taken from *Fluid dynamic gallery, engineer department, University of Duisburg-Essen, Germany*) (b) Cross section film of plasma turbulence in the cylindrical Large Plasma Device (LAPD) at UCLA (Figure taken from *T. A. Carter Ref [42]*)

eddy is a small convection cell, where particle is transported from one side of the eddy to the other side by a fast flow. As a result, a larger eddy can transport plasma over a larger radial extent. The eddy coherence length can be defined as the distance over which the eddy flow remains correlated and can be thought of as a distance on the order of the eddy diameter in fully developed turbulence [43]. Moreover, during a turbulent transport process, the diffusive component of transport scales linearly with the eddies' radial extent. As shown in Figure 2.5(b), in plasmas, there also exist turbulences causing fluctuations in density, temperature and potential (black and white blobs in the picture). In a simplified model, if we assume  $L_{mach}$  the typical machine size,  $\Delta$  the radial eddy size,  $N$  the number of steps to randomly walk out of plasma. Then for a particle to be transferred out of the machine by turbulence, there should be the following equation [44]:

$$L_{mach} \approx \sqrt{N} \cdot \Delta \quad \rightarrow \quad N = \left( \frac{L_{mach}}{\Delta} \right)^2 \quad (2.5)$$

Here  $\sqrt{N}$  is the expected distance from the origin for a unit random walk in N steps, it is a statistic average value, readers can refer to William Feller's "An Introduction to Probability Theory and Its Applications", Chapter 5 for more detailed derivation. If the time scale of the eddy is  $\frac{\Delta}{v_e}$ , where  $v_e$  is the characteristic flow velocity of the eddy. Therefore the confinement time of the plasma will scale with [43, 44]:

$$\tau_E \propto N\left(\frac{\Delta}{v_e}\right) \propto \left(\frac{L_{mach}^2}{\Delta \cdot v_e}\right) \quad (2.6)$$

Thus we can see from equation 2.6 that the increase of the coherence length  $\Delta$  can strengthen turbulent transport and cause the decrease in the plasma confinement time.

Another property of turbulence is the turn over time, which is defined as the time for turbulence to lose its coherence. At each position, the plasma flow is a superposition of many eddies of different scale length. The configuration of these eddies is constantly changing due to the transfer of energy between the different scales. We can quantify the turn over time by assuming that, when an eddy rotates, its energy has been transferred to other eddies and it has decayed in time  $\tau_e = \frac{\Delta}{v_e}$  [43], where  $v_e$  is the flow's characteristic velocity. In the absence of viscosity, this energy transfer process is conserved since there is no loss of energy, only a transfer of energy from one scale to another. However, viscosity is inherently present in a fluid. The effect of viscosity can be quantified by the viscous dissipation rate (the rate at which the energy of fluid motion is dissipated and converted to heat),  $\tau_d^{-1} = \mu_{vis}/\Delta^2$ . Where  $\mu_{vis}$  is the kinematic viscosity. Since the dissipation rate is inversely proportional to  $\Delta^2$  while the turbulence turn over rate only inversely proportional to  $\Delta$ , at smaller eddy scale,  $\tau_d^{-1}$  increases faster than  $\tau_e^{-1}$ . Therefore, at large scales where  $\tau_d^{-1} < \tau_e^{-1}$ , the energy is transferred between scales with negligible dissipation, establishing an energy cascade. At smaller scales where  $\tau_d^{-1} > \tau_e^{-1}$ , the energy is dissipated before it

can be transferred to other scales, thus terminating the eddies. Finally, in a steady state plasma, to maintain the same amount of energy in the turbulence system, new turbulence eddies should be produced by the instabilities to balance the dissipation. Since eddies are characterized by a small density and potential perturbation, we can define the turbulence growth rate using a perturbative theory:

$$\tilde{n} = n_0 \exp(i\mathbf{k} \cdot \mathbf{x} - i\omega t), \quad \text{where } \omega = \omega_{freq} + i\gamma \quad (2.7)$$

Here,  $\tilde{n}$  is the perturbed density,  $n_0$  is the local plasma density,  $\omega_{freq}$ ,  $\gamma$  denote the instability modes frequency and its growth rate,  $\mathbf{k}$  is the wave number. The growth rate  $\gamma$  is a key indication of how fast the instability, causing the eddies, grows. As indicated in Figure 2.6, a positive value of the growth rate means that the instability causes the eddies to grow, while a negative value corresponds to decay in the growth of the instability.

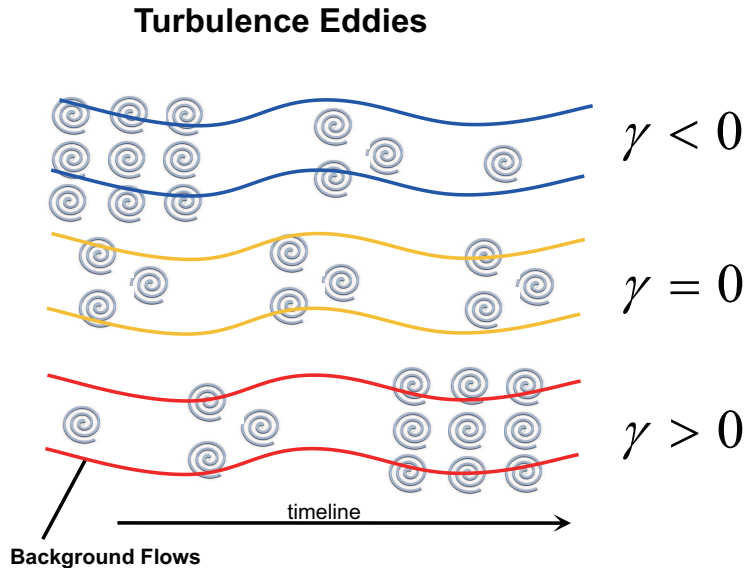


FIG. 2.6: Turbulence eddies' change with corresponding growth rate. The picture shows how growth rate indicates the grow ( $\gamma > 0$ ), decay ( $\gamma < 0$ ), and stasis ( $\gamma = 0$ ) of the instability causing eddies in background plasma flows.

### 2.2.2 $E \times B$ shear stabilization

Turbulent transport in a tokamak can cause heat and particle loss which is larger than the collisional transport. Thus to achieve plasma conditions in which fusion occurs, we need to find a way to reduce turbulence in a plasma. Since the 1990s, both theoretical and experimental work [34, 45, 43, 46, 47, 48, 49] indicate that turbulent transport can be strongly reduced by  $E \times B$  shear flow. Within a tokamak plasma, the electric field is the result of maintaining the force balance in radial direction for each ion species, i:

$$eE_r = e(Z_i en_i)^{-1} \nabla P_i - ev_{\theta_i} B_\phi + ev_{\phi_i} B_\theta \quad (2.8)$$

Here,  $E_r$  is the radial electric field,  $Z_i$  is the net charge,  $P_i$  is the ion plasma pressure,  $v$  is the plasma velocity,  $\theta$  and  $\phi$  denote poloidal and toroidal direction respectively. On the right hand side of the equation, the first force term comes from the pressure gradient, while the second and the third force terms come from the Lorentz force caused by poloidal and toroidal magnetic fields. The radial electric field  $E_r$  can drive a plasma flow which is parallel to the field lines, namely, an  $E \times B$  flow (see Figure 2.7). The flow,  $\mathbf{v}_{E \times B}$ , is the result from Ohms law [17] for an ideal plasma:  $(\mathbf{E} + \mathbf{v}_{E \times B} \times \mathbf{B}) \cdot qn = 0$ . So we can have the  $E \times B$  flows velocity of:  $\mathbf{v}_{E \times B} = \mathbf{E} \times \mathbf{B}/B^2$ . Finally, with the  $E \times B$  flows velocity calculated, we give out the expression for  $E \times B$  shearing rate:

$$\omega_{E \times B} = \frac{dv_{E \times B}}{d\rho} = \frac{(R_0 B_\theta)^2}{B} \left( \frac{\partial}{\partial \Psi} \right) \frac{E_r}{R_0 B_\theta} \quad (2.9)$$

Equation 2.9 is the definition equation of ExB shearing rate  $\omega_{E \times B}$ , where  $R_0$  is the major radius and  $\Psi$  is plasma surface flux. The expression for  $\omega_{E \times B}$  is called the Hahm-Burrell expression [50, 49]. It is a method for calculating the shearing rate based on non-circular plasma equilibria. Equations 2.7 and 2.9 also show us that both the growth rate and the

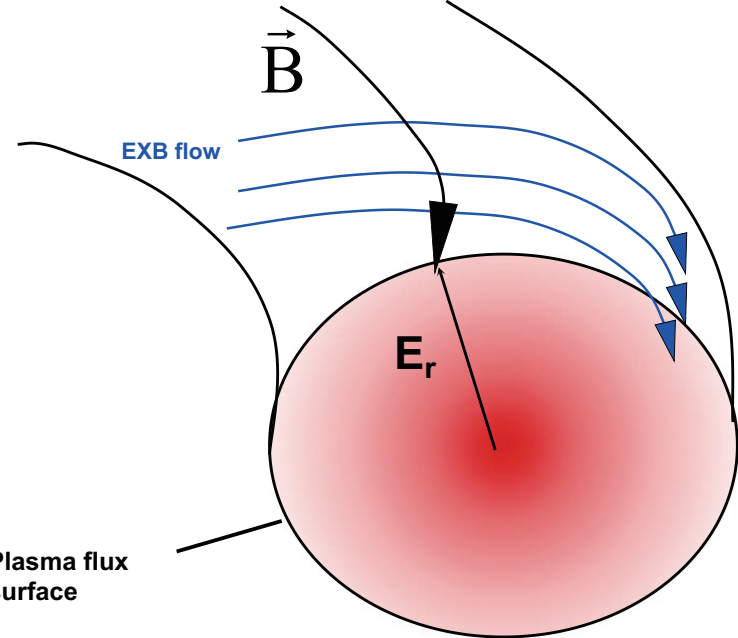


FIG. 2.7:  $E \times B$  shearing rate : the radial electric field as well as the magnetic field caused the  $E \times B$  shear flow which is perpendicular to both of them.

$E \times B$  shearing rate have the same unit (i.e., [rad/s]), so we can compare their magnitudes directly to see which effect (turbulence or  $E \times B$  shear) dominates in a simplified picture.

Theoretically,  $E \times B$  shear can affect turbulence in two ways [49]: nonlinear decorrelation, which includes the reduction in turbulences radial correlation length, phase, and fluctuation size; or linear stabilization, which enhances the turbulences damping by coupling the unstable modes to nearby, stable modes, thus improving the overall stability of the system. As mentioned earlier, the eddy's radial extent scales linearly with the diffusive component of transport. The  $E \times B$  flow shear can reduce the radial extent of eddies by tearing apart turbulence eddies and thus effectively decrease the turbulent transport. In Figure 2.8 we present an intuitive description of how  $E \times B$  shear flow reduces transport through scales decorrelation. Figure 2.8(a) shows that when local flow has the same speed at different radii and no shear exists, all of the microscopic turbulence eddies keep their

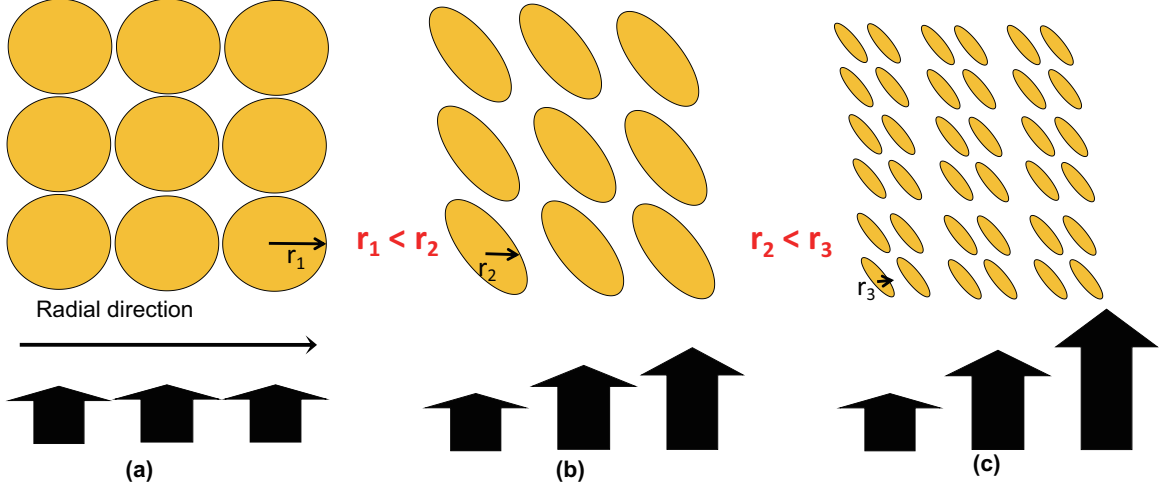


FIG. 2.8: How shear flow tear apart turbulence eddies into small sizes and thus effectively reduce transport. With (a) no shear, i.e. the flow has the same magnitude at all radii. (b) Small variations in poloidal flow velocity start to stretch and tilt turbulence eddies. (c) Large flow shear will finally tear apart eddies into small sizes.

original radial coherence length (i.e., size) as well as their characteristic turn over time. However, when a small flow shear is introduced, the eddies are stretched and start to tilt (Figure 2.8(b)). Finally, when the flow shear increases even more, the shear results in the breakdown of the larger sized eddies into smaller sized eddies (Figure 2.8(c)). Since the transport diffusivity scales with eddy's radial extent, this breaking down process caused by shear flow can strongly reduce the turbulent transport. As an experimental example, we show in the Figure 2.9 the evolution of the plasma turbulence under  $E \times B$  shear flow in the cylindrical Large Plasma Device (LAPD) at UCLA [42]. Figure 2.9(a) is the fast camera imaging of the turbulence with no shear flow. At some point a biasing electric field is placed radially in this cylindrical system, causing a poloidal  $E \times B$  flow (with  $\mathbf{B}$  field perpendicular to the paper). This flow stretches and tears apart the turbulence eddies (black and white blobs) into smaller pieces along radial directions and thus enhance the confinement (Figure 2.9(c)).

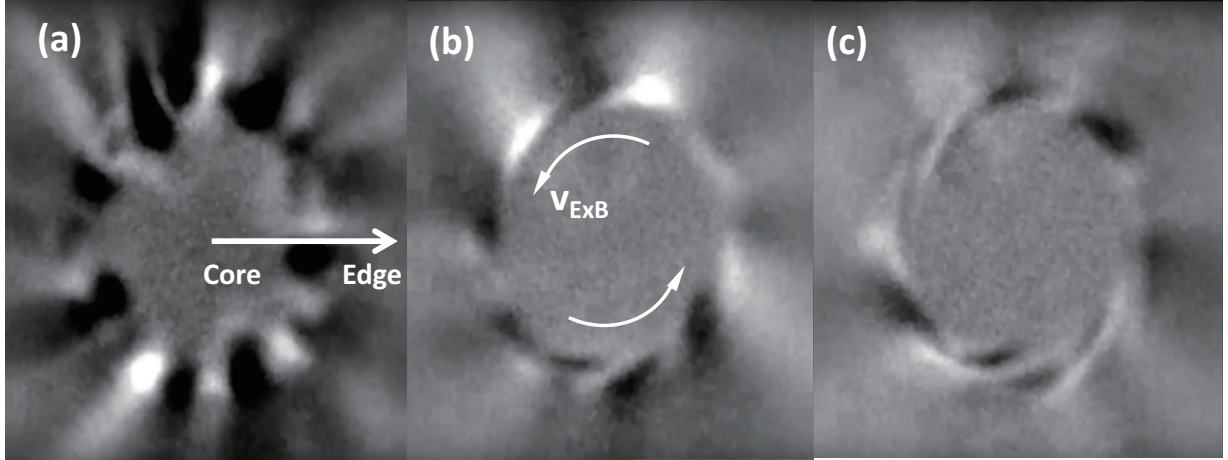


FIG. 2.9: Fast camera imaging of turbulence suppression by shear flow. (a) Cross section film of plasma turbulence in no shear flow. (b) Shear flow starts to stretch the turbulence eddies. (c) Fluctuation amplitude decreases in the stretched eddies. (Figure taken from *T. A. Carter Ref [42]* in the cylindrical Large Plasma Device (LAPD) at UCLA.)

### 2.2.3 Types of turbulence: ITG & TEM

We have mentioned in section 2.2.1 that instabilities are the “source” of energy that maintains and drives turbulence at different scales in plasmas. As the last part of this section, we will discuss two types of instability modes, namely, the ion temperature gradient (ITG) mode and the trapped electron mode (TEM). The ITG and the TEM modes are the second most dangerous class of modes after the macroscopic magneto-hydrodynamic instability (MHD) modes. These two kinds of instability modes have poloidal wave length of the same order as microscopic eddy size (on the order of the ion gyro-radius) and typically have a maximum growth rate at  $0.1 < k_\theta \rho_s < 2$ , (here  $k_\theta$  is the poloidal wavenumber,  $\rho_s$  is the ion gyro-radius). Thus ITG and TEM instabilities are potentially two of the most likely candidates for explaining the turbulence and anomalous transport in tokamaks [51].

First, we try to give an intuitive picture of what can cause an instability in a plasma

based on the analogy of an inverted pendulum. As shown in Figure 2.10(a), an inverted pendulum is in an unstable equilibrium system when compared to a stable pendulum whose oscillation frequency is  $\omega = \sqrt{g/L}$ , which means a small perturbation away from its equilibrium point can keep growing with a growth rate of  $\gamma$ . Similarly, in a tokamak,

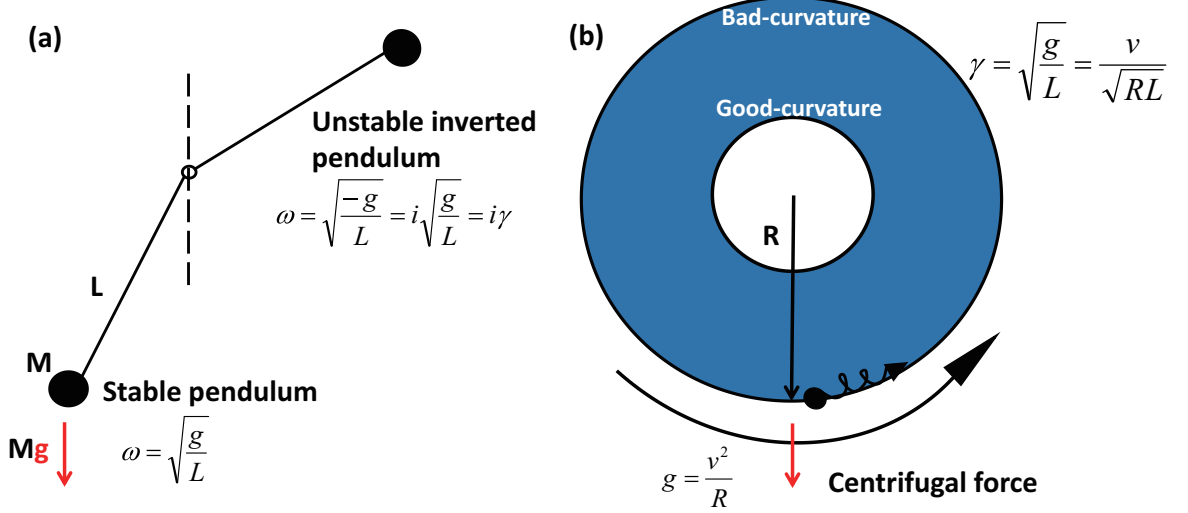


FIG. 2.10: Pictures of instabilities in (a) an unstable inverted pendulum and in (b) toroidal plasmas (top view of a toroidal plasma).

as the plasma rotates toroidally around the torus, the centrifugal force which points radially outward produces the instability mechanism. It is shown in Figure 2.10(b) that the corresponding  $g = \frac{v^2}{R}$ , and thus the instability growth rate  $\gamma = \frac{v}{\sqrt{RL}}$ . Here,  $L$  is the characteristic length of the inhomogeneity, specifically,  $1/L \propto \nabla p/p$  for macroscopic magneto-hydrodynamic instabilities and  $1/L \propto \nabla n$  and  $\nabla T$  for microscopic drift wave instabilities. Where  $p$  is plasma pressure,  $n$  and  $T$  are plasma density and temperature. In addition, although the poloidal magnetic field keeps carrying plasma from bad curvature region (outside-torus curvature region) to good curvature region (inside-torus curvature region), the instabilities can still arise if the growth rate is larger than the propagation from bad-curvature to good curvature regions.

Next we will derive briefly the ITG growth rate and threshold. The ion temperature gradient ( $\nabla T_i$ ) driven nature will also be presented in this derivation. We start from a simplified drift-kinetic equation which describes the time evolution of the plasma distribution function  $F(\mathbf{x}, v_{\parallel}, \mu, t)$  [52] (the derivation of this kinetic approximation can be found in Ref [53, 54, 17]):

$$\frac{\partial F}{\partial t} + (\mathbf{v}_{\parallel} + \mathbf{v}_{E \times B} + \mathbf{v}_d) \cdot \nabla F + \left( \frac{q}{m} - \mu \nabla_{\parallel} B + v_{\parallel} (\mathbf{b} \cdot \nabla \mathbf{b}) \cdot \mathbf{v}_{E \times B} \right) \frac{\partial F}{\partial v_{\parallel}} = 0 \quad (2.10)$$

where  $\mathbf{v}_{E \times B} = -\frac{e}{B} \nabla \tilde{\phi} \times \mathbf{b}$  is the perturbed  $E \times B$  shear velocity,  $\mathbf{b}$  is the unit vector in magnetic field direction,  $\tilde{\phi}$  is the perturbed potential.  $\mathbf{v}_d \approx \frac{v_{\parallel}^2 + v_{\perp}^2/2}{\Omega B^2} \mathbf{B} \times \nabla B$  is the  $\nabla B$  and curvature  $B$  drift velocity ( $\Omega = \frac{eB}{mc}$  is the ion gyro-frequency).  $\mu = \frac{v_{\perp}^2}{2B}$  is the magnetic moment. Equation 2.10 assumes a collisionless and weak electric field condition, and is simplified using a gyrokinetic form [52] from the original time evolution of  $F(\mathbf{x}, \mathbf{v}, t)$  [55]. Gyrokinetic approximation assumes that the gyro-motion of a particle is neglectable and the particle's motion can be described by the guiding center's motion. Thus the plasma distribution function can be written as  $F(\mathbf{x}, v_{\parallel}, \mu, t)$ . We separate the distribution function into an equilibrium part and a perturbation part  $F = F_0 + \tilde{F}$ , where  $\tilde{F}$  is small if compared with  $F_0$ . Substitute back into Equation 2.10, the equilibrium part and the perturbation part should satisfy the following equations:

$$(v_{\parallel} \mathbf{b} + \mathbf{v}_d) \cdot \nabla F_0 - \mu \nabla_{\parallel} B \frac{\partial F_0}{\partial v_{\parallel}} = 0 \quad (2.11)$$

$$\frac{\partial \tilde{F}}{\partial t} + (v_{\parallel} \mathbf{b} + \mathbf{v}_d) \cdot \nabla \tilde{F} - \mu \nabla_{\parallel} B \frac{\partial \tilde{F}}{\partial v_{\parallel}} = -\mathbf{v}_{E \times B} \cdot \nabla F_0 - \left( \frac{q}{m} E_{\parallel} + (\mathbf{v}_{\parallel} \cdot \nabla \mathbf{b}) \cdot \mathbf{v}_{E \times B} \right) \frac{\partial F_0}{\partial v_{\parallel}} \quad (2.12)$$

The equation of the perturbed distribution function can be linearized by assuming  $\tilde{F} =$

$\tilde{F}_0 \exp(i\mathbf{k} \cdot \mathbf{x} - i\omega t)$ , where  $\omega$  and  $\mathbf{k}$  are wave frequency and wave number,  $\tilde{F}_0$  is the wave's amplitude. Equation 2.12 then becomes:

$$(-i\omega + i\mathbf{v}_\parallel \cdot \mathbf{k}_\parallel + i\omega_{dv})\tilde{F} = -\mathbf{v}_{E \times B} \cdot \nabla F_0 - \left(\frac{q}{m} E_\parallel + (\mathbf{v}_\parallel \cdot \nabla \mathbf{b}) \cdot \mathbf{v}_{E \times B}\right) \frac{\partial F_0}{\partial v_\parallel} \quad (2.13)$$

where  $\omega_{dv} = \omega_d(v_\parallel^2 + \mu B)/v_t^2$  is the  $\nabla B$  and curvature B drift frequency,  $\omega_d = -k_\theta \rho_s v_t/R$  and  $v_t$  is the ion thermal velocity. Assuming the equilibrium part of distribution function  $F_0 \propto \frac{n_0}{T_i^{3/2}} \exp(-E/T_i)$ , and  $E = \frac{1}{2}mv_\parallel^2 + m\mu B$  is the particle's energy, the first and third terms on the right hand side will yield to:

$$i(\omega_{*v}^T - \omega_{dv}) \frac{e\tilde{\phi}}{T_i} F_0 \quad (2.14)$$

where  $\omega_{*v}^T = \omega_*[1 + \eta(E/T - 3/2)]$ ,  $\omega_* = -k_\theta \rho_s \frac{v_t}{L_n}$ ,  $1/L_n = \frac{\nabla n}{n}$  and  $\eta = \frac{L_n}{L_T}$ . The second term is  $-ik_\parallel v_\parallel \frac{e\tilde{\phi}}{T_i} F_0$ . Thus we can solve for the perturbed distribution function:

$$\tilde{F} = \frac{-\omega_{*v}^T + (k_\parallel v_\parallel + \omega_{dv})}{\omega - (k_\parallel v_\parallel + \omega_{dv})} \frac{e\tilde{\phi}}{T_i} F_0 \quad (2.15)$$

For the ITG mode, we assume all the electrons to be adiabatic (electrons under Boltzmann distribution  $\int dv^3 \tilde{F} = \tilde{n}_e n_{e0} \frac{e\tilde{\phi}}{T_e}$ ) and the plasma to be in a quasi-neutrality state ( $\tilde{n}_e = \tilde{n}_i$ ). By integrating both sides of equation 2.15 over the velocity moment, we can get:

$$n_{e0} \frac{e\tilde{\phi}}{T_e} = \int dv^3 \frac{-\omega_{*v}^T + \omega_{dv}}{\omega - \omega_{dv}} F_0 \frac{e\tilde{\phi}}{T_i} = n_{e0} \frac{e\tilde{\phi}}{T_i} \int dv^3 \frac{F_0}{n_{e0}} \frac{\omega_{dv} - \omega_{*v}^T}{\omega - \omega_{dv}} \quad (2.16)$$

Here we neglected the  $k_\parallel v_\parallel$  since the perturbation along the field line is much slower than the rapid variations which cross the field line (i. e.  $\omega, \omega_{*v}^T, \omega_{dv} \gg k_\parallel v_\parallel$ ). Rearrange the equation and assume  $\omega \gg \omega_{dv}$ , we get the first order approximation of the dispersion

relation:

$$\frac{T_i}{T_e} = \int dv^3 \frac{F_0}{n_{e0}} \frac{\omega_{dv} - \omega_{*v}^T}{\omega} \left(1 + \frac{\omega_{dv}}{\omega} + \dots\right) \approx 2 \frac{\omega_d}{\omega} - \frac{\omega_*}{\omega} + 7 \frac{\omega_d^2}{\omega^2} - 2 \frac{\omega_d \omega_*}{\omega^2} (1 + \eta) \quad (2.17)$$

Equation 2.17 is a second order equation of  $\omega$ , it has solutions of

$$\omega = \frac{2\omega_d - \omega_* \pm \sqrt{(2\omega_d - \omega_*)^2 + 4\frac{T_i}{T_e}(7\omega_d^2 - 2\omega_d \omega_*(1 + \eta))}}{2(T_i/T_e)} \quad (2.18)$$

The growth rate  $\gamma = Im(\omega)$  is the imaginary part of the solutions. As a simple example, considering the flat density limit where  $\nabla n \rightarrow 0$ ,  $\nabla T \neq 0$ . We have  $\omega_* \rightarrow 0$ ,  $\eta \rightarrow \infty$ , and  $\omega_* \eta = -k_\theta \rho_s \frac{v_t}{L_n} \frac{L_n}{L_T} = \omega_{*T}$ . The solution becomes:

$$\omega = \frac{2\omega_d \pm \sqrt{(4 + 28\frac{T_i}{T_e})\omega_d^2 - 8\frac{T_i}{T_e}\omega_d \omega_{*T}}}{2(T_i/T_e)} \quad (2.19)$$

Thus the growth rate is approximately:

$$\gamma \approx \frac{\sqrt{2\omega_d \omega_{*T}}}{\sqrt{T_i/T_e}} = \frac{\sqrt{2}k_\theta \rho_s}{\sqrt{T_i/T_e}} \frac{v_{ti}}{\sqrt{RL_{Ti}}} \quad (2.20)$$

And the instability only exists (i.e. equation 2.17 has complex solutions) when:

$$8\frac{T_i}{T_e}\omega_d \omega_{*T} > \omega_d^2(4 + 28\frac{T_i}{T_e}) \quad (2.21)$$

$$\rightarrow \frac{R}{L_{Ti}} > \frac{1}{2}(7 + \frac{T_e}{T_i}) \quad (2.22)$$

Equation 2.22 indicates the threshold of the ion temperature gradient to produce the ITG instability when we assume a flat density [52, 56, 57, 58, 59].

In ITG mode, all electrons are assumed to be adiabatic. However, as we have discussed in Section 2.1.2, in a toroidal magnetic geometry, both ions and electrons can be trapped on the outside region of the torus when their parallel velocity  $v_{\parallel} < \frac{r}{R}v$  (see Figure 2.2). These trapped electrons are not adiabatic and thus can result in a new instability mode, i.e., trapped electron mode (TEM). The derivation of the TEM threshold is very similar to the derivation of ITG mode, with the only exception that those trapped electrons are not adiabatic. Thus the left hand side of equation 2.16 should become

$$(1 - f_t)n_{e0}\frac{e\tilde{\phi}}{T_e} + f_t \int dv^3 \tilde{F} \quad (2.23)$$

where  $f_t$  is the fraction of trapped electrons. The untrapped portion of electrons  $(1 - f_t)$  are still treated as adiabatic. Following a similar derivation, we can get the dispersion relation of  $\omega$  and thus solve for the growth rate as well as its threshold. For example, J. Weiland derived the threshold of TEM within his model [51, 57]:

$$\frac{R}{L_{Te}} > \frac{f_t}{3(1 - f_t)(1 + \frac{T_e}{T_i} \frac{1}{1 - f_t})} \left( \frac{3}{2} - \frac{R}{2L_n} \right)^2 - \frac{R}{L_n} + 5 \quad (2.24)$$

We can see the drive term for the TEM is a combination of the electron temperature gradient and the electron density gradient. Finally, in Figure 2.11, we give a summary of the ITG mode and TEM mode, including their characteristic wave number region, their affecting transport channels, and some stabilization mechanisms.

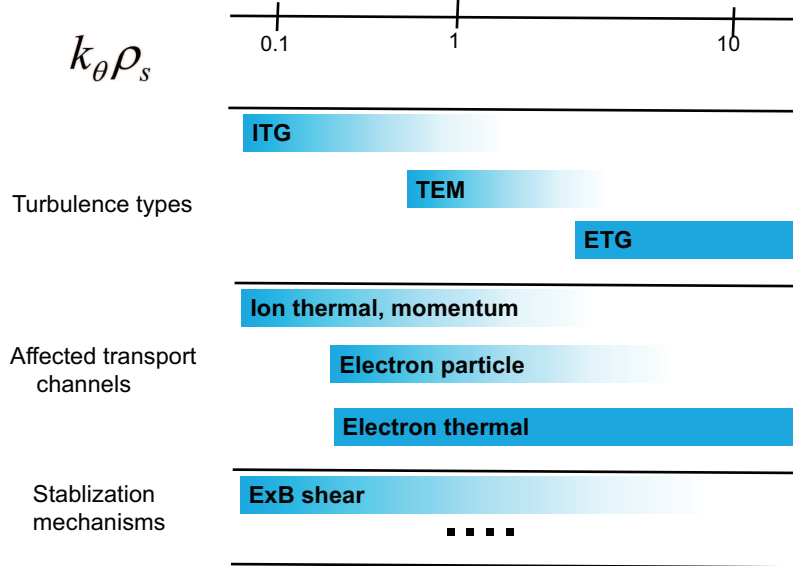


FIG. 2.11: Summary of ITG and TEM turbulence .

## 2.3 Particle transport

### 2.3.1 Effect on density profile

Both the neoclassical and turbulent particle transport can affect the plasma density profiles. The electron particle flux is governed by the continuity equation for the electron density,  $n_e$ :

$$\frac{\partial n_e}{\partial t} = -\nabla \cdot (\mathbf{v}_e n_e) + S \quad (2.25)$$

where  $\mathbf{v}_e$  is the electron flow and  $S$  is the particle source. For the turbulent fluctuation in a tokamak, because both toroidal and poloidal flows effectively lie on the nested tori and therefore lead to no loss, net losses are consequently governed by a radial derivative of the product of density and radial flow  $u_{re}$ . Separating the density into averaged and fluctuated components  $n_{e0}$  and  $\tilde{n}_e$ , and considering equilibria in which the average radial

flow is zero, we find that the average density is governed by:

$$\frac{\partial n_{e0}}{\partial t} = -\frac{\partial \Gamma_e}{\partial r} + S, \quad \text{where} \quad \Gamma_e = \tilde{u}_{re} \tilde{n}_e \quad (2.26)$$

If the density perturbations are proportional to the gradient, substitution of the proportionality relationship into the flux yields an expression of  $\Gamma_e = -D_e \frac{dn_e}{dr}$  (Fick's law, where  $D_e$  is the diffusion coefficient). In general, for both the neoclassical and turbulent particle transport, the particle flux can be written as a combination of a diffusive term which is proportional to the density gradient and a convection term which is proportional to the density:

$$\Gamma = -D \frac{\partial n}{\partial r} + v n \quad (2.27)$$

here  $D$  is the diffusion coefficient and  $v$  is the convection coefficient. While the neoclassical diffusivity is proportional to collisionality and the convection is usually from Ware pinch, the turbulent transport coefficients can be altered based on different plasma parameters and thus determining the local density profile as well as overall confinement. [60, 61]. Figure 2.12 is an example to show how the diffusion and convection coefficients can make a difference in local density profile of a non-central-fueling steady state plasma.

First, turbulent transport is found to produce inward pinch which leads to density peaking. The observations of peaked density profiles in non-inductive tokamak discharges on Tore Supra [62, 63], TCV [64], FTU [65], and JET [66], where there is no toroidal electric field and thus no Ware pinch exist are direct evidence (there is also no core fueling in these experiments). Another evidence comes from recent experiments on ASDEX [67, 68], where an electron density peaking in plasma core is observed when adding center electron heating power into H-mode plasmas while keeping the same amount of neutral

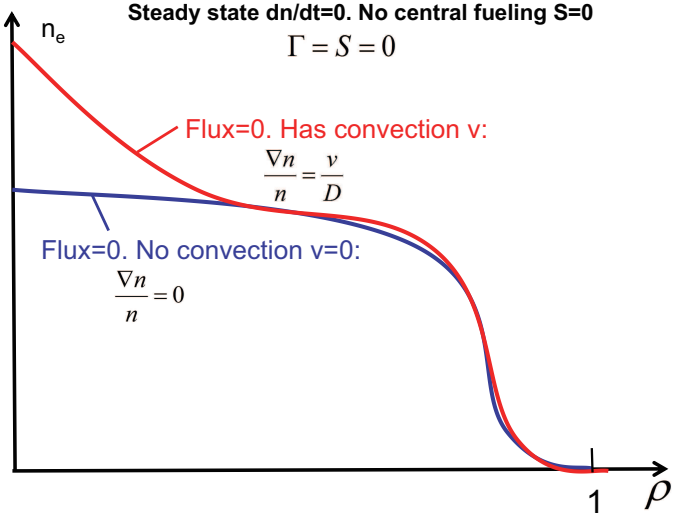


FIG. 2.12: Local density profile determined by diffusion coefficient  $D$  and convection coefficient  $v$ .

beam injection (NBI) power. The core fueling is the same during the whole discharge and the turbulence is in ITG or ITG/TEM regime. However, this phenomenon is not observed in current DIII-D experiments performed at low plasmas density [69]. Finally, in a separate cylindrical plasma experiment on CSDX [70], a net inward, up-gradient turbulent particle flux is reported when collisional drift waves generate a sufficiently strong sheared azimuthal flow. This is a more fundamental experiment addressing the turbulence interaction mechanisms and its driven transport.

On the other hand, turbulent transport also causes density flattening. The recent experimental observations in DIII-D by S. Mordijck et al. [69] point out that, an outward particle flux is produced by TEM instabilities as a consequence of central electron heating. This phenomenon is often referred to as density pump-out in the literature and has been observed previously in TCV [71, 72], AUG [24, 73], T-10 [74], and Alcator C-Mod [32] tokamaks. Moreover, one recent experiment in DIII-D shows (more details will be presented in Chapter 6), although the electron heating power is deposited in plasma core,

both the particle flux and the intermediate-scale density fluctuation are increased closer to the plasma edge, indicating a turbulence driven nature of the pump-out.

Since peaked core density is desirable and core fueling is impossible in future burning plasmas devices such as ITER [75, 76], the density profile will be determined mainly by the balance between outward diffusion and inward convection, see Figure 2.12 where  $\frac{\nabla n}{n} = \frac{v}{D}$ . In the past two decades, experimental researches have been intensively dedicated to identify the scaling of density profile peaking on various plasma parameters in many tokamaks. In JET H-mode discharges [77, 78, 79], results from an extensive database analysis of density profiles in stationary conditions show that the density peaking increases 25% as the effective plasma collisionality  $\nu_{eff} \approx 10^{-14}RZ_{eff}n_e/T_e^2$  decreases from 1 at mid-radius to below 0.1 as expected for ITER. Where  $R$  is the tokamak major radius,  $Z_{eff}$  is the effective ion charge number,  $n_e$  and  $T_e$  are the electron density and temperature. This result is comparable to other observations on AUG [61, 73], Alcator C-mod [38], and JT-60U [80]. Moreover, in L-mode or low collisionality H-mode plasmas, magnetic shear is found to affect density peaking [77, 65, 79, 81]. Some earlier work in JET [77, 78] and AUG [81] also shows that the density peaking is strongly correlated with  $n_e/n_G$ , where  $n_e$  is the experimental density and  $n_G$  is the empirically calculated density limit [37]. But recent Alcator C-Mod results [38] counter this correlation. Lastly, the parameter scan on JET [78] and ASDEX [81] does not show obvious evidence of the dependences on electron temperature gradient  $L_{Te}$ , ion temperature gradient  $L_{Ti}$ , electron gyro-radius  $\rho_e$ , and normalized plasma pressure  $\beta_N$ .

### 2.3.2 The full transport matrix

Besides particle transport, there are also two other transport channels (i.e., energy transport and momentum transport) exist in a tokamak plasma. Energy transport determines plasma temperature profile while momentum transport determines plasma rotation profile. Till now, for the particle transport, we have only considered the diffusive effects from density gradient (diagonal term). However, in actual experimental environment, all these three transport channels are coupled. Thus the contributions from off-diagonal terms which are proportional to temperature gradient and rotation shear can also play an essential role in establishing the density profile shapes [82, 83]. We can write the flux equations of coupled transport channels in a unified matrix form:

$$\begin{pmatrix} \Gamma_n/n \\ \Gamma_Q/T \\ \Gamma_M/v_\phi \end{pmatrix} = - \begin{pmatrix} D_n & D_T & D_v \\ \chi_n & \chi_T & \chi_v \\ \chi_{n'} & \chi_{T'} & \chi_{v'} \end{pmatrix} \begin{pmatrix} \frac{1}{n} \frac{\partial n}{\partial r} \\ \frac{1}{T} \frac{\partial T}{\partial r} \\ \frac{1}{v_{th,i}} \frac{\partial v_\phi}{\partial r} \end{pmatrix} + \mathbf{V}_p \quad (2.28)$$

On the left hand side of the equation,  $\Gamma_n$ ,  $\Gamma_Q$ , and  $\Gamma_M$  represent particle, energy and momentum fluxes. On the right hand side, the  $3 \times 3$  matrix is the full transport coefficients matrix with its diagonal term  $D_n$ ,  $\chi_T$ ,  $\chi_{v'}$  representing diffusive flux caused by density gradient, temperature gradient and toroidal rotation gradient in each channel. The off-diagonal coefficients in the matrix represent the contribution of diffusivity from other transport channels. Finally, a pure convection term which exists in the absence of any gradients is also added to complete the full matrix equations.

From Equation 2.28, we can write the radial particle flux equation in the form of:

$$\frac{\Gamma_n}{n} = -D_n \frac{1}{n} \frac{\partial n}{\partial r} - D_T \frac{1}{T} \frac{\partial T}{\partial r} - D_v \frac{1}{v_{th,i}} \frac{\partial v_\phi}{\partial r} + V_{pn} \quad (2.29)$$

The first, second and third term on the right hand side of equation are named diffusion, thermo-diffusion and roto-diffusion term. We can derive these off-diagonal particle transport coefficients via a gyro-kinetic approach. From equation 2.26 we know the fluctuation induced particle flux is:  $\Gamma_e = \tilde{u}_{re}\tilde{n}_e$ . In a statistic plasma, the fluctuation velocity comes from the perturbed  $E \times B$  flow [43]. If the mean magnetic field in a tokamak is  $B$ , and the perturbed electric field can be approximated by an electrostatic fluctuation, i.e.,  $\mathbf{E} = -\nabla\tilde{\phi}$ . The radial component of the fluctuating  $E \times B$  is therefore:

$$\tilde{u}_{Er} = \frac{(\mathbf{E} \times \mathbf{B})_r}{B^2} = -B^{-1}\nabla_\theta\tilde{\phi} \quad (2.30)$$

where  $\nabla_\theta$  is the derivative in the poloidal direction. Furthermore, if a Fourier transform is introduced for the coordinates in the toroidal and poloidal directions, the flux is then proportional to the imaginary part of  $\tilde{\phi}_{-k}\tilde{n}_k$  [43]:

$$\Gamma_e = -B^{-1} \sum_k k_\theta \text{Im}(\tilde{\phi}_{-k}\tilde{n}_k) \quad (2.31)$$

where  $\tilde{\phi}_{-k}$  and  $\tilde{n}_k$  are Fourier amplitudes,  $\mathbf{k}$  is the wave vector composed of poloidal  $k_\theta$  and toroidal  $k_\phi$  components. In section 2.2.3, we derived a kinetic expression of the fluctuating plasma distribution function  $\tilde{F}$  in equation 2.15:

$$\tilde{F} = \frac{-\omega_{*v}^T + (k_\parallel v_\parallel + \omega_{dv})}{\omega - (k_\parallel v_\parallel + \omega_{dv})} \frac{e\tilde{\phi}}{T_i} F_0$$

This kinetic equation is a collisionless, weak electric field expression in the electrostatic limit. For the form with collision and strong electric field, readers are referred to [55]. A more general derivation including electromagnetic effects can be found in [84]. If we multiply both sides of the equation with the conjugation of perturbed potential  $\tilde{\phi}^*$  and

integrate over velocity space, we can get the radial particle flux:

$$\Gamma_e = -B^{-1}k_\theta Im\left(\int dv^3 \left(\frac{-\omega_{*v}^T + (k_\parallel v_\parallel + \omega_{dv})}{\omega - (k_\parallel v_\parallel + \omega_{dv})} \frac{e|\tilde{\phi}|^2}{T_i} F_0\right)\right) \quad (2.32)$$

Since  $\omega_{*v}^T = k_\theta \rho_s [\frac{v_t}{L_n} + \frac{v_t}{L_T} (E/T_e - \frac{3}{2})]$ , where  $v_t$  is particle thermal velocity and  $E$  is particle energy, the electron particle flux becomes:

$$\Gamma_e = B^{-1} Im\left(\int dv^3 \left[\frac{R}{L_n} + \frac{R}{L_T} (E/T_e - \frac{3}{2}) - R(k_\parallel v_\parallel + \omega_{dv})\right] \frac{k_\theta^2 \rho_s v_t e |\tilde{\phi}|^2 F_0}{R(\omega - (k_\parallel v_\parallel + \omega_{dv})) T_i}\right) \quad (2.33)$$

Thus the decomposition presented in equation 2.29 can be recognized in equation 2.33, where diffusion, thermo-diffusion, and convection can be identified as the first, the second and the third term on the right hand side of the equation. We note that while the diagonal diffusion coefficient is always positive (i.e., represents outward flux contribution), the thermo-diffusion coefficient involves the energy dependent kernel ( $E/T_e - 3/2$ ), and as such can be directed inwards or outwards depending on turbulence conditions. For example, theoretical work shows [82, 85, 58, 51] that for electrons, ITG mode produces an increase of particles in the low energy range so that an inward thermo-diffusion “pinch” is obtained. In contrast, a TEM instability produces large amount of energetic particles which result in an outwards thermal-diffusive flux. Similarly, the roto-diffusion term can be derived from momentum transport equation (which is not part of this thesis, readers can refer to [82, 86] for details). To summarize, we present all the predicted inward and outward patterns of each off-diagonal term in the table 2.1, depending on the type of unstable modes and on the particle species.

Table 2.1 provides a starting point for theory validation. Many experiments have been conducted in the last decade to find evidence or at least qualitative agreement with these

TABLE 2.1: Different directions of off-diagonal terms of electron and ion transport for ITG and TEM instabilities.

	Thermo-diffusion		Convection		Roto-diffusion	
	ITG	TEM	ITG	TEM	ITG	TEM
Electrons	IN	OUT	IN		OUT	IN
Ions	OUT	IN			OUT	IN

theoretical predictions. In regard to the thermo-diffusion term, investigations in high density H-mode discharges on ASDEX Upgrade [87] shows that, when we increase the ratio of  $T_e/T_i$  by central electron heating (ECH), the density profile is not affected. However, for intermediate density plasmas, density peaking is increased when we add central electron heating to neutral beam injection (NBI) heated plasma in ITG regime [68]. Finally, in low density L-mode experiments [24] and low density H-mode experiments [73, 69], density pump-out due to central electron heating is observed in TEM regime and thus the density profile is flattened in these discharges. This non-monotonic dependence of density peaking is in correspondence with theoretical prediction that the thermal-diffusive flux changes sign from ITG to TEM region [68, 88]. In particular, both experiments [23] and simulations [22] indicate a correlation between the electron density gradient  $R/L_n$  and the most unstable mode frequency, that is,  $R/L_n$  peaks where the turbulence regime switches over from ITG to TEM and decreases toward either deep ITG or deep TEM regime. It indicates that, when core fueling is small, the thermal diffusive pinch can become one of the most important contributions to the total inward pinch in plasma core [85].

On the other hand, gyro-kinetic simulations [89, 68] show that, while the impact of the toroidal rotation and its radial gradient is negligible on electron particle transport, the roto-diffusion can become important for ion and impurities, due to their heavier mass

and lower thermal velocity. Correlation analysis based on an AUG experimental H-mode database [90, 68] indicates that, in the discharges with neutral beam injection (NBI) heating only and with low electron heating power (dominant by ITG modes), the boron density gradient decreases as the plasma toroidal rotation Mach number and toroidal rotation gradient increases. These plots confirm the important role of roto-diffusion in predicting the experimentally observed trend of increasing impurity peaking.

## 2.4 Summary

In this chapter, we introduce theories as well as experimental results for the particle transport. We first describe the classical and neoclassical theory for cross-field transport. However, these two theories predict smaller diffusion coefficients than the experimental measurements. The turbulence-caused anomalous transport is of particular importance in tokamak plasmas. Next, we introduce some basic properties of turbulence along with one of its suppression mechanisms (via  $E \times B$  shear flow). The driven terms and thresholds of two types of turbulence (i.e., the ion temperature gradient (ITG) mode and the trapped electron mode (TEM)) are presented. Finally, recent literature on particle transport and its relation in determining density profiles are summarized. Both the diagonal and off-diagonal terms of the particle flux are described through a full multi-channel transport matrix.

# CHAPTER 3

## Methods

### 3.1 Theoretical simulation codes

In this section, we introduce two simulation codes: ONETWO and TGLF. ONETWO calculates particle, momentum and energy transport relying on conservation principles. In order to calculate the transport coefficients, ONETWO needs to first calculate the sources using experimental parameters, from which it can calculate the (particle, momentum, energy) flux. Then based on the experiment measured profiles or their fitted profiles, diffusive-like transport coefficients can be extracted. TGLF on the other hand is a quasi-linear gyrokinetic code which calculates the linear driftwave eigenmodes by solving linear fluid approximation of the kinetic equations. Extensive benchmarking of the TGLF eigenmodes against a large database of non-linear gyrokinetic stability calculations verifies that the TGLF model is accurate in small and medium wave number regions [91].

### 3.1.1 ONETWO: One-and-a-half-dimensional transport code

ONETWO code is a one-and-a-half-dimensional, time-dependent code which solves the plasma transport equations in a tokamak [92, 93]. It is one-and-a-half-dimensional because it accounts for the 2D geometry of the flux surfaces in the 1D transport calculations. The magnetic flux surfaces in a tokamak are not circular. Figure 3.1 shows an example of the cross-section of a set of magnetic flux surfaces in a tokamak. The flux surfaces are D-shaped instead of the concentric circles in our former simplified model (Figure 1.5) in Chapter 1. Thus, for ONETWO to calculate a one-dimensional cross field flux from

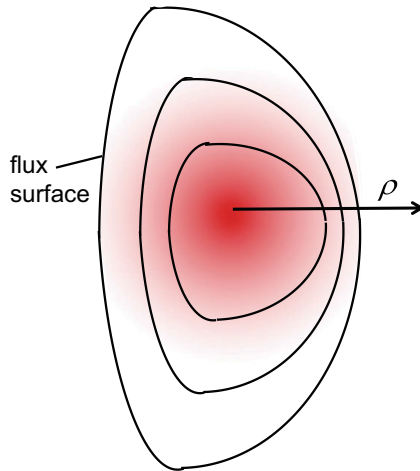


FIG. 3.1: Magnetic flux contours for a D-shaped tokamak plasma.

a two-dimensional system, we first need to know the 2-D geometry. The 2-D magnetic geometry in a tokamak is calculated using a magneto-hydrodynamic (MHD) equilibrium code. MHD model is a single fluid model which describes the macroscopic properties of a quasi-neutrally magnetized plasma. The equation of motion for a charge-neutral plasma placed in a magnetic field is described by:

$$\rho_0 \left( \frac{\partial}{\partial t} + \mathbf{v} \cdot \nabla \right) \mathbf{v} = \frac{1}{c} \mathbf{J} \times \mathbf{B} - \nabla p \quad (3.1)$$

where  $\rho_0 = (m_i + m_e)n_0$  is the plasma mass density,  $m_i$ ,  $m_e$ ,  $n_0$  are ion mass, electron mass, and local density,  $p$  is pressure. The average plasma flow velocity  $\mathbf{v}$  is approximated by the ion velocity and the current is defined by  $\mathbf{J} = n_0e(\mathbf{v}_i - \mathbf{v}_e)$ . In equilibrium, no time variation is involved ( $\frac{\partial}{\partial t} = 0$ ) and the flow velocity is small if compared with  $\sqrt{p/\rho_0}$  (of the order of the plasma sound speed [12]). Equation 3.1 becomes:

$$0 = \frac{1}{c}\mathbf{J} \times \mathbf{B} - \nabla p \quad (3.2)$$

This is the equation to be solved for plasma MHD equilibrium. In a tokamak, we first write both the pressure and the current as a function of poloidal magnetic flux  $\psi(R, Z)$  under a cylindrical coordinate system, i.e.,  $\mathbf{J}$ ,  $p$  can be written as  $\mathbf{J}(\psi)$ ,  $p(\psi)$ . Then equation 3.2 can be transferred into a nonlinear differential equation of the magnetic flux (for more detailed derivations, one should refer to H. Grad's paper in 1958 [94] and V. Shafranov's paper in 1966 [95]). By numerically solving this differential equation, the flux surfaces for a desired equilibrium configuration (like the one shown in figure 3.1) can be obtained. Finally, we can average each quantity in one-dimensional ONETWO model over the calculated 2-D flux surfaces from MHD equilibrium. For example, the flux surface average of plasma density  $n$  within a surface  $S = \oint 2\pi R dl$  is:

$$\langle n \rangle = \frac{2\pi \oint n R dl}{2\pi \oint R dl} = \frac{\oint \frac{n dl}{B_\theta}}{\oint \frac{dl}{B_\theta}} = \frac{\oint \frac{n dl}{B_\theta}}{\frac{1}{2\pi} \frac{\partial V}{\partial \psi}} \quad (3.3)$$

where  $l$  is the distance along a curve lying in a flux surface,  $V$  and  $B_\theta$  are the volume and the poloidal magnetic field in a flux surface [92, 93].

With 2-D flux surface geometry extracted from the MHD equilibrium, ONETWO calculates the flux surface averaged particle, momentum, and energy transport through

particle balance equations, toroidal momentum balance equations and energy conservation equations respectively. For example, the equation that governs the evolution of the density of primary ion species is the continuity equation:

$$\frac{\partial n_i}{\partial t} + \nabla \cdot \Gamma_i = S_i \quad (3.4)$$

here  $n_i$  is the ion species' density,  $\Gamma_i$  is the particle flux of ion species i. On the left-hand side of the equation, the first term denotes time dependent density change and the second term represents the flux surface averaged divergence of the particle flux. The ion density source term on the right-hand side of the equation has multiple contributions. For example, thermal ions are produced through the ionization of neutrals, injected by a neutral beam in the plasma core, or through electron collisional ionization of neutral particles near the plasma-wall area. Some other physical processes that produce sources or sinks of particles and energy are also considered, including ohmic heating, radio frequency (RF) heating, gas puff, electron-ion energy exchange, radiation and so on. Different source calculation models such as NFREYA [96] and NUBEAM [97] which use Monte Carlo techniques to simulate the beam deposition in tokamaks are implemented into the ONETWO code. Therefore, from the simulated source term, we can calculate the ion particle flux. Moreover, if provided with the experiment measured density profile, the diffusive-like transport coefficients can be obtained. Figure 3.2 is an example which shows the beam source from neutral beam injection in plasma core, and the resulted outward particle flux calculated by ONETWO from equation 3.4 (ONETWO assumes that the plasma is not evolving, i.e.,  $\frac{\partial n_i}{\partial t} = 0$ ). The centrally deposited beam source leads to the increase of an outward ion particle flux from  $\rho = 0 - 0.2$ . In addition, ONETWO assumes that the electron flux is the same as the ion flux based on quasi-neutral approximation of the plasma. Finally, the momentum and

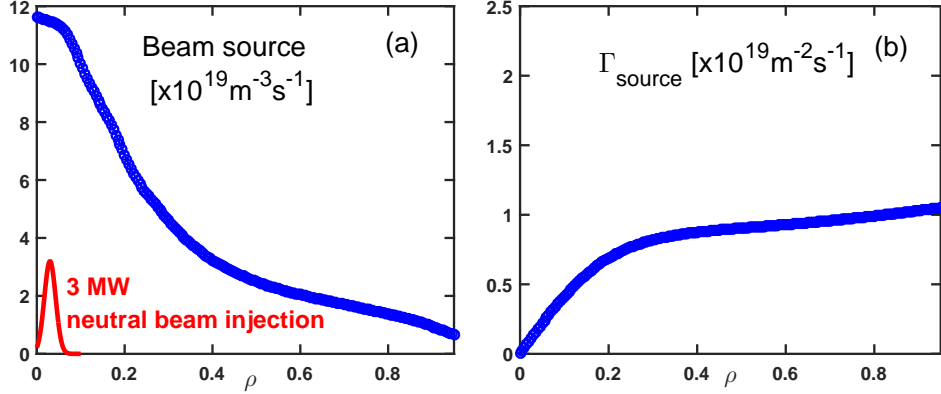


FIG. 3.2: ONETWO calculated source and particle flux. (a) Ion beam source profile under 3 MW central neutral beam injection. (b) Corresponding ion particle flux profile calculated from equation 3.4 (which assumes  $\frac{\partial n_i}{\partial t} = 0$ ).

energy balance equations can be calculated in the similar ways:

$$\frac{\partial(n_i \mathbf{v})}{\partial t} + \nabla \cdot \Gamma_M = M_i \quad (3.5)$$

$$\frac{\partial(3/2n_i T_i)}{\partial t} + \nabla \cdot \Gamma_Q = Q_i \quad (3.6)$$

where  $n_i \mathbf{v}$ ,  $3/2n_i T_i$  represent the ion momentum and energy density,  $\mathbf{v}$  is the plasma flow velocity,  $T_i$  is the ion temperature,  $\Gamma_M$ ,  $\Gamma_Q$  are the momentum and energy fluxes,  $M_i$  and  $Q_i$  are the ion momentum and energy sources.

Other applications of ONETWO code include but are not limited to: determining transport coefficients from experimental data, calculation of the current profile for MHD stability analysis, and investigating the effectiveness of gas puff or pellet fueling for increasing plasma density [93].

### 3.1.2 TGLF: Quasi-linear kinetic code

The Trapped Gyro-Landau Fluid (TGLF) code is a quasi-linear gyrokinetic code based on the Gyro-Landau fluid approximation developed by G. Hammett, M. Beer, and R. Waltz in the 1990s [98, 99, 100, 101, 102, 103]. TGLF has been benchmarked against GYRO [104], a full non-linear gyrokinetic code which captures the full diagnostics. This benchmark shows that TGLF agrees well with GYRO up to  $k_\theta \rho_s = 2$  [20] while TGLF only takes much less computational time. Here  $k_\theta$  is the poloidal wavenumber,  $\rho_s$  is the ion gyro-radius. The region  $0 < k_\theta \rho_s < 2$  is typically where the wavenumber of ion temperature gradient (ITG) mode and the trapped electron mode (TEM) exist as we have discussed in Chapter 2.

The derivation of Gyro-Landau fluid equations starts from the Vlasov equation [17, 55] which describes the time evolution of the distribution function of plasmas:

$$\left[ \frac{\partial}{\partial t} + \mathbf{v} \cdot \nabla + \frac{q}{m} (\mathbf{E} + \frac{\mathbf{v} \times \mathbf{B}}{c}) \cdot \frac{\partial}{\partial \mathbf{v}} \right] F = St(F) \quad (3.7)$$

here  $F(\mathbf{x}, \mathbf{v}, t)$  is the plasma distribution function,  $\mathbf{v}$  is the plasma velocity,  $\mathbf{E}$  is the electric field,  $\mathbf{B}$  is the magnetic field,  $c$  is the light speed, and  $St(F)$  represents the collision operator. We can express the distribution function as an equilibrium part and a perturbation part  $F = F_0 + \tilde{F}$  where the perturbation part is expressed as  $\tilde{F} = f(\mathbf{x}, \mathbf{v}) \exp(-i\omega t)$  and is small compared with the equilibrium part. Linearizing the Vlasov equation:

$$[-i\omega + \mathbf{v} \cdot \nabla + \frac{q}{m} (-\nabla \Phi_0 + \frac{\mathbf{v} \times \mathbf{B}_0}{c}) \cdot \frac{\partial}{\partial \mathbf{v}}] \tilde{F} = St(F) - \frac{q}{m} (\tilde{\mathbf{E}} + \frac{\mathbf{v} \times \tilde{\mathbf{B}}}{c}) \cdot \frac{\partial}{\partial \mathbf{v}} F_0 \quad (3.8)$$

Here  $\Phi_0$ ,  $\mathbf{B}_0$  are equilibrium part of the electric potential and magnetic field.  $\tilde{\mathbf{E}}$ ,  $\tilde{\mathbf{B}}$  are the perturbed electric and magnetic fields. This equation is a 6-D phase-space time

dependent equation. Using the similar gyrokinetic approximation as has been discussed in Chapter 2, we can “reduce” this 6-D equation to a 5-D equation by assuming that the gyro-motion of a particle is neglectable and the particle’s motion can be described by the guiding center’s motion. Thus  $F(\mathbf{x}, \mathbf{v}, t)$  can be transferred to  $F(\mathbf{x}, E, \mu)$ , where  $E$  is the particle’s energy and  $\mu$  is the guiding centre’s momentum. Further simplification can be achieved by separating the transport into parallel and perpendicular directions. We use an exponential eikonal function  $\exp(iS)$  (much like the Fourier transform) to represent the rapid, across the field lines perturbations and express the slow, along the field lines variation by a complex amplitude. Here  $S$  is the eikonal [55]. As a result, we can write:  $f(\mathbf{x}, E, \mu) = f_0(\mathbf{x}, E, \mu)\exp(iS)$ , where  $f_0$  is the amplitude and we impose that  $\mathbf{B} \cdot \nabla S = 0$ . When substituting the gyrokinetic form of the perturbed distribution function back into equation 3.8, we get [55]:

$$(-i\omega + v_{\parallel}\nabla_{\parallel} + i\omega_{dv})\tilde{F} = (-v_{\parallel}\nabla_{\parallel} - i\omega_{dv} + i\omega_*^T)F_0J_0\frac{e\tilde{\phi}}{T} \quad (3.9)$$

where

$$\omega_{dv} = \frac{\omega_d}{2v_t^2}(v_{\parallel}^2 + v^2), \quad \omega_d = \frac{\rho v_t \nabla S \cdot \mathbf{B} \times \nabla B}{B^2} \quad (3.10)$$

and

$$\omega_*^T = \omega_*[1 + \frac{3}{2}\eta(\frac{v^2}{3v_t^2} - 1)], \quad \omega_* = -\frac{\rho v_t \nabla S \cdot \mathbf{B} \times \nabla n_0}{n_0 B} \quad (3.11)$$

$\omega_{dv}$  is the  $\nabla B$  and curvature  $B$  drift frequency (the vertical drifts caused by the outward forces that result from magnetic lines’ gradient as well as its curvature),  $v_{\parallel}$  and  $v$  is particle’s parallel and total velocity,  $v_t = \sqrt{\frac{T}{m}}$  is the thermal velocity.  $\omega_*^T$  is the diamagnetic drift frequency,  $n_0$  is the local equilibrium density,  $\rho = \frac{v_t m c}{e B}$  is the gyro-radius,  $\eta = \frac{n_0 \nabla T}{T \nabla n_0}$ , and  $J_0$  represents zero order Bessel function. Collision operator is neglected in this equation to simplify our derivation of the TGLF equations. A more general derivation including

the collision operator can be found in Ref [105], where the collision operator is treated as a function of perturbed distribution function  $St(\tilde{F}) = (\nu_E/2)(\partial/\partial\xi)(1 - \xi^2)(\partial/\partial\xi)\tilde{F}$  ( here  $\xi = v_{\parallel}/v$ ,  $\nu_E$  is an energy dependent scattering rate from Ref [106] ). The added collision term requires no changes to the original closure rules of collisionless TGLF model. Thus, Equation 3.9 is called linearized gyrokinetic equation and is the starting point for the TGLF model.

TGLF integrates the linear gyrokinetic equation over the velocity space which results in six fluid equations. Starting from equation 3.9, when we integrate both sides of the equation over  $\int J_0 d^3v$ , we can get the fluid moment equation of the density:

$$-i\omega N + v_t \nabla_{\parallel} U_{\parallel} - i\omega_* [H_N + \frac{3}{2}\eta(H_{P_T} - H_N)]\Phi + \frac{v_t \nabla_{\parallel} B}{B} U_{\parallel} + i\omega_d (\frac{1}{2}P_{\parallel} + \frac{3}{2}P_T) + K_N = 0 \quad (3.12)$$

with the normalized moments of the fluctuating part of the distribution function defined by [20]:

$$\begin{aligned} \text{Density : } \quad N &= \frac{1}{n_0} \int d^3v J_0 \tilde{F} \\ \text{Parallel velocity : } \quad U_{\parallel} &= \frac{1}{n_0 v_t} \int d^3v v_{\parallel} J_0 \tilde{F} \\ \text{Parallel pressure : } \quad P_{\parallel} &= \frac{1}{n_0 v_t^2} \int d^3v v_{\parallel}^2 J_0 \tilde{F} \\ \text{Total pressure : } \quad P_T &= \frac{1}{3n_0 v_t^2} \int d^3v v^2 J_0 \tilde{F} \\ K_N &= \frac{-v_t}{n_0} \int d^3v [\nabla_{\parallel} J_0 - J_0 \nabla_{\parallel}] v_{\parallel} (\tilde{F} + J_0 F_0 \Phi) \end{aligned}$$

$H_N$ ,  $H_{p\parallel}$ ,  $H_{p\perp}$  are the similar velocity moments integration over the equilibrium part  $F_0$  of the distribution function. In the same way, by integrate over higher orders of the velocity moment (i.e  $\int J_0 v d^3v$ ,  $\int J_0 v^2 d^3v \dots$ ), we can get other five fluid equations of  $U_{\parallel}$ ,  $P_{\parallel}$ ,  $P_T$ ,

$Q_{\parallel}$ ,  $Q_T$ . Where the parallel and total energy are defined as:

$$Q_{\parallel} = \frac{1}{n_0 v_t^3} \int d^3v v_{\parallel}^3 J_0 \tilde{F}$$

$$Q_T = \frac{1}{3n_0 v_t^3} \int d^3v v_{\parallel} v^2 J_0 \tilde{F}$$

We can write these six linear equations into the matrix form and solve for the eigenmodes of  $\omega$ . The imaginary part of the eigenvalue  $Im(\omega)$  represents the mode growth rate, where positive growth rate  $Im(\omega) > 0$  means unstable mode and negative growth rate  $Im(\omega) < 0$  means stable mode. The real part,  $Re(\omega)$ , represents the mode drift frequency. It is also possible to identify the most unstable mode growth rate and frequency for a specified wave number by searching the largest eigenvalue.

In TGLF approximation, both trapped and passing particles have been included. As has been discussed in Chapter 2, trapped particles are particles which bounce back and force in a banana shaped orbit in the outer part of the torus due to their small parallel velocity, see Figure 2.2. Being able to treat both trapped and passing electrons in a unified system of equations is one of the main motivation behind the development of the TGLF model from its predecessor GLF23 model (a similar linear gyro-kinetic model developed by R.E. Waltz et al. [103] in 1997 to solve gyro-Landau fluid equations). For  $k_{\theta} \rho_s < 1$ , GLF23 model has both isothermal circulating electrons and trapped electrons included. For  $k_{\theta} \rho_s \gg 1$ , GLF23 treats all ions to be adiabatic and all electrons to be circulating. This treatment of poloidal wavenumber overlooks the trapped electron mode (TEM) whose wavenumber is  $k_{\theta} \rho_s \approx 1 - 2$  and thus does not capture an important instability [20, 91, 107]. In TGLF, we introduce a trapped electron fraction number  $f_t$  to unify both the trapped and circulating electrons into a same set of equations. While we

are integrating over the velocity momentum, the integration domain for trapped particles should be  $\int_{|v_{\parallel}| < f_t v} dv^3$  and the integration domain for all the particles can be written as  $\int_{|v_{\parallel}| < v} dv^3$  with only  $f_t$  set to be 1. Here  $v_{\parallel}$  is the parallel velocity. Therefore, the TGLF model is theoretically valid from the lowest  $k$  in trapped ion mode all the way up to the electron temperature gradient (ETG) mode at high  $k$ .

The way of calculating  $f_t$  in TGLF is related to the Landau-damping average effect by the trapped particles. Landau damping is a wave-particle interaction damping term in a plasma system [17]. It associates with the particles (resonant particles) in the distribution function that have a velocity nearly equal to the phase velocity of the wave. The particles that have a speed similar to the phase velocity of a wave in the plasma tend to see a relatively static electric field, rather than a rapidly fluctuating one. They will, therefore, exchange energy with the wave. Since turbulence in its nature is a fluctuating “wave” in plasma density and potential, it can exchange energy with particles through this Landau resonance. However, the trapped electrons with fast bounce frequencies in a plasma wave can ‘compete’ with Landau damping, since once the electrons become trapped they can no longer take any more energy from the wave [12]. A classic picture [108] to explain this is that when the resonant electrons are trapped within the wave, they first pick up enough energy from Landau damping to overtake the wave. The wave potential now causes the electrons to lose energy and give it back to the wave, and the cycle continues thus the Landau resonant effect is averaged [109, 102]. In TGLF, not all the trapped electrons are treated to average Landau resonance, only those trapped particles which change the sign of their parallel velocity within half period of the wave are counted (i.e bounce frequency should be larger than the wave frequency). This is expressed in the form that the poloidal angle travelled by a wave in half period should be larger than the electron’s bounce angle  $2\theta_B$  since the electron’s velocity changes sign after getting bounced. The poloidal angle

that a wave travels in time  $\Delta t$  is  $\Delta\theta = \frac{\omega\Delta t}{R_0 q k_{\parallel}}$ , where  $q$  is the safety factor,  $\omega$  is the wave frequency and  $k_{\parallel}$  is the mode parallel wave number. From the fact that half wave period is  $\omega\Delta t = \pi$ , we can define a maximum bounce angle  $\theta_{max}$  for trapped particles which can Landau average a particular wave:

$$\theta_{B,max} = \min\left[\frac{\pi}{2R_0 q k_{\parallel}}, \pi\right] \quad (3.13)$$

Therefore, the fraction of Landau averaging trapped particles can be calculated by  $f_t = \sqrt{1 - \mathbf{B}(\theta)/\mathbf{B}(\theta_{B,max})}$  where  $\mathbf{B}(\theta)$  is the local magnetic field in the poloidal angle  $\theta$ .

TGLF code is written based on the TGLF model to solve six fluid equations numerically. Its workflow is shown in Figure 3.3. Firstly, we use experimental measured profiles like the electron density, the electron temperature and the ion temperature as input to the TGLF code. The magnetic flux surface is described by Miller geometry. Miller geometry [110] is a finite aspect ratio, noncircular equilibrium model which is described by plasma parameters such as elongation, triangularity, safety factor and so on. The equilibrium satisfies the MHD equilibrium [17] and is particularly suitable for localized stability studies. Second, Hermite basis functions are used to convert the TGLF equations from poloidal  $\theta$  space to matrix equations. By taking the inner product of the equations with the Hermite basis functions, the coefficients of six TGLF equations at each grid point can be written in a matrix form and thus can be solved by any eigenvalue solver programs in the next step. Finally, we sort out the most unstable mode growth rate and its corresponding mode frequency from all the eigenvalues of the matrix. The perturbed particle, momentum and energy fluxes can also be obtained by summing their values over all the wavenumbers.

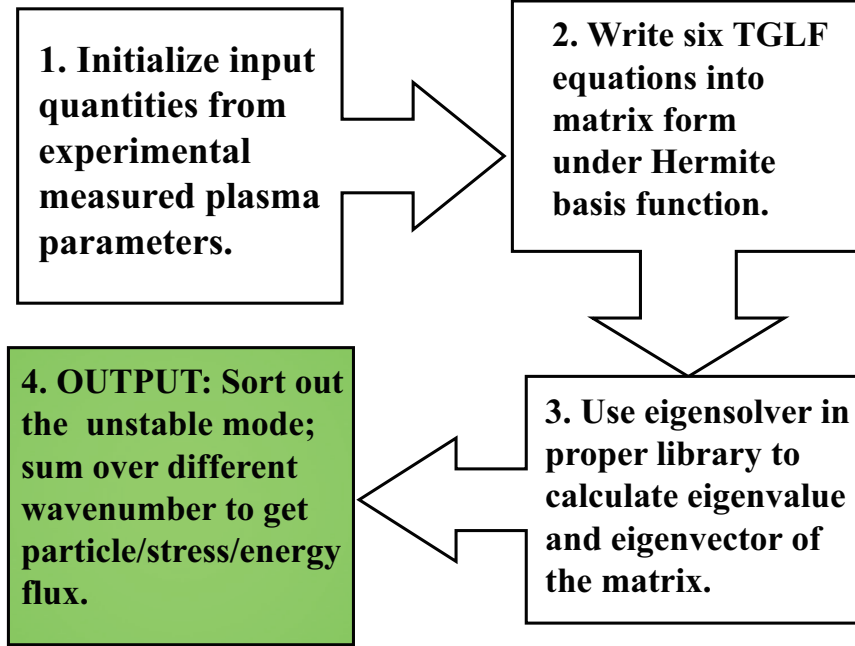


FIG. 3.3: Work flow of TGLF code.

## 3.2 Diagnostics

In this section, we will briefly introduce the principles of the essential diagnostics that are used in this thesis. These diagnostics provide measurements of various plasma parameters such as the electron density, the electron temperature, the ion temperature, the toroidal rotation, and the density fluctuations. Table 3.1 gives a summary of all the diagnostics that will be discussed.

### 3.2.1 Thomson Scattering System

Thomson Scattering is the name of the process where electromagnetic radiation is scattered by free electrons. It is in honor of J. J. Thomson who won the Nobel Price in physics with the discovery of the electron. The Thomson Scattering system is widely used diagnostic system [111, 112, 113, 114] in tokamaks. It measures the absolute electron

TABLE 3.1: Diagnostics for different plasma parameters in tokamaks

Name	Measured parameter
Thomson scattering	Electron density: $n_e$ Electron temperature: $T_e$
Reflectometer	Electron density: $n_e$
Electron cyclotron emission (ECE)	Electron temperature: $T_e$
Charge exchange recombination (CER)	Ion temperature: $T_i$ Poloidal rotation: $v_\theta$ Toroidal rotation: $v_\phi$
Beam emission spectroscopy (BES)	Density fluctuation: $\tilde{n}$ (long wave-length $k_\theta \rho_s < 1$ )
Doppler backscattering (DBS)	Density fluctuation: $\tilde{n}$ (short wave-length $k_\theta \rho_s > 1$ )

temperature from the thermal broadening of scattered laser light [112]. The total scattered power is the sum of the scattered power from individual electron presented in the observed scattering volume. Hence for the Maxwellian distributed electrons in tokamak plasmas, the scattered power spectrum should be Gaussian in shape following the Selden Model [115]:

$$P(\lambda) \sim P_I n_e e^{-\frac{127.5}{T_e} \Delta \lambda^2} \quad (3.14)$$

where  $P(\lambda)$  is the scattered power spectrum,  $P_I$  is the power of incident laser beam,  $n_e$  is the local electron density,  $T_e$  is the local electron temperature,  $\Delta \lambda = \frac{\lambda - \lambda_I}{\lambda_I}$  is the relative difference between incident wavelength  $\lambda_I$  and scattered wavelength  $\lambda$ .

From equation 3.14, we see the scattered power spectrum is under Gaussian distribution with respect to  $\lambda$ . Thus the half width at half maximum of this spectrum,  $\Delta \lambda_{1/e}$ ,

which is measurable, can then be linked with electron temperature by the equation:

$$T_e = \left( \frac{2.5 \times 10^2 \Delta \lambda_{1/e}}{\lambda_I \sin(\theta/2)} \right)^2 \quad (3.15)$$

where  $\theta$  is the angle between incident and scattering laser. In addition, from the scattering power, density profiles can also be determined using equation 3.14.

Experimentally, the spatial resolution of Thomson Scattering is decided by its optical collection chords number while its temporal resolution ( usually  $\approx 5ms$  for DIII-D ) is decided by the amount of laser pulses. DIII-D has a multipulse Thomson Scattering system which uses a mix of 20Hz and 50Hz pulsed lasers with  $\approx 1J$  per pulse [116, 117, 114]. The system has 54 viewing chords giving date from 54 spatial points, including the divertor region, high resolution (50Hz) plasma edge, and plasma core region [114].

### 3.2.2 Reflectometer

The reflectometer is a diagnostic derived from radar principles to measure the electron density using microwaves [118, 119]. As shown in Figure 3.4, it captures the amplitude and the phase variation of a microwave reflected from a cut-off layer at a particular location.

We know that in ordinary polarization situation where  $\mathbf{E} \parallel \mathbf{B}$  ( $\mathbf{E}$  is wave electric field and  $\mathbf{B}$  is the wave magnetic field), the dispersion relation of an electromagnetic wave in plasma is [111]:

$$f^2 = f_{pe}^2 + k^2 c^2 \quad (3.16)$$

where  $f$  is the wave frequency,  $k$  is the wave number, and  $f_{pe} = \frac{1}{2\pi} \left( \frac{n e^2}{\epsilon_0 m_e} \right)^{1/2}$  is the plasma oscillation frequency,  $n_e$  is the local electron density, and  $m_e$  is the electron mass. We

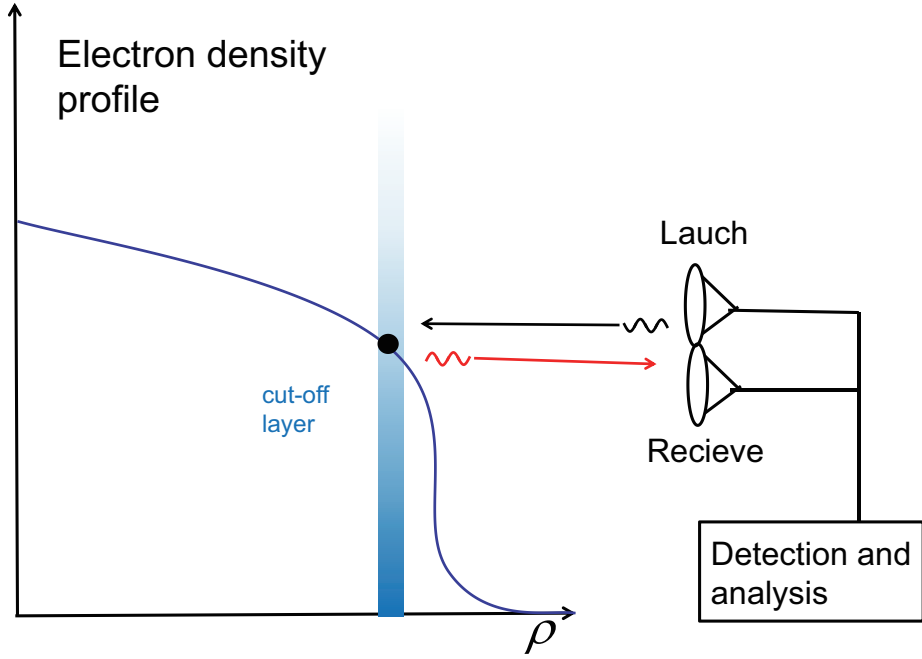


FIG. 3.4: Reflectometer cut-off layer for a given density profile.

can see from equation 3.16, that the frequency of electromagnetic wave,  $f$ , is larger than  $f_{pe}$  that it can propagate in the plasma. Otherwise, the wave is reflected. Thus the cut-off layer is defined as the plasma layer where  $f = f_{pe}$ . Because the plasma oscillation frequency is proportional to the local plasma density, we have a correlation between the incident wave frequency and the local plasma density at the cut-off location [33]:

$$n_e = \frac{4\pi^2 \epsilon_0 m_e}{e^2} f^2 \quad (3.17)$$

Similarly, for the extraordinary polarization situation where  $\mathbf{E} \perp \mathbf{B}$ , we can get the corresponding cut-off frequencies which depend on both electron density and the local magnetic field [111, 33].

In the DIII-D tokamak, the reflectometer system's temporal resolution is typically

$25\mu s$  and it has a density range of  $n_e = 0 - 6.2 \times 10^{19} m^{-3}$  for  $B_t > 1.6T$  [120]. It also has a very high spatial resolution ( $\approx 0.4cm$ ) which can be useful to measure the electron density profile as well as its dynamic evolution. However, the reflectometer profile data can become inaccurate and have errors when there are flat or hollow density profiles. This is because the reflectometer system can only 'see' monotonic increasing electron density profile due to its reflecting nature, i.e., the microwave with the hollow density cutoff frequency will be reflected earlier by outside plasma layers.

### 3.2.3 Electron Cyclotron Emission

The Electron Cyclotron Emission system (ECE) is a routine diagnostic in measuring electron temperature in tokamak plasmas since 1974 [121, 112, 122, 119, 123]. In tokamaks, the electrons gyrate around the toroidal oriented magnetic field lines. This gyromotion results in an electron cyclotron emission of the plasma at the electron gyrofrequency [122, 119]:

$$\omega_{gyro} = n_e \frac{eB}{\gamma_{rel}m_e} \quad (3.18)$$

where  $B$  is the magnetic field,  $m_e$  is the electron mass,  $n=1,2,3,\dots$  is the harmonic wavenumber, and  $\gamma_{rel} = (1 - \beta^2)^{-1/2}$  is the mass increasing effect from relativistic effects. Here  $\beta = v/c$ ,  $v$  is the electron thermal velocity. As mentioned earlier, the magnetic field in a tokamak is inversely proportional to the major radius (equation 2.3), thus the electron cyclotron frequency has a one-on-one mapping to the radius  $R$  of the corresponding resonant layer:

$$\omega_{gyro}(R) = \frac{n_e e B_0 R_0}{\gamma_{rel} m_e R} \quad (3.19)$$

In optically thick plasmas, the ECE radiation intensity received by the antenna ap-

proximately equals the Black Body radiation intensity at temperature  $T_e$  [112]:

$$I(\omega_{gyro}) \approx I_B \approx \frac{k_B T_e \omega_{gyro}^2}{8\pi^3 c^2} \quad (3.20)$$

here  $k_B$  is the Boltzmann constant. Since the Black Body radiation intensity is proportional to  $T_e$  at high temperatures, there is a correlation between the electron temperature and the radiation intensity from equation 3.19, and 3.20:

$$T_e(\omega_{gyro}(R)) = \frac{8\pi^3 c^2 I(\omega_{gyro})}{k_B \omega_{gyro}^2(R)} \quad (3.21)$$

Therefore, the electron temperature profiles based on the measurement of the electron cyclotron radiation intensity can be obtained.

In DIII-D, the ECE radiometer has a very good temporal resolution of 1–2KHz. There are currently 40 channels in the system providing electron temperature data from plasma core to outside mid-radius (specific spatial range varies discharge by discharge depending on toroidal magnetic field  $B_\phi$  and local plasma optical thickness). In our experiments which will be introduced in Chapter 4 to Chapter 6, the spatial resolution is about 2cm [123].

### 3.2.4 Charge Exchange Recombination

Unlike the Thomson scattering or reflectometer systems, which are designed to measure electron properties, the Charge Exchange Recombination (CER) system measures ion temperature, ion poloidal rotation, and ion toroidal rotation. In a deuterium plasma, since  $m_e/m_D \approx 1/3600$  (where  $m_e$  and  $m_D$  are electron and deuterium mass), the ions as well as other impurities (such as  $C^{6+}$ ) carry most of the momentum in tokamak plasmas. As

we will show in Chapter 4, the plasma rotation can have a significant effect on energy and particle confinement. Therefore, it is necessary to get reliable measurements of the ion temperature and impurity rotation.

When a neutral beam (here we take deuterium for example) of very high energy is injected into a plasma, the charge exchange recombination process happens in the form of [124, 125]:

$$\begin{aligned} D_{fast}^0 + A^{Z+} &= D_{fast}^+ + A^{(Z-1)+*} \\ &= D_{fast}^+ + A^{(Z-1)+} + \gamma_0 \end{aligned}$$

where  $D_{fast}^0$  is the injected deuterium atom with large kinetic energy,  $A$  typically represents element of D, He, C, or O,  $Z$  is the atom ionized number,  $\gamma_0$  represents photon, and  $A^{+*}$  means that the newly created ion exists in an excited state. From the above reaction we can see that a deuterium atom and an impurity ion undergo a charge transfer that results in producing an ion in an excited state. The ion then de-excites to the stable state by emitting one or more photons. Thus we can determine the impurity ion temperature and rotation speed respectively from the Doppler broadening of the spectrum and the Doppler shift of the spectral line [126]. For example, the  $70 - 75\text{Kev}$  energetic neutral heating beams used in DIII-D can produce a He II  $468.6\text{nm}$  line which is bright enough to be detected in the spectrum Figure [124].

The CER system of DIII-D has 48 tangential viewing and 32 vertical viewing which cover the whole plasma from the high field side to low field side. Figure 3.5 shows how one cord of the CER system works. A rotating ionized impurity  $A^{Z+}$  collides with an injected fast deuterium atom within the detecting angle and emits photons by de-excitation. This

light is then detected through a set of optical lenses by the spectrometer and is converted into temperature or rotation data.

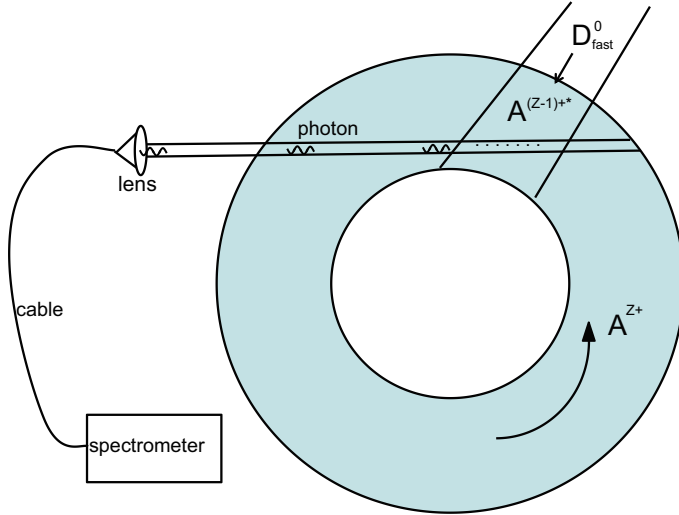


FIG. 3.5: Schematic of CER set up. As we look downward into a tokamak, the impurity rotate counter-clockwisely and collides with injected neutral beams. The emitted photons during this process is captured by outside spectrometer and is converted into ion species' temperature or rotation data.

### 3.2.5 Beam Emission Spectroscopy

Fluctuations in the plasma density, temperature, and electrostatic potential are widely recognized to result in the anomalous cross-field transports which are observed in nearly all magnetically confined fusion plasmas. An understanding of the underlying physical mechanisms that give rise to such fluctuations and transport requires experimental diagnostics to measure the turbulent fluctuations. The Beam emission spectroscopy system (BES) measures localized, long-wavelength ( $k_\theta \rho_s < 1$ ) density fluctuations in tokamak plasmas in an effort to characterize plasma turbulence and resulting turbulent-driven transport. The system obtains the plasma density by observing the collisionally excited emission from the deuterium beam particles as they traverse the plasma, interacting with plasma electrons and ions [127].

The injection of fast neutral deuterium atoms into a fully ionized hot plasma leads to two kinds of physically distinct excitations [128]. The first excitation occurs to plasma ions (or impurities) via charge exchange reactions as have been mentioned in the former section. The second excitation takes place in the injected deuterons themselves through collisions with plasma deuterons, impurity ions, and to a lesser extent, with electrons:

$$\begin{aligned} D_{fast}^0 + A^{Z+} &= D_{fast}^{0*} + A^{Z+} \\ &= D_{fast}^0 + \gamma_0 + A^{Z+} \end{aligned}$$

Here  $A$  represents element of electron, deuteron, or other impurities. The beam atoms that are collisionally excited to the  $n = 3$  quantum state and subsequently decay to the  $n = 2$  state (the D-alpha transition near 656nm) are observed. The D-alpha emission is Doppler-shifted by  $0.5 - 3.5\text{nm}$  because of the beam velocity ( $v = 2.6 \times 10^6\text{m/s}$  for  $70\text{KeV}$  deuterium), allowing the observed beam emission to be spectrally isolated from the intense edge D-alpha emission and the weaker thermal charge exchange signal [128, 127]. The intensity of this emission is a function of the local plasma density and the beam density. Thus the density fluctuations can be calculated through the fluctuations of observed beam-plasma emission intensity.

In DIII-D, the BES system currently has 64 channels, providing spatial resolution of  $1 - 3\text{cm}$  based on the radial and poloidal arrangement of the channels. The detected fluctuations frequency range is  $1 - 500\text{kHz}$  and the accessible spatial region covers from  $0.2 < r/a < 1.0$  (where  $r$  is the radial distance from the magnetic axis,  $a$  is the minor radius of a tokamak, see Figure 1.5).

### 3.2.6 Doppler Backscattering

The Doppler backscattering system (DBS) is a diagnostic technique which measures density fluctuation as well as the propagation velocity of the turbulent structure in the lab frame. It differs from a reflectometer which uses and reflects a normal-incidence microwave beam at a certain cut-off layer. A DBS system is a hybrid of reflectometry and microwave scattering [118, 119, 129]. The return signal of interest in this technique is not due to reflection but is due to Bragg backscattering off turbulent structures. [130, 131].

In solid state physics, the Bragg condition states, when a radiation whose wavelength is comparable to atomic spacings is scattered in a crystal (see Figure 3.6), the distance between each lattice planes within this crystal can be measured through the interference of the reflected waves. Specifically, only those waves with incident angle  $\theta$  which satisfies:

$$2dsin\theta = n\lambda \quad (3.22)$$

can interfere with each other. Here  $d$  is the distance between each lattice plane,  $\lambda$  is the incident wavelength,  $n = 1, 2, 3\dots$  is any positive integer. Thus the size of each lattice  $d$  can be calculated through the interference characteristics.

In a plasma, the electron density distribution can be regarded as a superposition of the background density profile and the density fluctuations. The density fluctuations are caused by the turbulence which can be pictured as many micro-sized blobs. The blobs near the cut-off layer can reflect the corresponding incident microwave. Due to Bragg condition, we know that the reflected microwave contains the information of the characteristic size of the turbulence eddies [131]:

$$K_{\perp} = 2k_0sin(\theta) \quad (3.23)$$

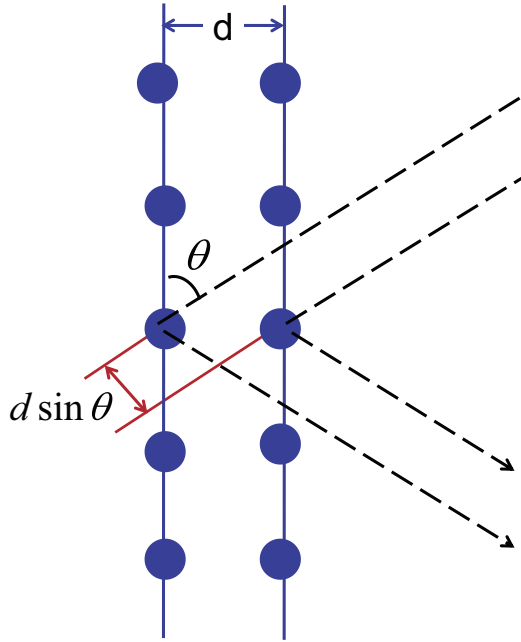


FIG. 3.6: Bragg scattering

where  $k_0$  is the wave vector of the microwave.  $K_{\perp}$  is the perpendicular wave number of the density perturbations. Therefore we can get the density fluctuation amplitude (through reflectometry principle in Section 3.2.2) of a certain turbulent wave number (through Bragg backscattering principle). For more details about the step-by-step derivation, please check J. Hillesheim's paper [129].

Moreover, those turbulence blobs usually propagate with a velocity  $\mathbf{v}$  in plasma, which produces a Doppler shift in the reflected wave frequency. And the shifted frequency is calculated by:

$$\Delta\omega_{turb} = \mathbf{v} \cdot \mathbf{K} \quad (3.24)$$

With measured Doppler shift frequency, the propagation velocity of the turbulent structures can be finally calculated [130].

### **3.3 Summary**

In this chapter, we discuss the theoretically based codes and experimental diagnostics that are crucial for studying turbulent particle transport. Two simulation packages of which one (ONETWO) solves the transport equations and the other (TGLF) is a quasi-linear gyrokinetic solver are introduced. Next we describe the basic principles of several essential diagnostics. These diagnostics measure the electron density, the electron temperature, the ion density, the toroidal rotation and the density fluctuation in the DIII-D tokamak.

# CHAPTER 4

## Turbulent particle transport as a function of toroidal rotation

### 4.1 Introduction

In this chapter we will study how toroidal rotation affects particle transport. Toroidal rotation in tokamaks is very important in that it can stabilize MHD instabilities [132, 133], reduce error field penetration [134], as well as determine global confinement in tokamaks [49, 45]. According to Lawson's Criteria [1], a high central density is eventually needed to achieve a high fusion gain in future magnetic confinement devices. However, the current predictive capability of particle transport in tokamaks is not well validated [135]. We still need to investigate how different plasma parameters can affect particle transport and confinement. Toroidal rotation is one of such parameters that we can use to help controlling the density profiles. Thus it is necessary to study the correlation between the toroidal rotation and the density.

As shown in Chapter 2, a significant amount of previous work has been done to investigate the role of collisionality and turbulence with respect to particle transport [81, 23, 82, 136, 38, 137, 78, 77, 79, 73, 38, 137, 24]. However, the role of toroidal rotation has historically received limited considerations in particle transport. Since the toroidal rotation is one of the contributions to the  $E \times B$  shear (see Equation 2.8), it plays an important role in determining confinement through the  $E \times B$  shear suppression of turbulent transport. This motivates us to investigate in more detail how toroidal rotation and rotational shear affect particle transport directly. In addition, because previous research on AUG has shown that the changes in the dominant mode can result in the changes of rotational shear and the local density gradient [23, 82]. We conduct our dedicated experiments on DIII-D to keep the same input power and fueling levels while only change the injected torque by using a mix of co- and counter- beam injection [21].

In this chapter, the toroidal rotation is altered by changing the injection direction of the neutral beams from co-torque to counter-torque, see Figure 4.1. Here co- and counter- refer to the direction correspond to the toroidal plasma current. A balanced torque can be obtained by turning on the same amount of co- and counter-torque injection. We study the effect of rotation, rotational shear, and the  $E \times B$  shear upon particle transport and confinement. The ion and electron temperature profiles remain identical and as a result the dominant instability turbulent mode is similar for all three discharges. Thus any changes in the density profile or the rotation profile will not be the result of a change in turbulence regime, but a direct result of a difference in injected torque and resulting  $E \times B$  shear. We find in DIII-D that the normalized density inverse scale length  $R/L_n = -\frac{R_0}{n_e} \frac{\partial n_e}{\partial R}$  is weakly correlated with the  $E \times B$  shearing rate, where  $n_e$  is electron density,  $R_0$  is the major radius. Moreover, we will show that the plasma which has the best density confinement, is the one whose shearing rate is larger than or similar to its microscopic turbulence growth

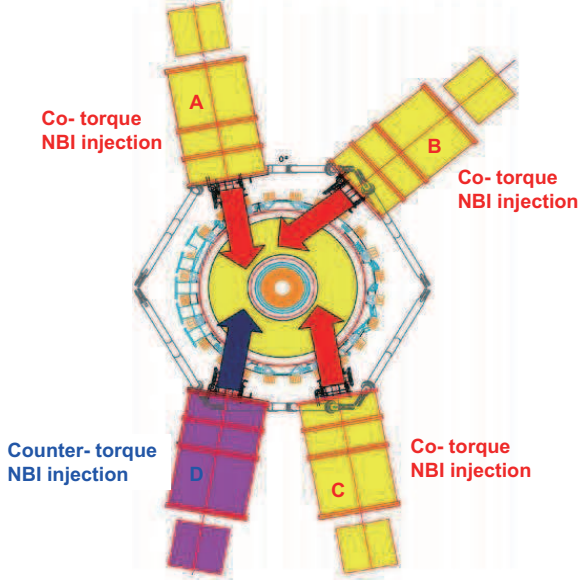


FIG. 4.1: Geometry of the DIII-D neutral beam injection system. Three of the beamlines inject power in the same direction as the usual plasma current (counter-clockwise in the diagram). We define these three as co-torque injection. One system is defined as counter-torque injection since its power is injected in the opposite direction. (Figure taken from DIII-D website, Neutral Beam Overview)

rate. Whereas the lowest density is observed in the balanced torque discharge, where the linear growth rate is larger than the  $E \times B$  shearing rate. We also find that the quasi-linear calculated particle flux by TGLF does not agree with the experimental particle flux. Neither does the linear growth rate as calculated with TGLF correlate with the observed density fluctuations. This indicates that more research needs to be done to validate the reduced linear transport model.

The chapter is organized in the following order. First, in section 4.2, we will discuss the experimental setup of these experiments as well as the linear stability calculations. In section 4.3 we will discuss the experimental particle flux along with the experimentally measured perturbed transport coefficients. Next, in section 4.4 we will show the changes in turbulence characteristics with a focus on the changes in  $E \times B$  shear along with the changes in growth rates and density fluctuations. Section 4.5 presents some comparisons between

TGLF simulations and the experimental results. We will conclude with a discussion and short summary.

## 4.2 Experiment setup

Our experiments were performed in the DIII-D tokamak with major radius,  $R \sim 1.67\text{ m}$  and minor radius,  $a \sim 0.67\text{ m}$ . The heating power is  $\sim 5\text{ MW}$  in these H-mode plasmas, with a line averaged density of  $3 - 4 \times 10^{19}\text{ m}^{-3}$ , see Figure 4.2. The toroidal

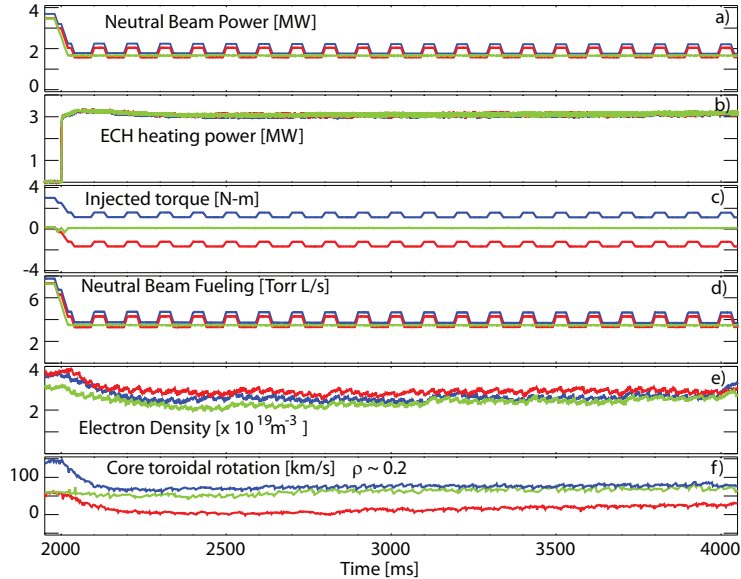


FIG. 4.2: Time evolution of three DIII-D H-mode discharges with different torque injection.(a) The NBI heating power for each discharge and the (b) ECH injected power are kept the same. (c) The NBI torque injection is varied from co- to counter-injected. (d) The fueling from the NBI is the same for all three discharges (e) The change in torque injection results in different line averaged electron density. (f) The core carbon rotation close to  $\rho = 0.3$  varies from co-rotating to zero rotation.

magnetic field is  $B_\phi = 1.9\text{ T}$  and the plasma current is  $I_p = 1.1\text{ MA}$ . In Figure 4.2, at  $2000\text{ ms}$ , the initial  $3.5\text{ MW}$  NBI power is reduced to  $2\text{ MW}$ , and  $3\text{ MW}$  of ECH power is added. The torque is varied from  $1.1\text{ Nm}$  in one discharge to  $0\text{ Nm}$  in the second discharge and  $-1.6\text{ Nm}$  in the third. The only fueling of the plasma comes from the NBI and the plasma-wall interactions, there is no additional gas puff during the H-mode phase

of these discharges.

We choose a steady state time slice for each of the three discharges and compare the profiles of different plasma parameters at these times. More specific, the chosen time slices are the time between two edge localized modes (ELMs). ELM is a periodic MHD instability occurring in the edge region of an H-mode tokamak plasma [138]). It can cause disruptions in plasma edge density and temperature and thus limits the measurement accuracy of those parameters. Figure 4.3 gives an example of how edge density changes before, during, and after an ELM crash in MAST (Figure taken from R. Scannell et. al Ref [139]. Note here that the MAST is a different tokamak to DIII-D, we use this figure only as an example to show how ELM affects the edge plasma density). We can see that during an ELM (red

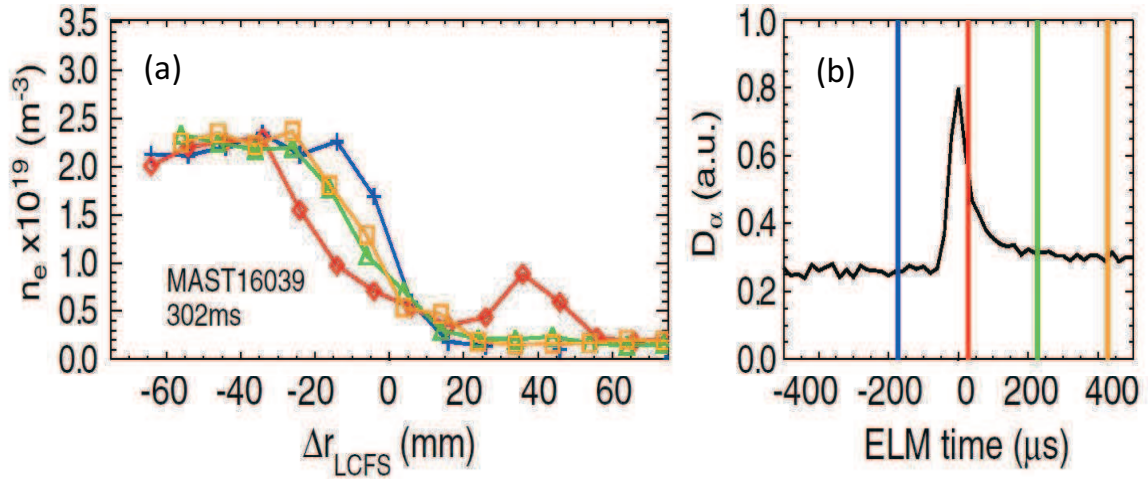


FIG. 4.3: Density profiles at the edge before and after ELM. The timing of measured density profiles (a) are shown on the  $D_\alpha$  measurement (b) with time interval of  $200\mu\text{s}$ . (Figure taken from R. Scannell et. al Ref [139])

line), the density profile collapses inward largely. The density then recovers gradually to its initial value (blue line) after the crash (see green and yellow lines). Therefore, in order to avoid the edge transport effects from ELM crashes, we choose the time slices which equal

80%-90%  $\tau_{ELM}$  after each ELM crash ( $\tau_{ELM}$  is the time interval between two ELMs). We can see that the change in injected torque results in a change in the core carbon rotation as measured by the Charge Exchange Recombination (CER) system [140] (see Chapter 3). Figure 4.4(a) shows that both the co-torque and the balanced torque discharges rotate in the co-current direction. For the counter-torque discharge, the toroidal rotation is in the counter-current direction within  $\rho \sim 0.3$  while is close to zero at  $\rho > 0.3$ . Here we use a polynomial fitting technique to fit the measured data (7th order polynomial fitting for rotation data and 5th order for the density and temperature data below). The unsymmetric co- and counter-torque rotation and the co-current directed balanced torque rotation indicate that an intrinsic torque in the co-current direction is presented in all three cases, similar as it has been shown in Solomon et al. Ref [141]. Moreover, in our experiments, the electron density is measured with the reflectometer system [120] and is verified with the Thomson Scattering system, the electron temperature profiles are measured using both the electron cyclotron emission (ECE) [123] and Thomson Scattering system [114], and the ion temperature profile is measured with the CER system (see Chapter 3 for all the diagnostics). Figure 4.4(c)(d) shows that both the co- and counter-torque discharges have a similar electron density profile as well as a similar inverse density gradient  $R/L_n$  within experimental error bars. However the balanced torque discharge has a much lower density and  $R/L_n$ . In Figure 4.4(e)(f), we can see the electron temperature profiles of all three discharges match well and are only marginally affected by the changes in toroidal rotation. Lastly, comparing the ion temperature profiles from Figure 4.4(g)(h), we see the co-torque discharge has a slightly higher  $T_i$ , however the ion temperature gradients in the region of interest for all three discharges are similar.

Previous research on AUG has shown that changes in the frequency of the dominant unstable mode can result in changes in rotational shear as well as the local density gradient

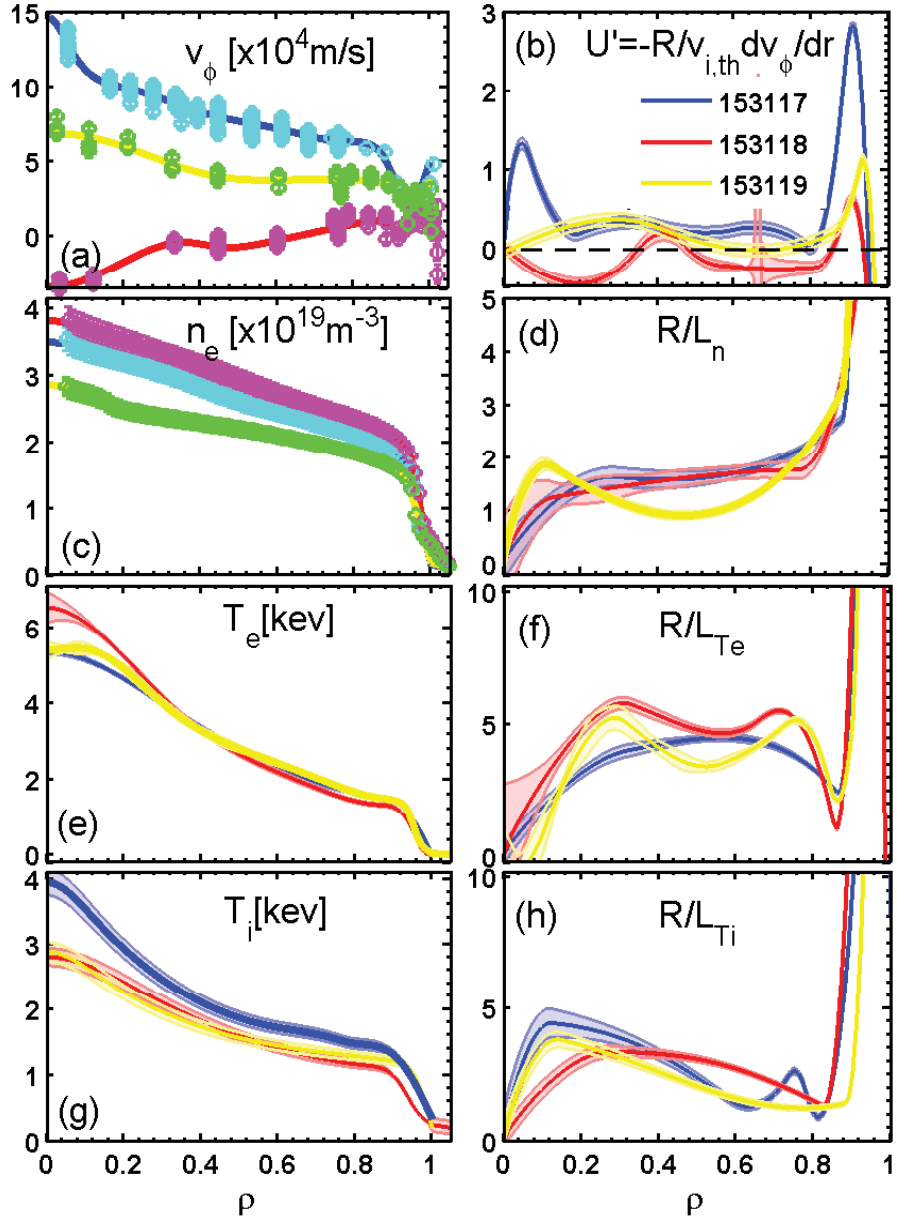


FIG. 4.4: Experimental fitted profiles and their inverse gradients for all three discharges (blue = co, yellow = balanced and red = counter injected NBI). (a-b) Due to the different injected torque the toroidal carbon rotation and its normalized gradient,  $u'$  are very different for all three discharges. (c-d) The electron density is the highest for the counter injected discharge and the lowest for the balanced injection.  $R/L_n$  for the co- and counter injected discharge are fairly similar. (e-f) The electron temperature profile is fairly similar for all three discharges outside  $\rho \sim 0.2$ . (g-h) The ion temperature is slightly higher for the co-injected discharge in comparison with the two other discharges.

[23, 82]. In order to study only the effect of toroidal rotation and control the changes of other variables, we need to verify that there is no change in the mode frequency. We use TGLF [20], a quasi-linear gyrokinetic code to calculate the linear growth rates and frequencies of the most unstable mode (see Chapter 3 for more details on TGLF). We use the experimental profile fits from Figure 4.4 as input to TGLF. For  $0 < k_\theta \rho_s < 1$  (where  $k_\theta$  is the poloidal wave-number,  $\rho_s$  is the ion sound radius), the frequency of the instability mode which has the largest growth rate (i.e., the most unstable mode) is extracted at each radial location. Figure 4.5 shows the mode frequency profiles of all three discharges. From  $\rho = 0.4 - 0.7$ , the frequency of the most unstable mode is positive, which means

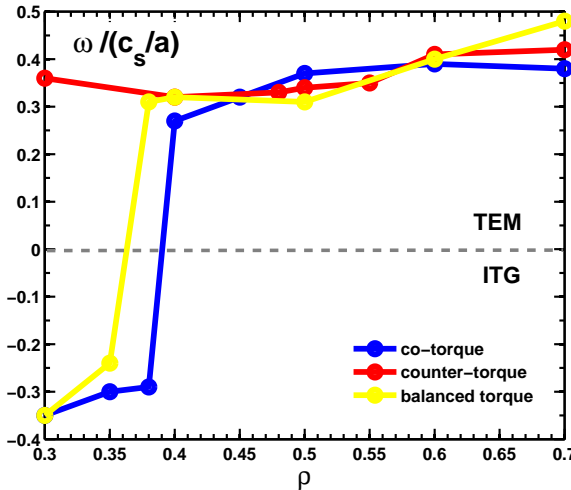


FIG. 4.5: Frequency of the most unstable mode for  $0 < k_\theta \rho_s < 1$  by TGLF. All three discharge are in TEM regime outside  $\rho = 0.4$  ( $\omega > 0$ ). Inside  $\rho = 0.4$ , the counter torque injected plasma is still in the TEM regime, whereas the other two discharges change to the ITG regime.

the turbulence drifts in the electron diamagnetic direction. Thus we can identify this mode as a Trapped Electron Mode (TEM), which is driven by both the density gradient and the electron temperature gradient. For the co-torque and counter-torque discharges, when  $\rho < 0.4$ , the mode frequency becomes negative, which means the drift direction of turbulence switches to the ion diamagnetic direction. As a result, the dominant mode can now be identified as an Ion Temperature Gradient (ITG) unstable mode. We can observe

from Figure 4.5 that not only is the frequency of the most unstable mode in the same drift direction (for  $\rho > 0.4$ ), but also the value of the frequency is similar. Therefore, we can assume that the changes in electron density and density gradient are not the result of a change in mode frequency and focus on the role of the toroidal rotation in determining particle transport. However, we need to note here, although typically the instabilities at small wave numbers dominate the changes in transport, GYRO simulations have shown that non-linear coupling can have a substantial effect on the heat flux [142]. We still do not know whether the non-linear effect from large wave number turbulence can play an important role in particle transport. Further discussion about the non-linear effect of the instability will be presented in Section 4.6.

## 4.3 Experimental particle transport changes

### 4.3.1 Particle flux

We use ONETWO, a one-and-half-dimensional code which solves transport balance equations to determine the fueling source from the beams and calculate the particle flux (readers can refer to Chapter 3 for more details of ONETWO). The particle balance equation that ONETWO solves is

$$\frac{\partial n_e}{\partial t} = -\nabla \Gamma_e + S_e \quad (4.1)$$

where  $n_e$  is the electron density,  $\Gamma_e$  is the particle flux and  $S_e$  is the fueling source. Figure 4.6(a) shows the total particle flux calculated by ONETWO. Since the central neutral beam fueling is proportional to the injected power and the NBI heating power is similar for all three discharges, we can see a similar particle flux in the core for all three discharges.

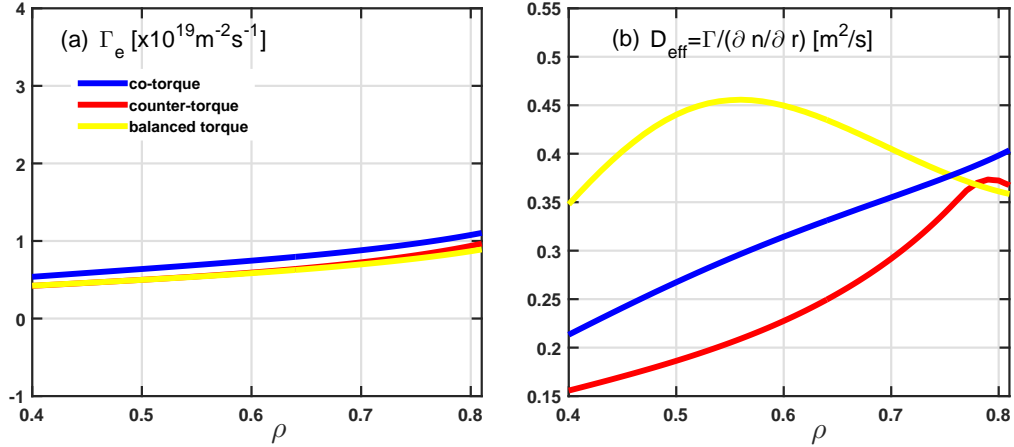


FIG. 4.6: Particle flux and effective diffusion coefficient profiles (a) Total electron particle flux determined using particle balance. (b) Effective transport as represented by an effective diffusion coefficient,  $D_{eff} = \Gamma / (\partial n / \partial r)$  for the 3 discharges.

Next we show in Figure 4.6(b) how steady-state transport coefficients varies. We calculate the effective diffusion coefficient which is defined as  $D_{eff} = -\Gamma_e / (\partial n_e / \partial \rho)$  in these three discharges.  $D_{eff}$  is an representation of the total change in radial transport. It includes both the particle pinch as well as the actual diffusion coefficient. As shown in Chapter 2, particle transport has multiple components, but these components cannot be extracted using steady state calculations. It is observed that, although the particle flux is similar for all three discharges, the changes in local density gradients (see Figure 4.4) result in different  $D_{eff}$ . We see the balanced torque discharge which has the lowest density profile (Figure 4.4(c)) has much larger effective diffusion coefficient from  $\rho = 0.2 - 0.7$ . While the co- and counter- torque discharges which have higher density profiles have smaller  $D_{eff}$ .

### 4.3.2 Perturbed transport coefficients

In previous section, we show that while the particle flux can be similar, particle transport can be very different (see Figure 4.6). Although we have studied the effective diffusion coefficient  $D_{eff} = -\Gamma / (\partial n / \partial \rho)$ , the actual particle flux equation should include both an

outward diffusion coefficient as well as an inward convection coefficient,  $\Gamma = -D \frac{\partial n}{\partial \rho} + v n$  (for more details, see Section 2.3). However, steady state measurement prevents us from getting both D's and v's at the same time since there is only one particle flux equation but two unknown variables. Therefore, in order to extract both the pinch and diffusion coefficient separately, we have to rely on the use of a perturbative gas puff technique.

The gas puff technique has been developed since 1980s and is used in more recent years (due to improved temporal and spatial diagnostic capabilities) to provide measurements of the perturbed diffusion coefficient  $D_p$  and the perturbed convection coefficient  $v_p$  [137, 143, 69, 144, 145, 36, 146]. This technique adds a periodic small gas puff into plasma, which modulates the density profile with a fixed periodicity. Figure 4.7 is an example from Ref. [137] showing how density evolves during two edge gas puffs (red overlay). The

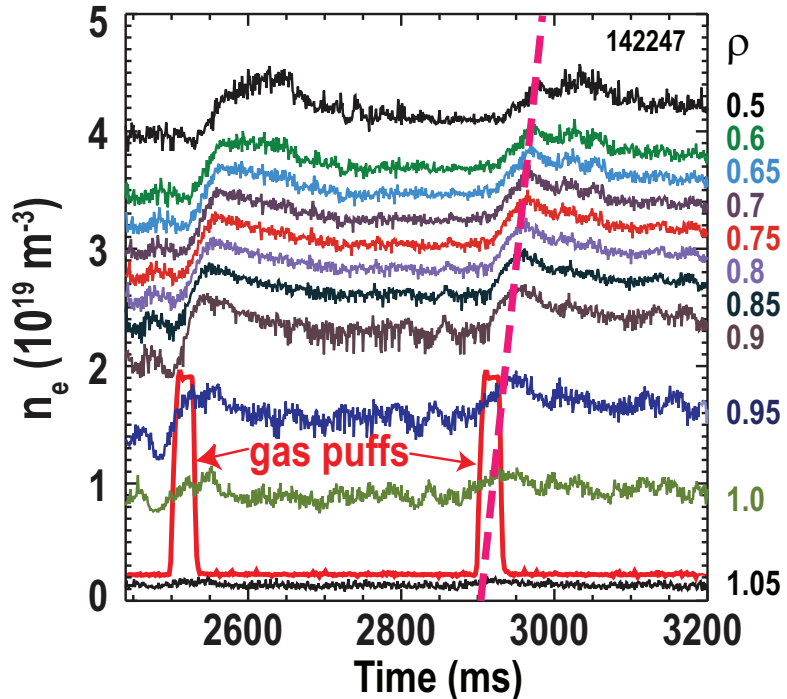


FIG. 4.7: Density evolution through two edge gas puffs. Density data measured by the DIII-D reflectometer system from mid-radius to the plasma edge.

time interval between two gas puffs is  $400ms$ . We can see clearly a gas-puff-induced density perturbation which propagates from the edge into the plasma core. Here the dashed line is only a guide to the eye and is not a fit to the data. We assume the density perturbation has the form of

$$\tilde{n}(\rho, t) = A(\rho) \exp(i[\omega t - \phi(\rho)])$$

Here  $A$  is the measured amplitude,  $\omega$  is the measured frequency, and  $\phi$  is the measured phase shift of the perturbed density  $\tilde{n}$ . We can extract the amplitude  $A$  and the frequency  $\omega$  by Fourier decomposing the modulated density profiles. Next we express the perturbed particle flux as  $\tilde{\Gamma} = -D_p \frac{\partial \tilde{n}}{\partial \rho} + v_p \tilde{n}$ . The continuity equation for the perturbed density can be written in the form of:

$$\frac{\partial \tilde{n}}{\partial t} = -\frac{1}{\rho} \frac{\partial}{\partial \rho} \left( -D_p \frac{\partial \tilde{n}}{\partial \rho} + v_p \tilde{n} \right) \quad (4.2)$$

Here we assume zero perturbation on particle source. Therefore, by replacing the perturbed density into Equation 4.2, we can derive the perturbed diffusion and convection coefficient:

$$D_p = -\frac{\omega(Y \sin \phi + X \cos \phi)}{\rho (\partial \phi / \partial \rho) A} \quad (4.3)$$

$$v_p = -\frac{\omega(\partial A / \partial \rho Y - \partial \phi / \partial \rho A X) \sin \phi}{\rho (\partial \phi / \partial \rho) A^2} - \frac{\omega(\partial A / \partial \rho X + \partial \phi / \partial \rho A Y) \cos \phi}{\rho (\partial \phi / \partial \rho) A^2} \quad (4.4)$$

where  $X = \int \rho A \cos \phi d\rho$  and  $Y = \int \rho A \sin \phi d\rho$ . More details about this technique can be found in H. Takenaga's paper [147]. Also, readers can refer to Doyle et al. [137] and Mordijk et al. [143, 69] for more experimental details on this technique for DIII-D plasmas.

We presents in Figure 4.8 the results of measured  $D_p$  and  $v_p$  of the three discharges. We can see that while the co-torque discharge and balanced torque discharge have similar  $D_p$  and  $v_p$ , the counter-torque discharge has a stronger convective inward pinch outside  $\rho =$

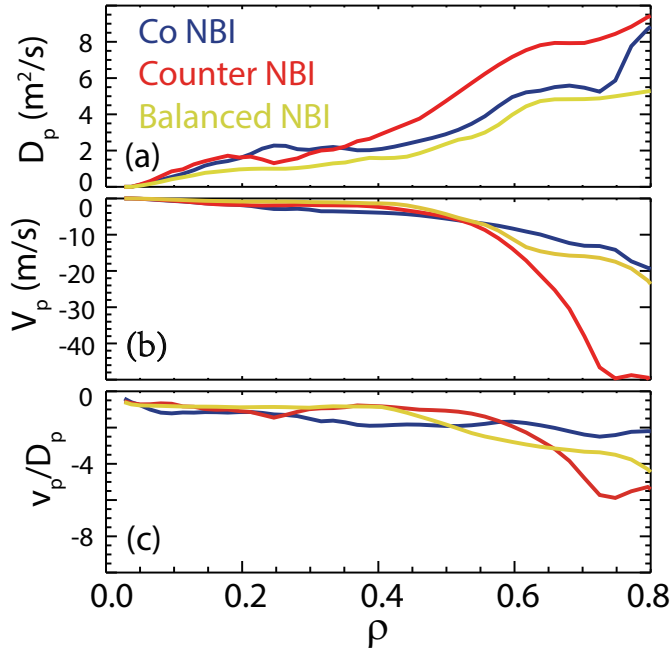


FIG. 4.8: Perturbative transport measurement for the three discharges: (a) Diffusive coefficients are similar in magnitude (b) Convective coefficients show that counter-torque discharge has a much larger inward pinch than the other two discharges outside  $\rho = 0.6$ . (c) The ratio of  $v_p/D_p$ .

0.6. This matches well with the observation in Figure 4.4(c) that counter-torque discharge has the highest electron density profile. Caution needs to be applied into over-interpreting these results. The Fourier analysis only results in the extraction of the perturbed transport coefficients and does not include the steady-state and perturbed fueling sources. Ongoing work on JET includes a non-linear optimization to extract the steady state transport coefficients, not just the perturbed transport coefficients [148]. However, this technique is still under development and cannot yet be applied to DIII-D plasmas.

## 4.4 Turbulence and $E \times B$ shear

### 4.4.1 Role of toroidal rotation in deciding $E \times B$ shearing rate

Toroidal rotation can indirectly affect particle transport, through its contribution to the radial electric field  $E_r$  and thus the  $E \times B$  shearing rate. Recall the radial electric

force balance equation 2.8 and the  $E \times B$  shearing rate definition equation 2.9 in Chapter 2 [49, 50]:

$$eE_r = e(Z_i en_i)^{-1} \nabla P_i - ev_{\theta_i} B_\phi + ev_{\phi_i} B_\theta \quad (4.5)$$

$$\omega_{E \times B} = \frac{(RB_\theta)^2}{B} \left( \frac{\partial}{\partial \Psi} \right) \frac{E_r}{RB_\theta} \quad (4.6)$$

Here,  $Z_i$  is the net particle charge of species  $i$ ,  $P_i$  is plasma pressure,  $v_i$  is the plasma velocity and  $\theta$  and  $\phi$  denote poloidal and toroidal direction respectively,  $B$  is the magnetic field and  $\Psi$  is the poloidal flux. On the right hand side of equation 4.5, there are three terms (plasma pressure, poloidal rotation, and toroidal rotation) that contribute to the radial electric field  $E_r$ . As an example, for the co-current discharge, Figure 4.9 shows the magnitude of each component. We can see that the contribution from toroidal rotation  $v_{\phi_i} B_\theta$  takes the largest portion of the total electric field (except in the edge where the diamagnetic term dominates, see pink line in Figure 4.9). Since the poloidal magnetic field  $B_\theta$  is fixed, a change in toroidal rotation profile can cause a consequent change in  $E_r$ . Next, with the radial electric field calculated, the  $E \times B$  shearing rate can be obtained via equation 4.6. Figure 4.10 shows a correlation plot between the  $E \times B$  shearing rate and the normalized density inverse scale length  $R/L_n$  at  $\rho = 0.5 - 0.8$  from a database of DIII-D plasmas. We can see a weak correlation between the local  $E \times B$  shearing rate and the local peaking of the density for  $\rho = 0.5 - 0.8$ . Here the  $E \times B$  shearing rate is based on measured quantities only (Carbon was the ion species used by the CER system). While the density gradient has a contribution in the  $\omega_{E \times B}$  (see diamagnetic component in Figure 4.9), there were large variations in the electron temperature gradient, ion temperature gradient, and rotation shear which can affect turbulence drive and thus eliminating any trends related to the density gradient. In the next section we will study the role of the  $E \times B$  shearing rate in determining particle confinement by comparing the three dedicated

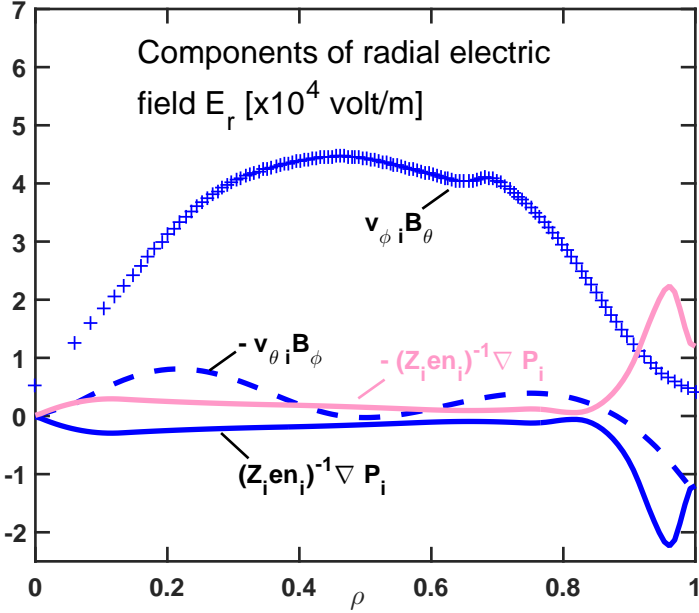


FIG. 4.9: Components of radial electric field for the co-current discharge from the plasma pressure gradient (solid line), the poloidal rotation (dashed line), and the toroidal rotation (cross dotted line).

discharges in which we varied the torque injection.

#### 4.4.2 Growth rate versus $E \times B$ shearing rate

As discussed in Chapter 2, previous research has shown that shear flow can tear apart turbulence eddies and thus reduce the turbulent transport [45, 46, 43, 49, 48]. Sheared flow, such as the  $E \times B$  shear, suppresses turbulence in two ways [49]; through nonlinear de-correlation, which includes the reduction in the turbulence radial correlation length, phase, and fluctuation size; or through linear stabilization, which enhances the damping of turbulence by coupling the unstable modes to nearby, stable modes, thus improving the overall stability of the system. Although the radial electric field (and thus the  $\omega_{E \times B}$  rate) is dominated by the pressure gradient in the pedestal region, as it goes deeper inside the core, the toroidal rotation contribution is more important (see Figure 4.9) [149]. As shown

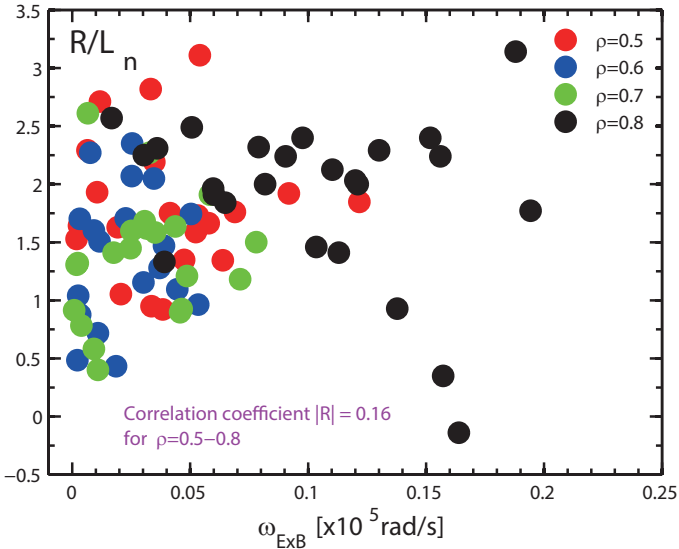


FIG. 4.10: Correlation plot : Inverse density gradient,  $R/L_n$  as a function of  $E \times B$  shearing rate  $\omega_{E \times B}$  for low density H-mode discharges in which the ratio of  $T_e/T_i$  is varied.

in Figure 4.11, the  $E \times B$  shearing rate in our set of three discharges changes due to the variations in toroidal rotation. We can see that the change in toroidal rotation has the strongest effect from  $\rho = 0.6 - 0.8$ . Outside  $\rho = 0.8$  the changes in the pressure gradient dominate and inside  $\rho = 0.6$  the shearing rate is small and the local difference between the discharges are related to fitting choices. Figure 4.11 shows that the discharge with balanced torque (yellow line) injection has the lowest  $\omega_{E \times B}$ , while the co- (blue line) and counter-torque discharges (red line) have a higher shearing rate from  $\rho = 0.6 - 0.8$ .

The  $E \times B$  shearing rate by itself is only an indication of how strong the shear is. The strength of the turbulence drive is also crucial. In a simplified picture, without including non-linear effects, the rule of thumb is that if the linear growth rate is smaller than the shearing rate, the mode will be suppressed, whereas if the linear growth rate is larger than the shearing rate, the mode will not be suppressed. This rule of thumb has been observed before on DIII-D, where the toroidal rotation is strongly modified using

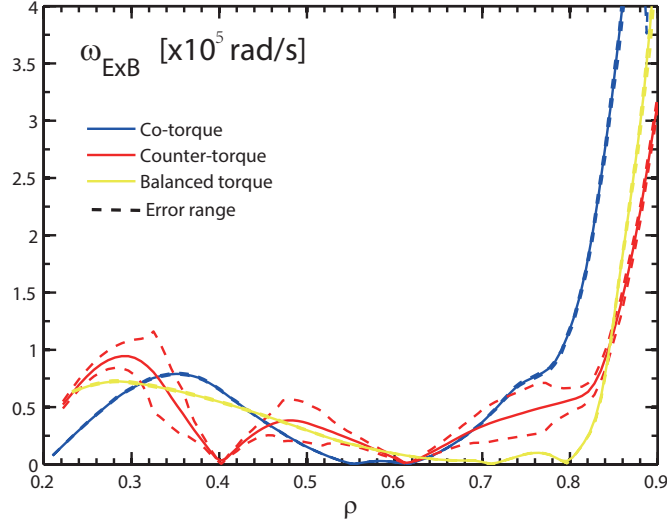


FIG. 4.11:  $E \times B$  shearing rates (using Hahm-Burrell [49]) for the three discharges with different torque injection.

Resonant Magnetic Perturbations [143]. When we compare the linear growth rate to the  $E \times B$  shearing rate in our experiment (see Figure 4.12), we find that ,for the co- (Figure

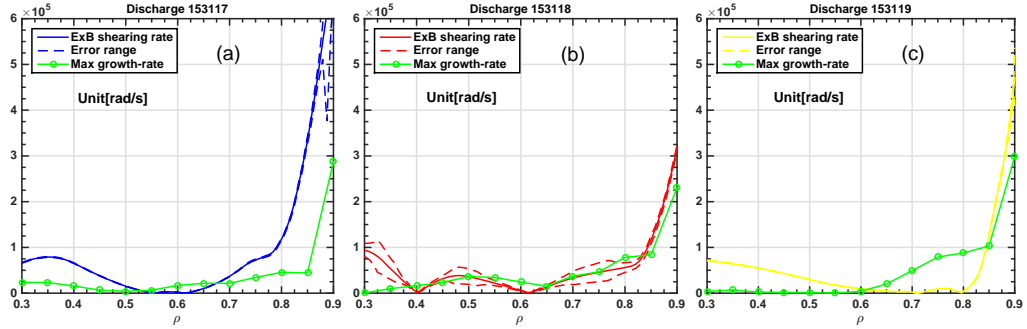


FIG. 4.12:  $E \times B$  shearing rates versus the maximum growth rates for  $k_\theta \rho_s = 0.1 - 0.5$ . Three  $E \times B$  shearing rates are labeled with different colors: (a) co-torque (Blue), (b) counter-torque (Red), and (c) balanced torque (Yellow). All the growth rates are represented by the green lines.

4.12(a)) and the counter-torque injected discharges (Figure 4.12(b)),  $\omega_{E \times B}$  is larger than or of similar to the maximum linear growth rate from  $\rho = 0.6 - 0.85$ . Whereas for the balanced torque injected discharge (Figure 4.12(c)), the  $E \times B$  shearing rate is much smaller than

the average linear growth rate. Thus based on the simplified rule, the balanced torque discharge will be less able to suppress turbulent transport from outside the mid-radius up to the top of the pedestal. However, the comparison between  $\omega_{E \times B}$  and the growth rate is based on a simplified linear picture. As mentioned in the beginning of this section, the  $E \times B$  shear flow can also result in the non-linear de-correlation of the turbulent eddies. Since we lack a direct 2D visualization measurement of the actual eddies, we cannot tell whether it is because the modes at smaller  $k_\theta \rho_s$  are suppressed or whether it is because of the de-correlation of these modes that results in a decrease in transport and improvement in confinement.

#### 4.4.3 Density fluctuations

As the last part of this section, we present the profile of experimental measured density fluctuations, see Figure 4.13. The density fluctuation is measured by the Doppler BackScattering (DBS) [129]. In our experiment, the DBS measures density fluctuations range in  $k_\theta \rho_s = 1.6 - 2.8$ , i.e., at the intermediate scale. This intermediate scale is typically associated with the TEM unstable regime. In Figure 4.13, from  $\rho = 0.6 - 0.75$ , we observe that the balanced torque discharge has slightly higher  $\tilde{n}/n$  than the other two discharges. While from  $\rho = 0.75 - 0.9$ , the density fluctuation of counter-torque discharge has a large increase and there is no data for the co and balanced discharge. Outside  $\rho = 0.9$ , density fluctuations of all three discharges are similar.

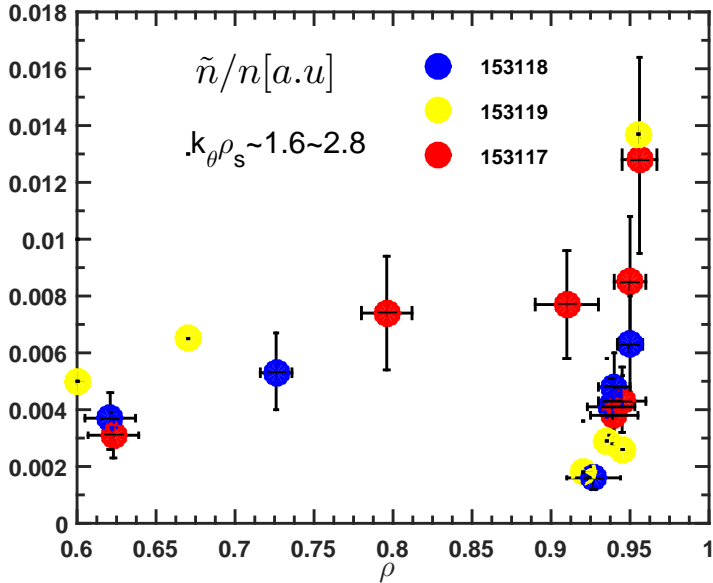


FIG. 4.13: Density fluctuation profiles Density fluctuations measured by DBS at intermediate scale ( $k_\theta \rho_s = 1.6 - 2.8$ ) for all three discharges.

## 4.5 Comparison with theory

### 4.5.1 Growth rate and frequency spectrum

The quasi-linear gyrokinetic code (TGLF) we use in this chapter, despite lacking precision in large wave number region, can produce well calculations of the dominant mode frequency and growth rate spectrum. Figure 4.14 shows the frequency and growth rate spectrum of all three discharges with x-axis the radial distance and y-axis the normalized wave-number. We can see from Figure 4.14(a-c), in the core part ( $\rho < 0.4$ ) of co-torque and balanced torque discharges, the plasmas are under ITG regime. While outside  $\rho = 0.4$ , for all three discharges, we see the signs of frequency are positive and thus all three discharges are in TEM regime. One feature of this intermediate scale TEM instability is, its growth rate usually peaks within  $1 < k_y \rho_\theta < 2.5$  [142][150] and is usually larger than the growth rate of ITG mode Figure 4.14(d)-(f). Also, we can see the instability growth rate maintains the magnitude of same level at  $\rho = 0.6 - 0.7$ , which address the importance of  $E \times B$  shear

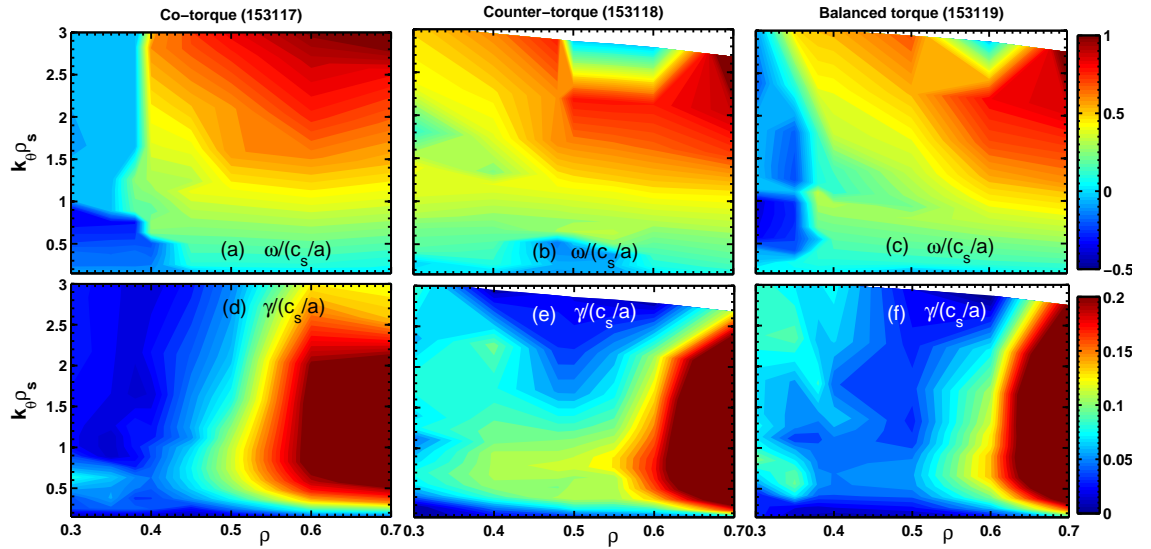


FIG. 4.14: Frequency and growth rate spectrum calculated by TGLF: (a-c) Frequency spectrum at each radial location. We see all three discharges are in TEM regime outside  $\rho = 0.4$  ( $\omega > 0$ ). (d-f) Growth rate spectrum at each radius. TEM instability's growth rate peaks in  $0.5 < k_\theta \rho_s < 2.8$  and is growing larger as it goes to the edge

change on particle confinement.

#### 4.5.2 Quasi-linear turbulent particle flux

Next we present a comparison between the TGLF calculated particle flux and the experimental particle flux got from Section 4.3.1. TGLF can calculate the turbulent particle flux at each  $k_\theta \rho_s$  for the different radii. Thus we can extract the quasi-linear particle flux at different radial locations by integrating over  $k_\theta \rho_s = 0 - 1$ . The difference between the TGLF calculated turbulent flux and the experimental results is that, the calculation of the experimental flux is based on the radial integral of the source, whereas TGLF does not know anything about the fueling sources, the TGLF calculations are based upon local gradients. The solid lines in Figure 4.15 show the total particle flux from ONETWO while the dashed lines show the quasi-linear turbulent particle flux from TGLF. Comparing these two flux results, we find that, even considering the range of error bars, there is still an

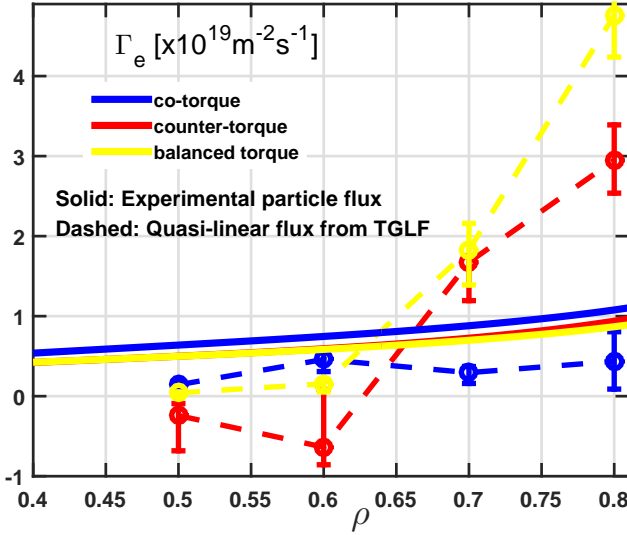


FIG. 4.15: Particle flux profiles for the 3 discharges. Total electron particle flux (solid lines) determined using particle balance; the dashed lines are the calculated quasi-linear calculated electron flux with TGLF.

large mismatch between the quasi-linear flux and the experimentally measured flux. Here we calculate the error bars by varying separately the gradients such as  $R/L_n$ ,  $R/L_{Te}$ , or  $R/L_{Ti}$  by 10%, and then choose the largest variation as the upper bound and the lower bound of each point. We can see that, in the co-torque injected discharge, although the quasi-linear flux follows the same trends as the experimental flux, it is still a factor 3 too small. For the counter-torque injected discharge, the quasi-linear flux has a negative value between  $\rho = 0.5$  and  $\rho = 0.6$  and then increases largely above experimental values when towards plasma edge. Finally, for the balanced-torque injected discharge, the calculated quasi-linear particle flux also exceeds the experimental observations outside  $\rho = 0.6$ .

### 4.5.3 Density fluctuations versus growth rate

We have shown the experimental density fluctuations at  $k_\theta \rho_s = 1.6 - 2.8$  in Figure 4.13. In a simplified linear picture, if we re-consider here Equation 2.7 in Chapter 2,

$$\tilde{n} = n_0 \exp(i\mathbf{k} \cdot \mathbf{x} - i\omega t), \quad \text{where } \omega = \omega_{freq} + i\gamma \quad (4.7)$$

here  $\tilde{n}$  is the perturbed density,  $n_0$  is the local plasma density,  $\omega_{freq}$ ,  $\gamma$  denote the instability modes frequency and its growth rate,  $\mathbf{k}$  is the wave number. We can see the equation indicates that the growth rates should have same trend of change as to the actual density fluctuations at the same scale. Figure 4.16 shows the average linear growth rate profile for the same  $k_\theta \rho_s = 1.6 - 2.8$  scale. We observe that, outside  $\rho = 0.9$ , the linear growth rates

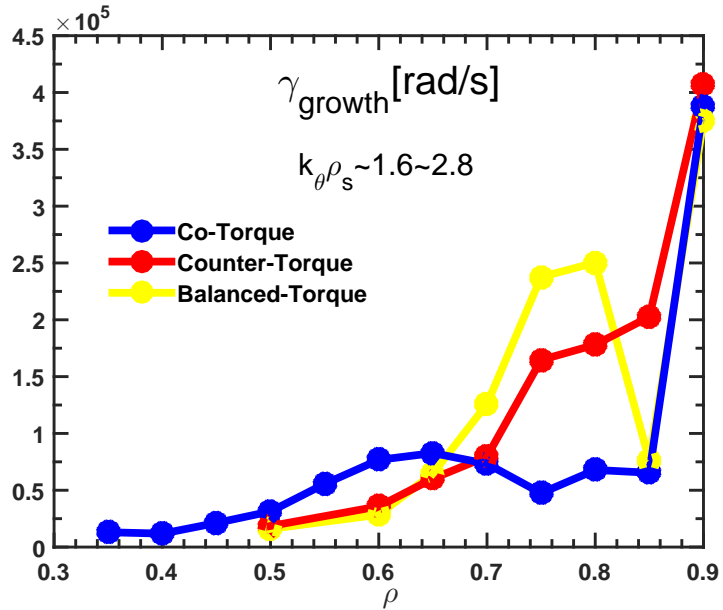


FIG. 4.16: Linear growth rate profiles The average linear growth rate for  $k_\theta \rho_s = 1.6 - 2.8$ .

seem to qualitatively agree with the observed density fluctuations. However, considering the fact that there is no data for the co and balanced injected discharge, it is impossible to compare the trends between  $\rho = 0.7 - 0.9$ .

To sum up, in this section, we find that there is a mismatch between the quasi-linear calculated turbulent flux and the experimental flux. The linear growth rates also do not match the experimental density fluctuations. One of the explanations can be that, for now, the linear calculation can not capture all the physics on microscopic and macroscopic scales, non-linear effects play an important role in turbulent transport and that a full non-linear gyrokinetic simulations would result in a better agreement. As an example, non-linear multi-scale gyrokinetic simulations of C-mod results [150] have already shown to increase the heat flux by 30% in comparison with ITG-only non-linear gyrokinetic simulations. But it is still unclear now whether a fully non-linear multi-scale gyrokinetic simulations will result in a change of the particle flux. Further research is needed to study whether non-linear gyrokinetic simulations can make a different with quasi-linear results for particle transport.

## 4.6 Discussion

In this chapter we study the effects of toroidal rotation on particle transport. In three dedicated discharges of low density H-mode plasmas on DIII-D, we keep the frequency of the dominant unstable mode the same and only change the input torque (from co- to counter- torque). The profile of toroidal rotation and electron density is changed while the electron temperature remains similar of all three discharges, see Figure 4.4. In addition, the changes in toroidal rotation can feed into the  $E \times B$  shearing rate via changing the radial electric field. Thus, we can vary the  $E \times B$  shear substantially from  $\rho = 0.6 - 0.8$  by altering the injected torque. The ability of the  $E \times B$  shear to regulate particle confinement from mid-radius to the top of the pedestal has been found previously during the application of Resonant Magnetic Perturbations (RMPs) [143] (a technique using mag-

netic perturbations to control ELMs in tokamak plasmas) and in Quiescent H-mode [151] (a high confinement plasma operation mode without the disruption from one of the plasma instabilities called edge localized modes (ELMs) [152]). In both cases, a reduction in particle confinement is observed when the linear growth rate for small  $k_\theta \rho_s$  is larger than the  $E \times B$  shear. However, there are many differences between our experiments and the previous experiments in the QH-mode and the RMP H-mode on DIII-D. One example is that, the former experiments would change the temperature gradients and thus change the underlying linear instability, while in this dedicated set of three discharges the temperature gradients are similar and, as a result, the frequency of the most unstable mode is similar for all three discharges in which the torque was varied.

Another example of the turbulent particle transport suppression by  $E \times B$  shear is the observation of an Internal Transport Barrier (ITB) on TFTR, where the magnetic shear reversal cannot explain the improvement in confinement [153]. Different from the approach of our experiment, the change of the  $E \times B$  shear in this case is not the result of a change in toroidal rotation, but is due to the steep pressure gradients formed in the ITB region. For the ITB case, the mechanism of turbulence suppression is more comparable to the formation of the pedestal during the L- to H-mode transition [154], where eventually the gradients in the pedestal provide the shear to maintain the pedestal through suppression of turbulent transport.

Next, we will discuss the perturbed diffusion coefficient  $D_p$  and the perturbed convection coefficient  $v_p$  measured by gas puff technique. As shown in Section 4.3, the perturbed transport coefficients indicate that the changes in transport are not only just the result of changes in outward diffusion, but also the changes in inward convection. However, we need to be careful that the perturbed transport coefficients are not equal to the transport coeffi-

ients in steady state. This is because although the perturbations to the density are small, this can still affect the local gradients. Currently it is still unclear whether the perturbed coefficients can accurately reflect the physics of steady-state transport. In order to connect the perturbed transport coefficients to the background steady state transport coefficients, a non-linear optimization is needed, which includes not only the perturbed density profiles, but also the steady-state density profile, and the perturbed fueling sources. Initial progress on this topic has been made on JET, but the technique is still being tested and developed [148].

Finally, we report another interesting finding from our experiment. In one recent paper by S. Mordijk et al. [69] where  $T_e/T_i$  is varied on DIII-D H-mode plasma, a correlation between a strong increase in perturbed inward particle pinch and an increase in intermediate scale density fluctuations is observed around  $\rho = 0.6$ . In our experiment, we find a similar correlation. For the counter-torque discharge, a strong inward particle pinch happens around  $\rho = 0.8$  (Figure 4.8(b)), this is the same radii where the strong increase in intermediate scale density fluctuations occurs (see Figure 4.13(a)). This correlation provides the possibility of turbulence drive inward pinch in plasma edge and thus is worth further research.

## 4.7 Conclusion

In this chapter we present the first dedicated study on how changes in toroidal rotation affect particle transport and confinement. While keeping the underlying turbulence drive unchanged, we vary the toroidal rotation by changing the injected torque in co-current, counter-current, and balanced directions. We find that there is a correlation between  $R/L_n$  and the  $E \times B$  shear. A reduction in particle confinement is observed in balanced torque

discharge when the  $E \times B$  shear is lower than the linear growth rate at small  $k_\theta \rho_s$  outside mid-radius. However, when the  $E \times B$  shear is larger than or at least similar as the linear growth rate, the density profile as well as the plasma peaking increases. In addition, quasi-linear gyrokinetic simulations of the particle flux using TGLF do not match experimental observations. This suggests that more future work need to be made to validate the quasi-linear gyrokinetic simulations in order to improve the ability in predicting density profiles. Finally, the perturbed transport coefficients which are measured by gas puff technique indicate that changes in transport are not only just related to an increase in outward diffusion, but also related to the changes in inward pinch. In the counter-torque injected discharge, a strong increase in the perturbed inward pinch is observed at the plasma edge. An increase in intermediate scale density fluctuation is also observed at the same radius. This correlation is similar as it has been reported in Ref [69].

# CHAPTER 5

## The determination of local density gradient by the local turbulence regime

### 5.1 Introduction

In Chapter 4, we have shown that the balanced torque injected plasmas can result in a reduction in confinement. This reduction can become a big concern for future burning plasmas devices such as ITER [155], since ITER will have no external momentum source. One way to counter the confinement loss due to changes at the plasma edge is through an increase in peaking of the core density. There are three known mechanisms to affect the density gradient in the core: collisionality [77, 78, 79, 61, 73], frequency of the dominant turbulent mode [22, 68, 82, 23, 82], and the q-profile driven by plasma current ( $q$  is the plasma safety factor defined as:  $q = \frac{rB_\phi}{RB_\theta}$ , where  $r$  and  $R$  denote length in minor and major radii) [66, 77, 78]. As discussed in Chapter 2, in JET H-mode discharges [77, 78, 79], results

from an extensive database analysis of density profiles in stationary conditions show that the density peaking increases 25% as the effective plasma collisionality decreases from 1 at mid-radius to below 0.1. However, on DIII-D, in a set of dimensionless scaling experiments, no increase in density peaking was observed when collisionality was reduced by a factor of 2 in both H-mode and L-mode discharges [137]. Another component in determining the density profile is the q-profile, through the curvature pinch. Density peaking is observed to increase when the plasma current drive (proportional to  $1/q$ ) increases on JET [66, 77, 78]. A similar correlation between the density peaking and q-profile is also observed on DIII-D, where the correlation is more pronounced when  $T_e = T_i$  and less pronounced when  $T_e > T_i$  and the plasma is in a TEM turbulence regime. Finally, in this chapter, we will investigate the role of the linear mode frequency in determining the density profile in the core. Particularly, we will focus on the dependence of electron density gradient on frequency of the most unstable mode.

In recent years, both gyrokinetic simulations [22, 68, 82] and experiments in AUG [23, 82] have reported a connection between the electron density gradient and the frequency of the linear microinstability mode. The inverse density scale length  $R/L_n = -\frac{R_0}{n_e} \frac{\partial n_e}{\partial R}$  is found to maximize near the ITG-TEM transition and decreases towards both the ITG and the TEM regimes. Here  $n_e$  is the electron density,  $R_0$  is the major radius. This interesting dependence was first derived theoretically by assuming little turbulent particle flux in Ref. [22] and then found in a set of L-mode and H-mode discharges across different plasma parameters at  $r/a = 0.45$  on AUG [23]. Here  $r$  denotes length of the minor radii,  $a$  is the minor radius. The dependence seems to be universal in describing the density peaking under various experimental conditions, such as L- and H-mode plasmas, whether the plasmas are dominantly ion heated or dominantly electron heated. However, the AUG experimental results only report the dependence at  $r/a = 0.45$  [23]. These results have

yet to be confirmed on other experimental devices nor at other radial locations. More validation is still needed.

In this chapter, we report for the first time on DIII-D the dependence of  $R/L_n$  on frequency of the unstable mode. Counter to AUG, we investigate this correlation time-dependently with a 3MW ECH pulse added into a steady neutral beam heated H-mode plasma on DIII-D. Instead of steady states, we are looking at the dynamic ITG-TEM transition process in our experiment. We use a polynomial fitting method to fit the electron density data in time evolution direction during the whole process. The same fitting is performed at all radial locations so that a 2D figure in both time and spatial directions can be drawn for the density data. With this smoothed fits, the electron density gradient can be calculated. On the other hand, TGLF can calculate frequency of the turbulence in one time point using profiles of different plasma parameters at that exact time. Thus together with time-dependent fitted  $R/L_n$  and time-independent calculated frequency of mode, we find that the electron density gradient in plasma core shows a dependence on the most unstable mode frequency. That is, when the absolute frequency of the dominant unstable mode decreases in the ion temperature gradient (ITG) regime, local density peaking increases. Once the dominant mode switches over to the trapped electron mode (TEM) regime, the local peaking of the density decreases again. As a result the density gradient reaches a maximum where the turbulence regime switches over from ITG to TEM. This dependence is in agreement with theoretical prediction [22] and experimental results on AUG [23]. However, when we move to the plasma edge, the dependence between  $R/L_n$  and frequency of instability mode disappears. In addition, to study how particle transport changes during the ITG-TEM change, we calculate the radial integral of the electron density changing rate  $\int_0^r \frac{dn_e(r,t)}{dt} dr$  and compare it with the mode frequency. Since core fueling is a constant during our discharge, the integral of  $dn_e/dt$  is a good reflection of how the

electron flux changes. We observe that the electron density changing rate also peaks near the ITG-TEM transition, which indicates that the particle flux in this discharge is largely affected by changes in turbulence.

We will firstly describe our experiment set up in Section 5.2. The next section, 5.3, presents all the fitting methods that are used to fit the raw density data, along with the comparison of their fitting errors. In Section 5.4, the correlation between the density gradient  $R/Ln$  and the instability mode frequency is presented. We then calculate the electron flux assuming the core fueling is not affected by changes in electron flux  $\Gamma_e$ , ion flux  $\Gamma_i$ , and  $n_e$  in Section 5.5. This chapter will end with a discussion section and a summary section (Section 5.6, 5.7).

## 5.2 Experiment set-up

We conduct our experiment in the DIII-D tokamak[19] whose major radius  $R_0 = 1.67m$  and minor radius  $a = 0.67m$ . The plasmas are low density, low collisionality H-mode plasmas heated by a constant neutral beam injection, see Figure 5.1(a). The central toroidal magnetic field is  $B_T = 1.88T$  and the plasma current is  $I_p = 1.1MA$ . The plasma's safety factor is around  $q_{95} \approx 4.2$  and the normalized plasma pressure is among  $\beta_N = 1 - 1.5$ . As shown in Figure 5.1(a), at  $2500ms$ ,  $3.2MW$  electron cyclotron heating (ECH) power is added. It lasts for  $500ms$  and is reduced to  $1MW$  at  $3000ms$ . The second ECH pulse starts at  $3500ms$  with the same  $3.2MW$  power and the same duration time  $500ms$ , after which it is again reduced to  $1MW$  at  $4000ms$ . The core injected neutral beam power is kept at  $3MW$  so that the beam fueling and heating is the same at all times, see Figure 5.1(b). We see from Figure 5.1(c)-(f), for each ECH pulse, the electron temperature increases while the line averaged density, ion temperature, and the impurity rotation decrease. Moreover,

we can see that it takes much less time for the electron temperature to reach a new steady state than the electron density.

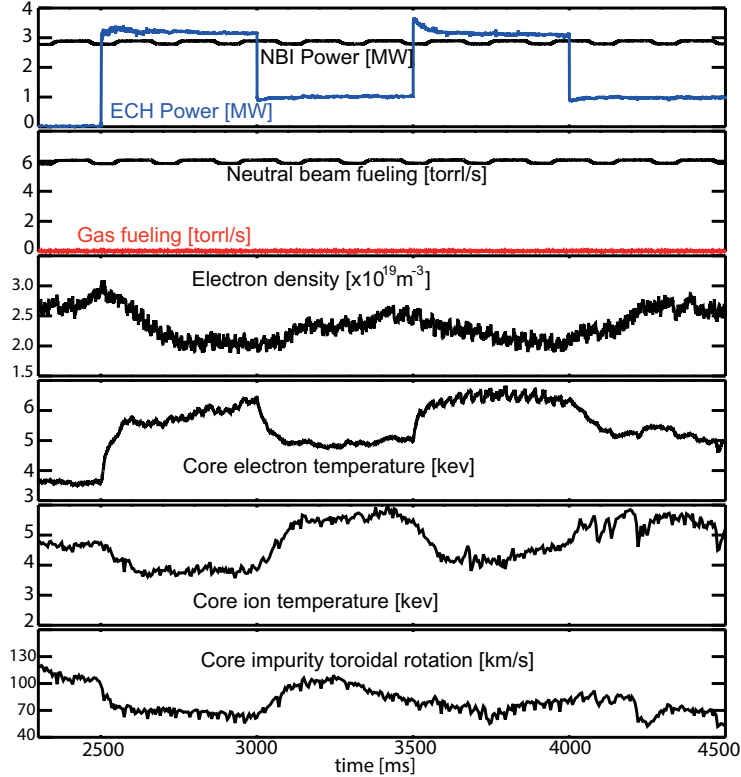


FIG. 5.1: Time evolution figures of a DIII-D H-mode discharge with periodic added ECH pulses.(a) The NBI heating power is kept same and a 500ms long ECH pulse (3.2 MW) is injected every 1000ms after 2500ms. (b) The fueling from both the NBI and the edge gas puff are the same at all time. The periodic injected ECH pulses result in different (c) line averaged electron density, (d)Core electron temperature, and (e) Core carbon toroidal rotation.

The electron density in this experiment is measured by the Reflectometer system [120] and has been compared to the Thomson Scattering system (see detailed comparison in the next chapter). The electron temperature profile data comes from both the electron cyclotron emission (ECE) system [123] and the Thomson Scattering system [114]. The ion temperature and the impurity toroidal rotation are measured by the charge exchange recombination (CER) system [140]. In the DIII-D tokamak, the reflectometer system can provide temporal resolution of  $25\mu s$  for the density range of  $n_e = 0 - 6.2 \times 10^{19} m^{-3}$  for

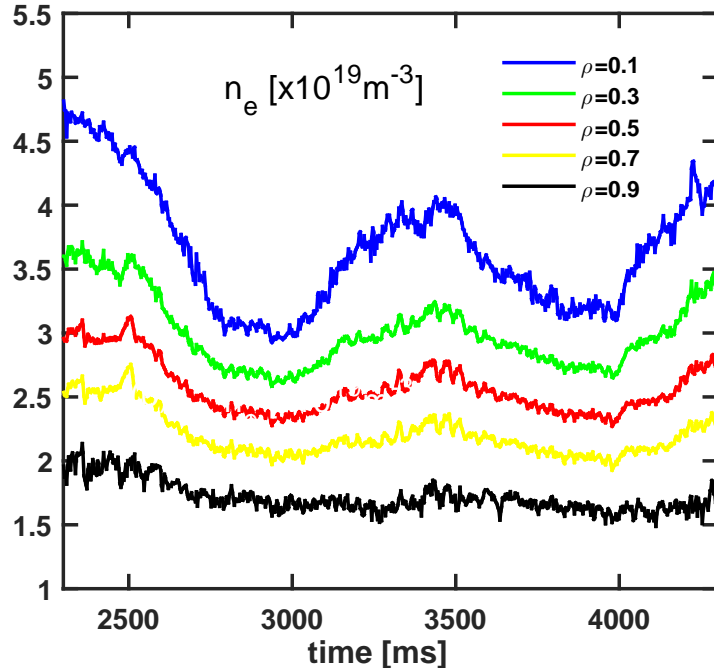


FIG. 5.2: Measured electron density data. Time evolution of the electron density at different radial locations.

$B_t > 1.6T$  [120]. It also has a spatial resolution of  $\approx 0.4cm$ . Figure 5.2 presents the time evolution of electron density at different radial locations. We can observe that, during the first ECH pulse ( $2500 - 3000ms$ ), the electron density is pumped out as time evolves (along the x-axis), and the pump-out happens at all radial location (along the y-axis). This periodic decrease of  $n_e$  can repeatedly be seen during the successive ECH pulses. Moreover, if we set time  $t$  as the x-axis and normalized radial location  $\rho$  as the y-axis (here  $\rho$  is calculated by normalizing the square root value of each flux surface, it ranges from 0 to 1 and is typically used as a coordinate to reflect the radial extent in a tokamak cross section), a 2D contour plot can be drawn (see Figure 5.3). The 2D plot presents a clearer and more direct way to show the changes in both temporal and spacial direction. We will use 2D plot repeatedly in the following sections and in Chapter 6.

## 5.3 Data fitting

Although the high resolution electron density measurement can show the pump-out phenomenon in ECH plasmas, the raw data is too scattered if we want to calculate the density gradient versus time (i.e.,  $dn/dt$ ) and versus radius (i.e.,  $dn/d\rho$ ) directions. Figure 5.3 gives an example of calculating  $dn/dt$  via raw density data. the variation of  $n_e$  versus time is too fast to give information on slow time scale of interest. Therefore, in order to study the dynamic process of this density pump-out, we need to remove the higher frequencies. In this section, we use three methods to fit the density data during the first ECH cycle (from 2500ms to 3000ms). Among all three methods, polynomial fitting is shown to produce the best fits by providing minimum fitting errors.

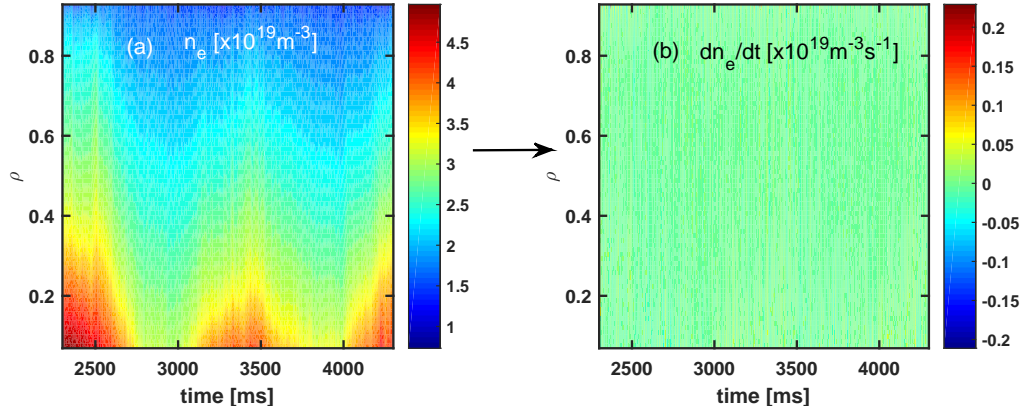


FIG. 5.3:  $dn/dt$  calculated by raw data. (a) 2D plot of raw electron data. (b) 2D plot of  $dn/dt$  calculated by raw data.

### 5.3.1 Exponential fitting

The first fitting method we try is an exponential fitting method since the trend of density pump-out from 2500ms to 3000ms behave as an exponential decay, see Figure 5.2.

We set  $n_{e,norm}$  from 0 to 1 by normalizing the electron density via:

$$n_{e,norm}(t, \rho) = \frac{n_e(t, \rho) - n_e(3000, \rho)}{n_e(2500, \rho) - n_e(3000, \rho)} \quad (5.1)$$

Here  $n_e(t, \rho)$  is the electron density at time  $t$  and location  $\rho$ . We assume  $n_e$  to be maximum at 2500ms and to be minimum at 3000ms. Next, we use an exponential fitting equation  $n_{e,norm} = \exp(-\frac{t-2.5s}{\tau_{fit}})$  to fit the data set of the normalized electron density from 2500ms to 3000ms.  $\tau_{fit}$  is the time interval in which the normalized density drops to  $1/e$  of its initial value. It can be interpreted as the characteristic decay time which indicates how fast the fitting line decays. In a tokamak plasma, the particle confinement time  $\tau_p$  is defined by the ratio of total number of confined particles over the particle lose at the edge  $\tau_p = \frac{\int_v n dv}{\int_s \Gamma ds}$  (where  $v$  and  $s$  are the volume and surface area within the torus chamber,  $\Gamma$  is particle flux). Thus with the same amount of core fueling, the smaller  $\tau_{fit}$  is, the larger transport is, and the smaller confinement time  $\tau_p$  would be during the exponential decay. Figure 5.4(a) shows both the raw reflectometer data and the exponential fitting line at  $\rho = 0.2$  while Figure 5.4(b) shows the same comparison at  $\rho = 0.7$ . The characteristic decay time are  $\tau_{fit} = 159ms$  at  $\rho = 0.2$  and  $\tau_{fit} = 119ms$  at  $\rho = 0.7$ , which indicates that the particle confinement time is smaller at the plasma edge than in the plasma core.

However, from Figure 5.4(a), we can see that the exponential fitting quality at  $\rho = 0.2$  is much worse than at  $\rho = 0.7$ . Particularly, during  $t = 2500 - 2650ms$  (i.e., in the beginning of the ECH cycle), the decrease of raw density data does not follow exponential decay, which introduces inaccuracy to the fitted density line. Also, the  $\tau_{fit,core} > \tau_{fit,edge}$  is not strictly valid since the initial decrease in the core maybe faster. Thus it is necessary to find another fitting method which can fit the density data in the first 100ms in the core.

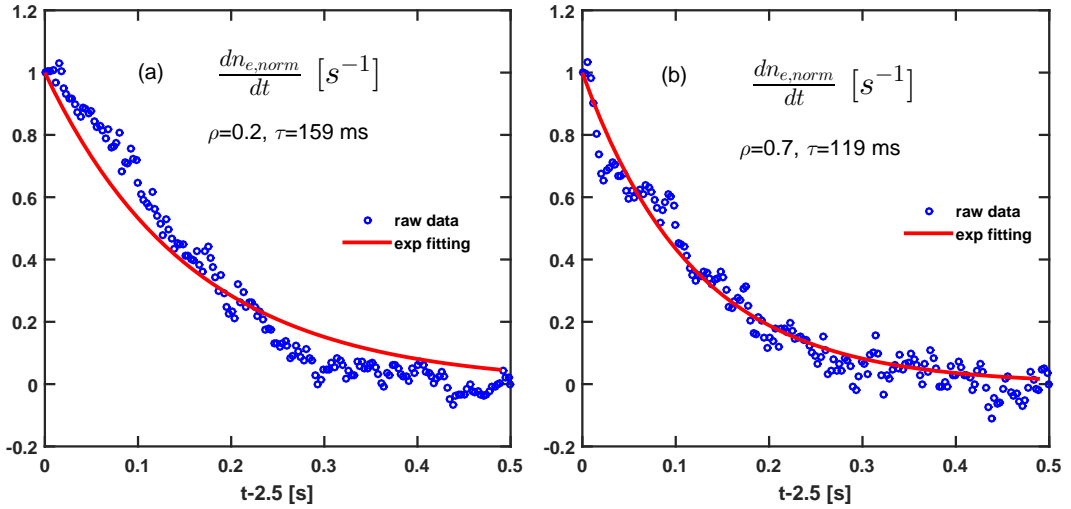


FIG. 5.4: Exponential fitting of normalized electron density from  $t = 2500ms - 3000ms$  at (a)  $\rho = 0.2$ , (b)  $\rho = 0.7$ .

### 5.3.2 Linear fitting

Linear fitting is used to fit the raw density data in the beginning of the first ECH cycle. When the time interval is small enough (smaller than 50ms in this case), the decrease of electron density can be treated as a linear function of the time in its first order approximation. Thus we can use a fitting equation  $n_{e,norm} = 1 + k(\rho)t$  to fit the data. Here  $k$  is the slope and 1 is the intercept since  $n_{e,norm}$  ranges from 0 to 1. Figure 5.5(a) shows the raw data and the linear fitting at  $\rho = 0.2$  and Figure 5.5(b) shows the same comparison at  $\rho = 0.7$ . The slope  $k(\rho)$  is an indication of how fast the electron density decreases. We can see that the slope at  $\rho = 0.2$  is  $-3.4$  while the slope at  $\rho = 0.7$  is  $-7$ , which again means the density decrease in plasma edge is faster than plasma core. This is in agreement with the exponential fitting result.

However, although a linear fitting technique can fit the density data well in the beginning of the ECH cycle, it cannot fit the whole cycle from 2500ms to 3000ms similar to the

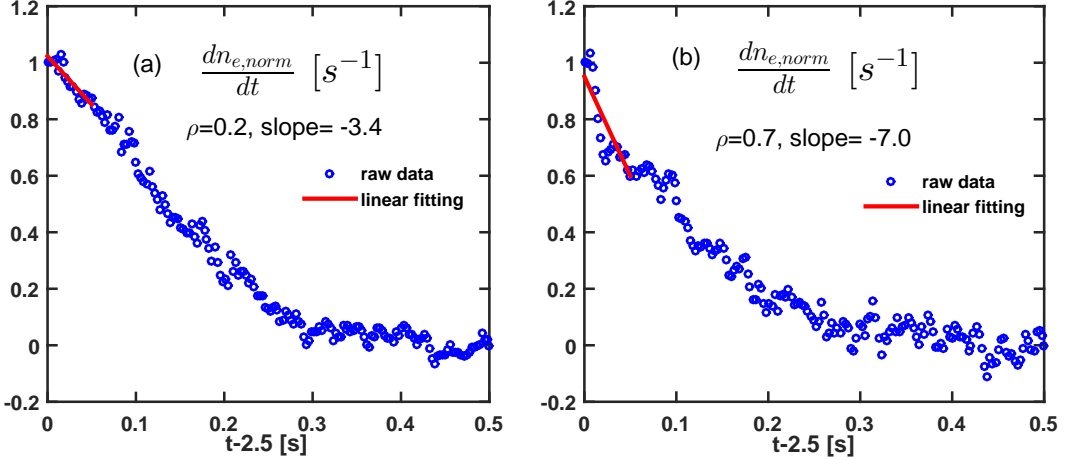


FIG. 5.5: Linear fitting of normalized electron density from  $t = 2500ms - 3000ms$  at (a)  $\rho = 0.2$ , (b)  $\rho = 0.7$ .

exponential fitting. When the time interval becomes larger, a first order approximation is no longer valid and higher orders effects become important. Thus we need to introduce a polynomial fitting method for a longer time interval.

### 5.3.3 Polynomial fitting

Lastly, we use a polynomial fitting method to fit the density data. The polynomial fits can capture the full time interval of interest (from  $2500ms$  to  $3000ms$ ) and provide a good fit in the core as well as the edge. The fitting equation looks like:  $n_{e,norm} = A_0 + A_1t + A_2t^2 + A_3t^3 + \dots$  where  $A_i$  are the fitting coefficients for different orders. We show in Figure 5.6(a) and (b) the 5th order polynomial fitting results at  $\rho = 0.2$  and at  $\rho = 0.7$ .

There are two reasons that we use the 5th order polynomial fitting. First, as shown in Figure 5.7(a), the 5th order's relative fitting error is 20% less than the 4th order in the core area (here the relative error refers to the ratio of density fitting error and local density, i.e.,

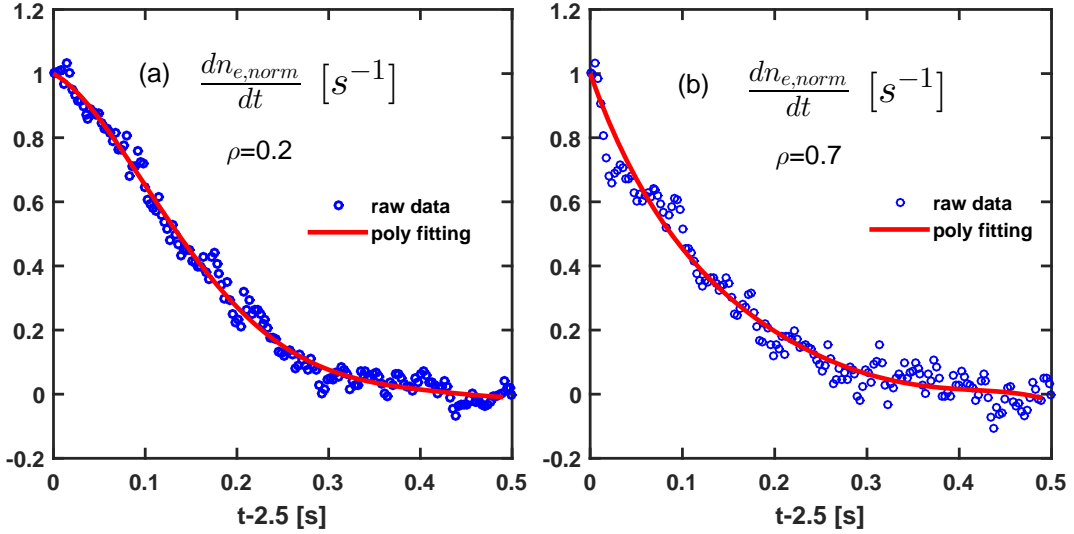


FIG. 5.6: Polynomial fitting of normalized electron density from  $t = 2500ms - 3000ms$  at (a)  $\rho = 0.2$ , (b)  $\rho = 0.7$ .

$\frac{\delta n}{n}$ ). Second, while the 6th order fitting reduces the error further, it introduces a higher frequency  $n_e$  modulation which defeats the purpose. Figure 5.7(b) gives an example of how data gets fitted from 2500-3000ms at  $\rho = 0.8$ , we see that, comparing with the 5th order, 6th order fitting captures more high frequency changes (small waves) in the fitting line. Thus it is better to keep in 5th order since we only want to see the slow evolution in density.

In the following part of this chapter and also in Chapter 6, we will use polynomial fitting to fit the density data because it gives more accurate fitting quality and less error when compared with exponential fitting or linear fitting. Figure 5.8 is a 2D plot of the polynomial fitted density data from  $2500ms$  to  $3000ms$ . It is much smoother when compared with the 2D plot of raw data (Figure 5.3(a)) however the slow evolution of the electron density is well captured. We can see the density decreases at all radial locations and this dynamic process takes at least  $300ms$  before the plasma reaches to new equilibrium.

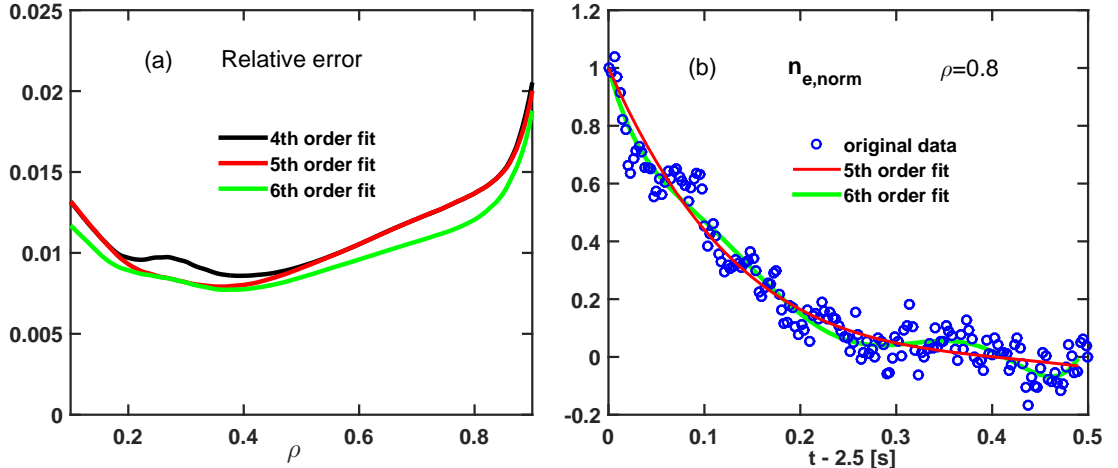


FIG. 5.7: Polynomial fitting quality (a) Relative fitting error of the 4th, 5th and 6th polynomial fittings. (b) Real data and the fitted lines between 5th order and 6th order polynomial fittings at  $\rho = 0.8$ .

rium (i.e. after 2800ms).

## 5.4 Changes in electron density gradient

### 5.4.1 2D plot of $R/L_n$

In the former section, we smoothed the electron density data from  $t = 2500 - 3000\text{ms}$  using a polynomial fit, see Figure 5.8. This smoothed data provides us with the ability to study how the density gradient changes when ECH is applied. We can calculate the inverse density scale length  $R/L_n = -\frac{R_0 \nabla n_e}{n_e}$  (where  $R_0$  is the major radius) at each radial location at  $t = 2500 - 3000\text{ms}$ . A 2D plot (Figure 5.9) illustrates the magnitude of  $R/L_n$  versus time and space. We can see from Figure 5.9, in plasma core at  $\rho \approx 0.1$ , inverse density scale length  $R/L_n$  keeps increasing after we turn the ECH on at  $t = 2500\text{ms}$ .  $R/L_n$  peaks around 2650ms in the core (red region in Figure 5.9) and decreases afterwards. Around

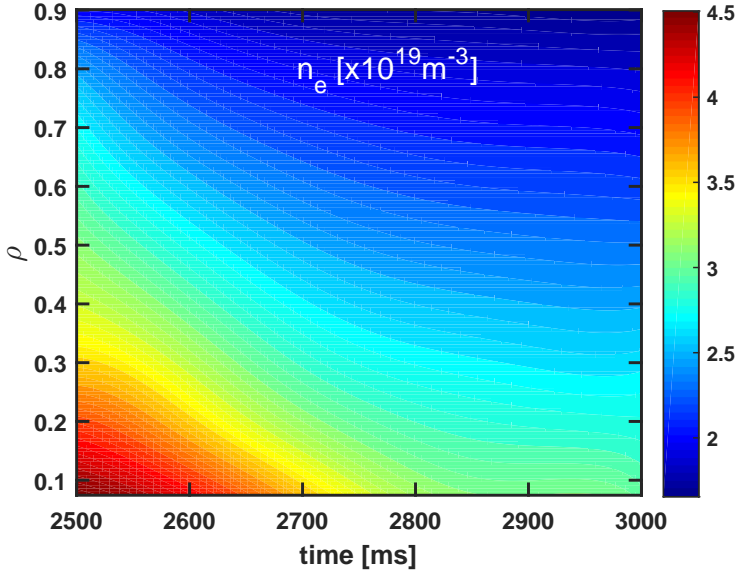


FIG. 5.8: Polynomial fitting of electron density. 2D plot of electron density from 2500ms - 3000ms

mid-radius region ( $\rho = 0.4 - 0.65$ ), the similar trend can be observed where  $R/L_n$  first increases until 2600ms and then decreases again. However, we cannot observe this peaking of inverse density scale length when it goes toward the plasma edge ( $\rho > 0.7$ ). We do not plot the value of density gradient outside  $\rho = 0.85$  since for H-mode plasmas, the  $R/L_n$  in pedestal region is much larger than the one inside the pedestal. In addition, we focuses mainly on the role of turbulence regime in this chapter. However, from Chapter 4, we can see that the role of  $E \times B$  dominates over the turbulence effects (i.e.,  $E \times B$  shear larger than the linear growth rate) outside  $\rho = 0.85$ .

#### 5.4.2 Dominant mode frequency

Next we calculate the frequency of the dominant instability mode using TGLF. TGLF is a quasi-linear gyrokinetic code to calculate the linear eigenvalues of the most unstable mode (more details about TGLF can be found in Section 3.1). We choose six time slices before and after the ECH pulse: one in steady state NBI phase ( $t - 35ms$ ), three in the

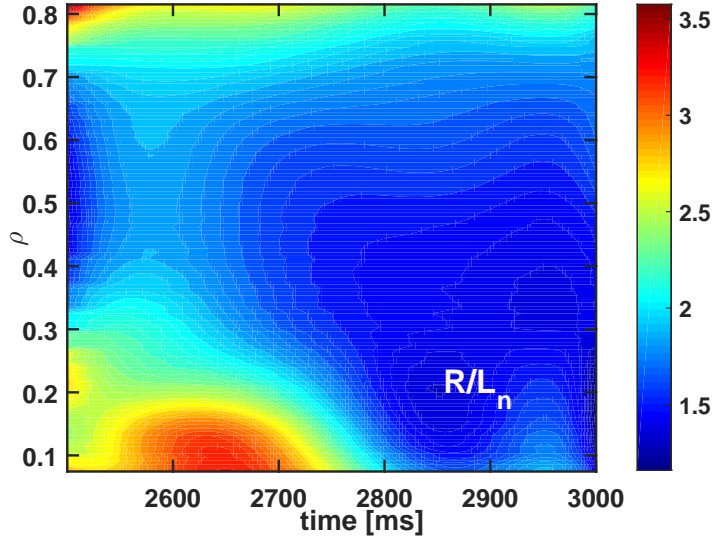


FIG. 5.9: 2D plot of  $R/L_n$  using the polynomial fitted electron density data during the ECH pulse (2500ms - 3000ms). x-axis is the time, y-axis is  $\rho$ .

dynamic changing phases after turning on ECH ( $t + 7ms$ ,  $t + 30ms$ ,  $t + 65ms$ ), and two in steady state ECH phase ( $t + 168ms$ ,  $t + 340ms$ ). Here  $t = 2500ms$  is the time we turn on the ECH pulse. TGLF uses fits of experimental plasma parameters. Fits were obtained in similar way as previous chapter. The calculated profiles of the frequency of the most unstable mode for  $0 < k_\theta \rho_s < 1$  are shown in Figure 5.10, where  $k_\theta$  is the poloidal wave-number,  $\rho_s$  is the ion sound radius. During the steady state phase with only NBI heating ( $t - 35ms$ , blue line), the frequency of the most unstable mode is negative in the plasma frame, which is in the ion diamagnetic direction. As a result we can identify this mode as an ITG mode, which is driven by the ion temperature gradient. After turning on ECH at  $t = 2500ms$ , we can see that the most unstable mode remains in the ITG regime at  $t + 7ms$ ,  $t + 30ms$ , and  $t + 65ms$ , while the absolute magnitude of frequency from  $\rho = 0.4 - 0.6$  decreases gradually. At  $t + 168ms$ , the mode frequency inside  $\rho < 0.65$  switches sign from negative to positive, indicating a switch to electron diamagnetic direction. As a result, the dominant mode now becomes a Trapped Electron Mode (TEM) which is driven by both the

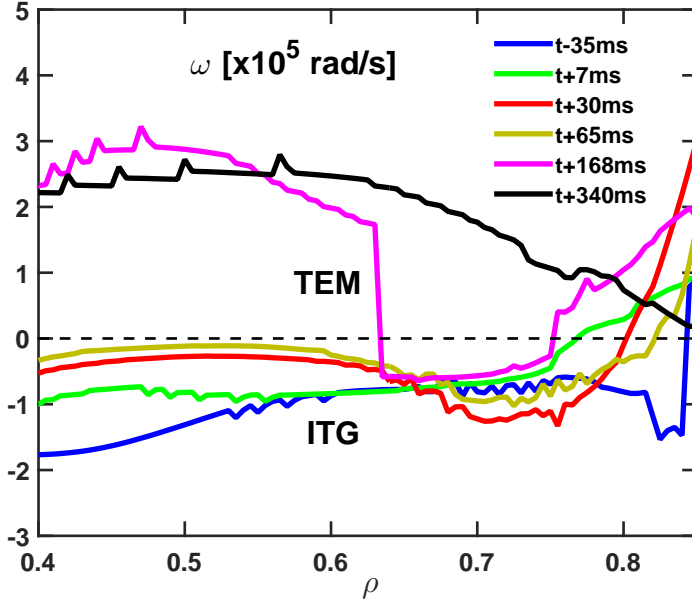


FIG. 5.10: Frequency of the most unstable mode within  $0 < k_\theta \rho_s < 1$  by TGLF at different time slices.

electron density gradient and the electron temperature gradient. However, for the region where  $\rho = 0.65 - 0.75$  at  $t + 168ms$ , the mode is still dominated by ITG, which indicates that the switch in mode starts in the plasma core and propagates outward. Lastly, as it goes further into steady state ECH phase at  $t + 340ms$ , the dominant mode becomes TEM in the whole plasma region (black line).

### 5.4.3 Inverse density scale length versus unstable mode frequency

We compare the inverse density scale length  $R/L_n$  and the frequency of the most unstable mode in this section. Figure 5.11 shows  $R/L_n$  as a function of the mode linear frequency at  $\rho = 0.4$  and  $\rho = 0.5$ . We can see that, when the absolute value of mode frequency decreases in the ITG regime (negative  $\omega$ ), local density peaking increases. Once the dominant unstable mode switches over to the trapped electron mode (TEM) regime, the local density gradient decreases again. A maximum in the density gradient has been

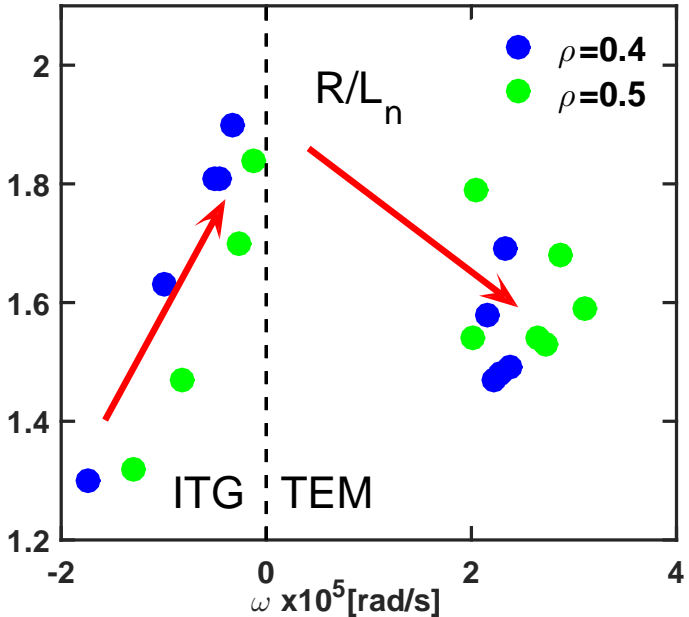


FIG. 5.11: Electron density gradient vs the mode frequency at  $\rho = 0.4$  (blue),  $\rho = 0.5$ (green).

reached when the mode has zero frequency, which corresponds to the cross-over from ITG to TEM. However, this non-monotonic correlation between  $R/L_n$  and mode frequency is only observed from plasma core to mid-radius. It no longer exists in outside  $\rho = 0.6$  region, see Figure 5.12. One explanation is that the microscopic turbulent transport is no longer dominant in this region. Effects from  $E \times B$  shear can overwhelm turbulence and thus suppress the turbulent transport (see previous chapter). Other particle transport mechanisms such as collisional transport or MHD instability can also become important as it goes toward the plasma edge.

In addition, this correlation between  $R/L_n$  and mode frequency is in agreement with the theoretical predictions [22, 68, 82] as well as the experimental results [23, 82] from AUG. In those theoretical studies on AUG and on off-diagonal turbulent particle transport [73, 32, 24], thermo-diffusion is used to explain this non-monotonic correlation. As

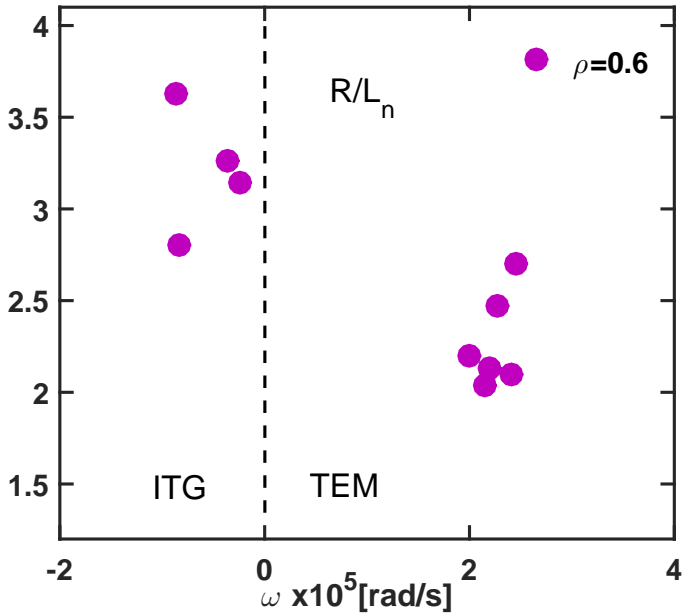


FIG. 5.12: Electron density gradient vs the mode frequency at  $\rho = 0.6$  (purple).

discussed in Section 2.3, thermo-diffusion can produce an inward pinch while in the ITG regime, in which case the thermo-diffusion coefficient  $D_T$  is negative. In Ref. [85, 22] simulations show the absolute value of  $D_T$  increases when the instability mode frequency approaches zero from the ITG side (negative  $\omega$  side), indicating an increase in the inward pinch. However after the turbulence changes to electron dominant regime,  $D_T$  switches quickly from negative to positive, indicating an outward flux. Although the change in thermo-diffusion coefficient matches the correlation between density gradient and mode frequency, we should be careful that in the original work of [85, 22], simulations are carried out assuming zero turbulent flux in quasi-linear gyrokinetic calculations and zero central fueling. While in our experiment on DIII-D there exists a constant central beam source as well as a non-neglectable turbulent flux. Therefore, further validation needs to include turbulent flux term as well as source fueling term in the simulations to provide a more convincing comparison.

## 5.5 Changes in electron particle flux

### 5.5.1 Time dependent electron flux

We use ONETWO, a one-and-a-half-dimensional code, to calculate time independent flux. As shown in Section 3.1, ONETWO calculates the ion flux by solving the transport equation:

$$\frac{\partial n_i}{\partial t} + \nabla \cdot \Gamma_i = S_i \quad (5.2)$$

here  $n_i$  and  $\Gamma_i$  are the density and the particle flux of ion species  $i$ ,  $S_i$  is the ion beam source. For time independent case, ONETWO assumes that the plasma is not evolving, i.e.,  $\frac{\partial n_i}{\partial t} = 0$ . Thus the radial ion flux can be integrated by  $\Gamma_i = \int S_i d\rho$ . Furthermore, ONETWO assumes that the electron flux  $\Gamma_e$  is the same as the ion flux based on quasi-neutral approximation of the plasma. From time evolution Figure 5.1(a)(b) we can see that the central neutral beam fueling is always the same no matter whether it is before or after the ECH pulse at  $t = 2500ms$ . Therefore, it is reasonable that ONETWO gives similar time independent electron flux for each time slice, see Figure 5.13(a). However,

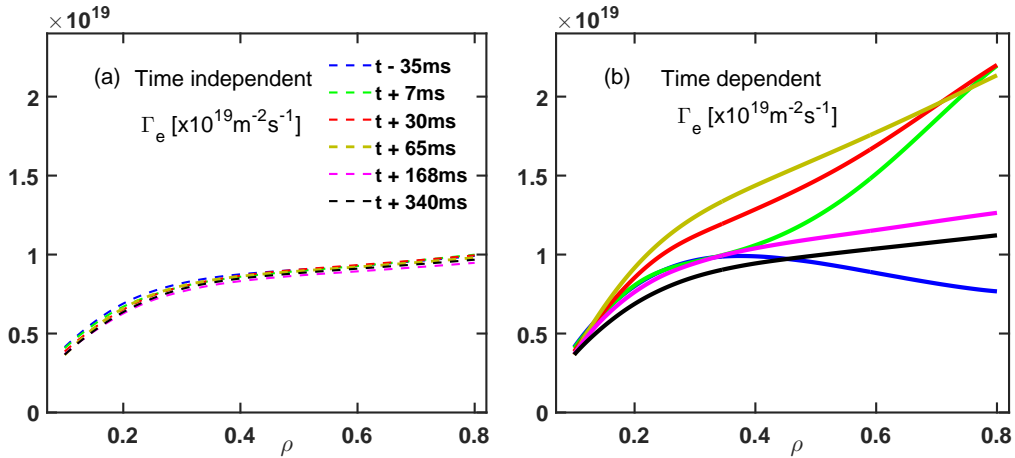


FIG. 5.13: Electron flux at different time slices. (a) Time independent flux with only source term included. (b) Time dependent flux with both  $dn/dt$  and source term included.

time independent calculation only holds when the plasma is in a steady state or when the source is much larger than  $dn/dt$ . In our case, the plasma after applying ECH undergoes a dynamic process where the magnitude of  $dn/dt$  is comparable to core particle source. Thus a time dependent term  $\int -\frac{dn}{dt} d\rho$  need to be added in order to fully describe the flux change. We can calculate  $\frac{dn_e(t,\rho)}{dt}$  at each time and radial location using the polynomial fits to the density from Figure 5.8 (more details regarding  $dn/dt$  changes will be presented in the next chapter). Then the time dependent electron flux is calculated by  $\Gamma_e = \int (-\frac{dn_e}{dt} + S_i) d\rho$ , see Figure 5.13(b). We observe that, immediately after turning on the ECH at  $2500ms$  (see the green line in Figure 5.13(b)), the outward electron flux increases largely from outside mid-radius area ( $\rho > 0.4$ ). Then an increase in plasma core ( $\rho = 0.2 - 0.4$ ) follows after about  $30ms$  later (red and yellow lines). In the final stage, the electron flux decreases back to the same level as it was before the ECH pulse after  $300ms$  (purple and black lines), indicating that plasma has reached a new equilibrium (i.e.,  $dn/dt = 0$ ). In addition, we make a 2D plot to describe how the time dependent component of electron flux changes, see Figure 5.14. As time evolves, we see the value of  $\int -\frac{dn_e}{dt} d\rho$  increases first and then decreases around  $2600ms$  at  $\rho = 0.3 - 0.7$ . The "ridge" (which is defined as the line connecting the maximum curvature point of each contour curve, see black line in Figure 5.14) of this contour plot lays around  $t = 2600ms$ , which coincides with the switch point of ITG to TEM as discussed in Section 5.4.2. Caution needs to be applied here that we only plot  $\int -\frac{dn_e}{dt} d\rho$  (instead of  $\Gamma_e$ ) in Figure 5.14. This is because we do not have precise profile of the electron source. More details of the electron source will be discussed in the Discussion Section.

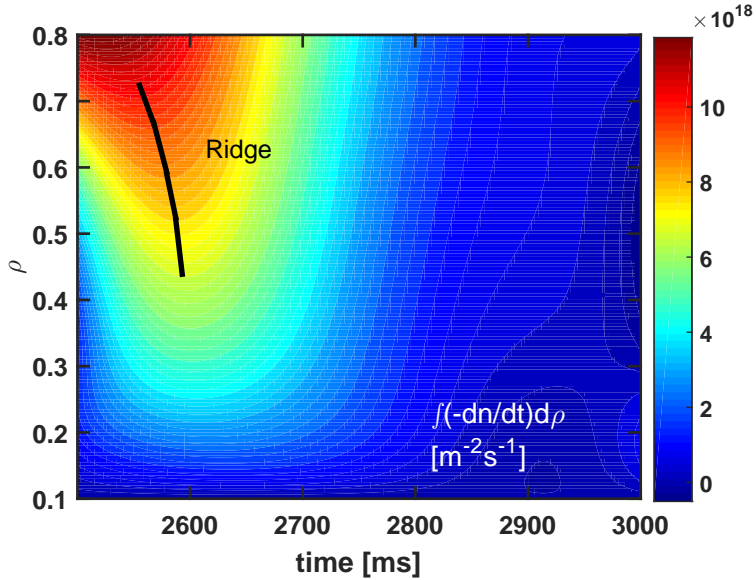


FIG. 5.14: 2D plot of the time dependent electron flux which includes both  $dn/dt$  and the source term during the first ECH pulse (2500ms - 3000ms). x-axis is the time, y-axis is  $\rho$ .

### 5.5.2 $\Gamma_e$ versus unstable mode frequency

Similar to what we did in Section 5.4, we plot the time dependent component of electron flux  $\int -\frac{dn_e}{dt} d\rho$  as a function of dominant mode frequency at  $\rho = 0.4$  and  $\rho = 0.5$ , see Figure 5.15. A similar non-monotonic correlation is obtained as in Figure 5.11, where the magnitude of  $\int -\frac{dn_e}{dt} d\rho$  peaks at ITG-TEM cross-over location and decreases toward both deep inside each instability regime. This similarity between Figure 5.11 and Figure 5.15 is a very interesting finding because we get these two figures from two independent calculation approaches, i.e.,  $R/L_n$  from density changing in spatial direction and  $\Gamma_e$  from density changing in time direction. Since particle flux can be closely related to density gradient through a diffusion coefficient, an important conclusion from this similarity is that, the diffusion coefficient is close to a constant or is only slightly linear correlated with the mode frequency (i.e., the ITG-TEM change). Figure 5.16 shows how effective diffusion coefficient,  $D_{eff} = -\Gamma_e / (\partial n_e / \partial r)$  depends on the mode frequency. Please note, that this is an effective diffusion coefficient and thus does encompasses the particle pinch as well as

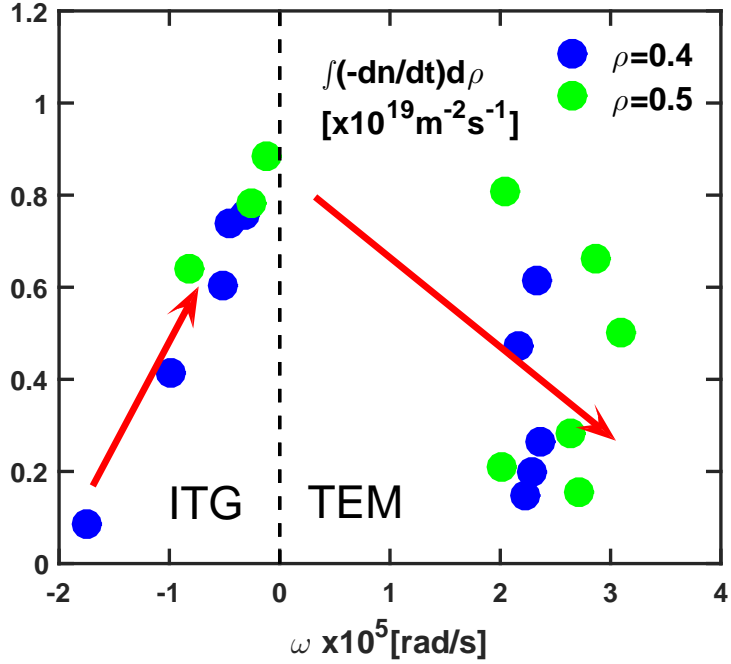


FIG. 5.15: Electron particle flux vs the mode frequency at  $\rho = 0.4$  (blue),  $\rho = 0.5$  (green).

the actual diffusion coefficient. We can see that the non-monotonic correlation no longer exists.  $D_{eff}$  increases slightly when crosses from ITG regime to TEM regime.

## 5.6 Discussion

In this chapter, we seek to find how changes of turbulence characteristics can affect density peaking. We observe for the first time in DIII-D a correlation between the changes in  $R/L_n$  and the changes in dominant mode frequency. The density peaking is maximized at the cross-over between the ITG and the TEM regime and decreases rapidly toward both deep ITG and deep TEM sides. This correlation is in agreement with theoretical predictions [22, 68, 82] and experimental results [23, 82] on AUG. While one difference from the results of AUG is that, instead of using a database of steady state L-mode and H-mode discharges, we find this correlation through an unsteady state process, using a

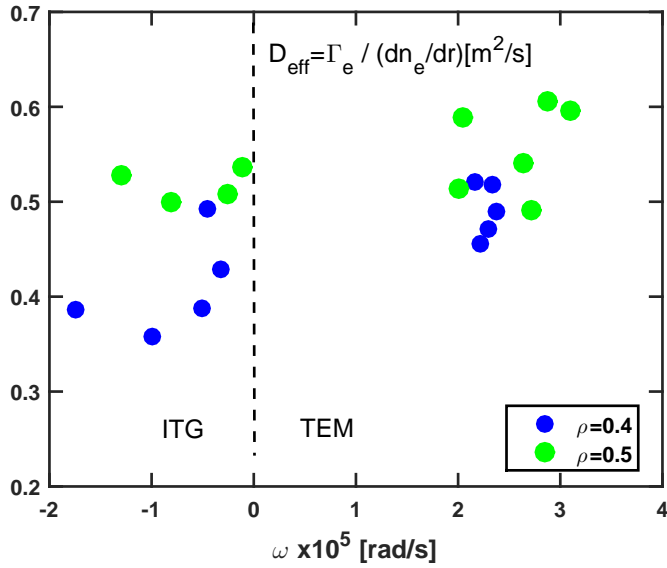


FIG. 5.16: Effective diffusion coefficient vs the mode frequency at  $\rho = 0.4$  (blue),  $\rho = 0.5$  (green).

dynamic analysis within only one low-collisionality H-mode discharge. In our case, core neutral beam fueling is kept the same, which makes it possible for us to calculate and thus compare the changes in electron particle flux. In addition, the correlation between  $R/L_n$  and mode frequency is critical to both theoretical prediction and experimental control of the density profile in future burning plasma devices such as ITER. Currently, the predictive capability of particle transport is not well validated, and as such ITER assumes that the core density will be flat [135]. However, in this chapter we show that the peaking of the core density is strongly influenced by the frequency of the turbulent mode. This opens up a new opportunity to control density peaking in plasma core through controlling the turbulence regime, which has the potential to compensate for some loss of confinement at the plasma edge.

In Section 5.5, we also find a similar non-monotonic correlation between the time dependent component of electron particle flux  $\int -\frac{dn_e}{dt} d\rho$  and the dominant mode frequency,

see Figure 5.15. However, we cannot make the conclusion that  $\int -\frac{dn_e}{dt} d\rho$  is proportional to the electron flux  $\Gamma_e$  until we can prove  $S_i = S_e$ . Although the profile of ion source  $S_i$  can be obtained from simulation models such as NFREYA [96] and NUBEAM [97] in ONETWO, the calculation of electron particle source from these models is still not yet validated. Current simulations from NFREYA show a difference in profiles between electron source and ion source, which indicates that the electron flux should be different from the ion flux. Since we already captured  $\frac{dn_e}{dt}$  from fitted electron density data, in order to obtain a fully accurate time dependent electron flux, more work is still needed to investigate how the actual electron source profile looks like. In addition, we find that the effective diffusion coefficient  $D_{eff} = -\Gamma_e / (\partial n_e / \partial r)$  is close to a constant during ITG/TEM transition (Figure 5.16). However  $D_{eff}$  encompasses the particle pinch  $v$  as well as the actual diffusion coefficient  $D$ . Thus further research will be placed on separating these two coefficients and on understanding how D's and v's change as a function of the frequency of the unstable mode.

Lastly, although thermo-diffusion can be used to explain the correlation between  $R/L_n$  and mode frequency, it does not apply to explain the electron density pump-out phenomenon after turning on the ECH. This is because the pump-out process happens in a much shorter time scale ( $\tau_{fit} < 150ms$  as shown in Section 5.3.1), during which the mode frequency is always negative and the plasma is always in ion dominant region, see Figure 5.10. In the next chapter we will study the dynamic process of the density pump-out and compare it with the growth rate of the most unstable mode. This study will reveal the turbulence drive nature of the ECH pump-out.

## 5.7 Conclusion

In this chapter, we present for the first time on DIII-D an observation of a correlation between electron density gradient and instability mode frequency. A dedicated low density H-mode experiment is conducted on DIII-D where the ECH power is modulated with a period of 500 ms on top of steady neutral beam heating. By fitting the density evolution during the ECH pulse, we find that the local density gradient has a non-monotonic correlation with the linear gyro-kinetic calculated mode frequency. In the ion temperature gradient (ITG) regime, local density peaking increases as the absolute frequency of the dominant unstable mode decreases. Once the dominant mode switches over to the trapped electron mode (TEM) regime, the local peaking of the density decreases again, producing a maximum value of density gradient in the ITG/TEM cross-over. We also find that the time dependent particle flux (which is independent of the local gradients) shows a similar correlation. This indicates that the effective diffusion coefficient is close to a constant during ITG/TEM switch.

# CHAPTER 6

## Understanding the ECH pump-out process on DIII-D

### 6.1 Introduction

In Chapter 5, we have discussed the correlation between electron density peaking and frequency of instability mode. Aside from this correlation, we also observe a strong decrease in electron density when electron cyclotron heating (ECH) is applied. This phenomenon is often referred to as density “pump-out” in the literature [61, 71, 72, 32, 24, 73]. In future large burning tokamak devices like ITER [156], ECH will be installed as one of the three radio frequency (RF) heating systems [157] to deliver sufficient central heating power and maintain an active current control (the other two are lower hybrid (LH) heating system, and ion cyclotron (IC) resonant heating system). Thus it is important for us to understand the physics of this ECH induced density pump-out since a density flattening reduces plasma performance and thus fusion gain.

During the past decade, observations of electron density pump-out caused by ECH have been reported in many tokamaks [71, 72, 24, 73, 74, 32]. For example, in one recent paper by S. Mordijk et al. [69], experiments are designed to investigate the impact of replacing a fraction of neutral beam injection (NBI) power with ECH in low collisionality H-mode plasmas on DIII-D. The line average electron density decreases from  $3.5 \times 10^{19} m^{-3}$  in NBI discharge to  $2.0 \times 10^{19} m^{-3}$  in ECH discharge, while both plasmas are in steady states. Since the decrease in fueling of ECH discharge is much smaller than the decrease in  $n_e$  (see Figure 1 in Ref [69]), we can say that the overall outward particle transport has increased under the ECH. However, most of the previous research focuses on steady state plasmas which does not address how the plasma reaches the new steady state regime. Therefore, questions like when and where the density pump-out happens, or what drives the density pump-out, have not been addressed. In order to solve these questions and to understand the physics behind the ECH pump-out, a time-dependent analysis needs to be conducted to study the dynamic pump-out process. Today, thanks to the progress in high resolution diagnostic techniques, we are able to perform a time-dependent analysis of the electron density in low collisionality DIII-D H-mode plasmas. This analysis helps to reveal the drive behind the ECH pump-out.

In this chapter, we use the same plasma discharge as in Chapter 5, where a modulated ECH pulse is added into NBI heated H-mode plasma. The same polynomial fitting is also carried out to smooth the electron density data and the electron temperature data. We observe an electron density pump-out when applying 3MW ECH power at  $t = 2500ms$ . Using the fitted data, the electron density changing rate over time  $dn/dt$  can be calculated. We find that, although the localized central electron heating leads to a maximum increase of the electron temperature in plasma core, the fastest decrease of the electron density occurs outside mid-radius ( $\rho \approx 0.7$ ). Both the quasi-linear gyrokinetic calculations and the

measured density fluctuations show that, this reduction in electron density corresponds to an increase in ITG turbulence drive at  $\rho = 0.7 - 0.8$ . The turbulence changes on a slower time scale from an ion dominant mode to an electron dominant mode. Finally, after we reduce the ECH power to  $1MW$  at  $t = 3000ms$ , an electron density pump-in is observed. However, the density pump-in does not happen at the same radial location as the pump-out. Thomson Scattering measurement shows that the pump-in starts from top of the pedestal and then transfers inward to the core area.

The structure of this chapter is as follows. First, in Section 6.2, we will present the changes in different plasma parameters during the first ECH pulse, along with a comparison between the measured electron density data from the Thomson Scattering system and the Reflectometer system. In Section 6.3, a dynamic observation of the ECH caused electron density pump-out will be reported. We choose several time slices during this process to show in detail how changes in turbulence drive the density pump-out. We also show a comparison between the experimentally measured density fluctuations and the linear stability calculations. In the following section, Section 6.4, will discuss the electron density pump-in process when the ECH power is reduced to  $1MW$  at  $t = 3000ms$ . A discussion (Section 6.5) and a summary (Section 6.6) will be provided at the end.

## 6.2 Experimental measurement

In this chapter, we use the same low-collisionality H-mode discharge on DIII-D as in Chapter 5, where the ECH power is modulated with a periodicity of  $500ms$  on top of steady neutral beam heating (see Figure 5.1 in Chapter 5 for the time evolution of different plasma parameters). The electron density is measured by both the Thomson Scattering system [114] and the Reflectometer system [120]. The electron temperature

comes from both the electron cyclotron emission (ECE) system [123] and the Thomson Scattering system. The ion temperature and the impurity toroidal rotation are measured by the charge exchange recombination (CER) system [140]. Readers can refer to Chapter 5 for more details about the experimental set up and refer to Chapter 2 for the diagnostics.

In order to compare the changes in different plasma parameters, we choose one time slices before the ECH pulse and three time slices after the ECH pulse. They are: one during the steady state NBI phase ( $t - 35ms$ ), two in the dynamic changing phases after turning on the ECH ( $t + 30ms, t + 65ms$ ), and one during the ECH after new equilibrium is achieved ( $t + 340ms$ ). Here  $t = 2500ms$  is the time we add  $3.2MW$  ECH power into plasma core ( $\rho \approx 0.2$ ). Figure 6.1(a) shows the electron density profiles measured by the Thomson Scattering system. We observe that, although the electron density profile

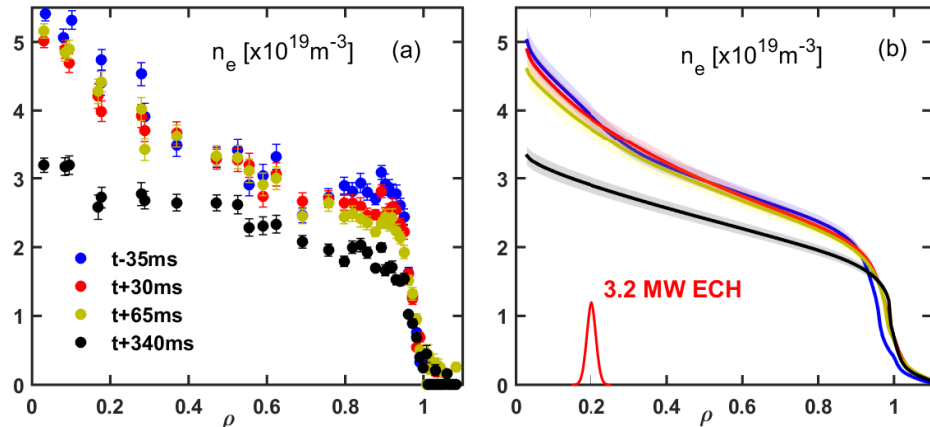


FIG. 6.1: Density profiles. (a) Thomson scattering data shows the electron density pump-out when adding ECH at 2500ms. (b) Reflectometer profiles data also indicate the similar decrease.

originally decreases at the plasma edge after applying the ECH, it eventually decreases at all radial locations during the new equilibrium. A similar pump-out is also seen by reflectometer data, see Figure 6.1(b). However, it is difficult to distinguish just from Thomson Scattering profiles where the strongest pump-out happens. Thanks to high

temporal and spacial resolution of the Reflectometer system, an calculation of  $dn/dt$  is possible. We will show the results of  $dn/dt$  in the next section. In addition, the electron temperature increases (see Figure 6.2(a)) and the central electron heating which is slightly off-axis causes a peak of  $T_e$  profile at  $\rho = 0.2$  after 2500ms. The ion temperature profile and the impurity toroidal rotation profile in Figure 6.2(b)(c) decrease after the turn on of the ECH. We can also see by comparing Figure 6.1 and Figure 6.2, that the increase in electron temperature  $T_e$  is much faster than the decrease in  $n_e$ ,  $T_i$ , and  $v_\phi$ . In other words, the characteristic time of the  $T_e$  change is much smaller than the other three.

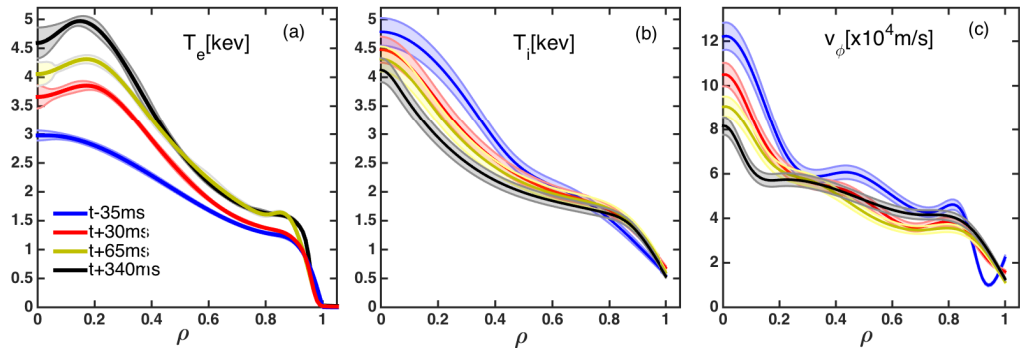


FIG. 6.2: Temperature and rotation profiles. (a) Electron temperature profiles. (b) Ion temperature profiles. (c) Toroidal rotation velocity profiles.

Before ending this section, one more comparison is presented here between the electron density measured by the Thomson Scattering system and the Reflectometer system. Since the precision of the electron density measurement would largely affect the results of our time-dependent analysis, we need to verify the accuracy of density measurements. Figure 6.3 shows the time evolution data from both the Thomson scattering system (red dots) and the Reflectometer system (blue lines) in the plasma core ( $\rho = 0.29$ ), at mid-radius ( $\rho = 0.52$ ), and at the plasma edge ( $\rho = 0.76$ ). To reduce the noise in the Thomson Scattering data, we calculate its combined average value (grey lines) based on the nearest five points.

Therefore, by comparing blue and grey lines, we can observe that the measurements from both systems shows good consistency through  $t = 2500 - 3000\text{ms}$  (first ECH pulse) in the plasma core, and through  $t = 2600 - 3000\text{ms}$  at the plasma edge and at mid-radius. However, after the ECH power is reduced to  $1\text{MW}$ , an obvious discrepancy can be observed at all radial locations. One explanation for this discrepancy is that the reflectometer profile

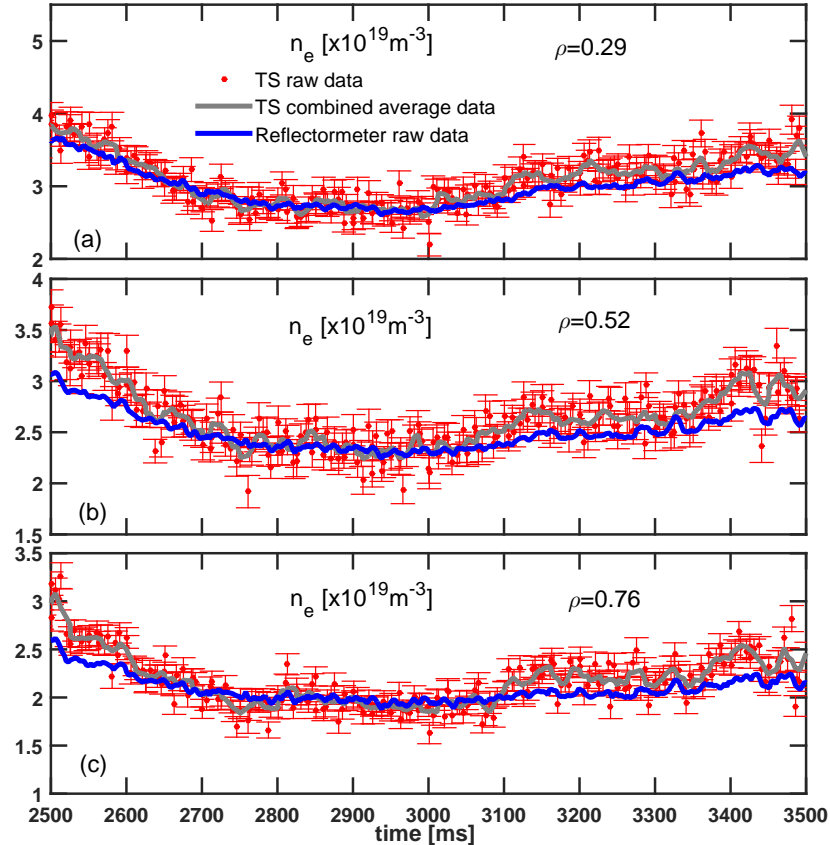


FIG. 6.3: Thomson scattering data *vs* reflectometer data of electron density at (a) plasma core, (b) mid-radius, and (c) plasma edge. The Thomson data is always higher than the reflectometer data during the time window of  $3000\text{ms}-3500\text{ms}$ .

can become inaccurate and have errors when the density profiles become hollow or flat. As we have discussed in Section 3.2.2, the reflectometer system measures the electron density profile by detecting the phase delay of the reflected microwaves from their corresponding plasma cutoff layers [120], thus it can only “see” monotonic increasing electron density

profile due to its reflecting nature. As will be discussed in Section 6.4, the density becomes hollow or flat in our ECH reducing process at  $t = 3000 - 3500\text{ms}$  (see Figure 6.9), where the density pump-in starts from top of the pedestal and thus the density profile arises firstly from the edge. To conclude, we can use the high resolution electron density data provided by the Reflectometer system during the density pump-out phase ( $t = 2500 - 3000\text{ms}$ ) but we should choose the Thomson Scattering measurement to study the pump-in.

## 6.3 Density pump-out

In this section, we will present a detailed analysis of what causes the density to pump-out. Our results show that the strongest change in the local electron density correlates with a substantial increase in the linear growth rate of the dominant mode. Moreover, the experimentally measured density fluctuations also indicate an increase in turbulence.

### 6.3.1 2D plot of $dn/dt$ and $dT_e/dt$

Using the same polynomial fitted electron density data from Section 5.3 in Chapter 5, we first calculate the normalized electron density changing rate over time:

$$\frac{dn_{e,norm}}{dt} = \frac{1}{n_e} \frac{dn_e}{dt} \quad [\text{s}^{-1}]$$

Similar to the 2D figures in chapter 5, we present a contour plot of  $dn/dt$  in Figure 6.4(a), with the x-axis in time direction and the y-axis in spatial direction. Here the time window is chosen from  $2500\text{ms}$  to  $3000\text{ms}$  and the radial location expands from  $\rho \approx 0.1 - 0.9$ . In addition, the same polynomial fitting method can be applied to the electron temperature data measured by high resolution ECE system. Figure 6.4(b) shows how the normalized electron temperature changes  $\frac{dT_{e,norm}}{dt} = \frac{1}{T_e} \frac{dT_e}{dt}$  from  $t = 2500 - 2580\text{ms}$  from  $\rho = 0.08 - 0.7$

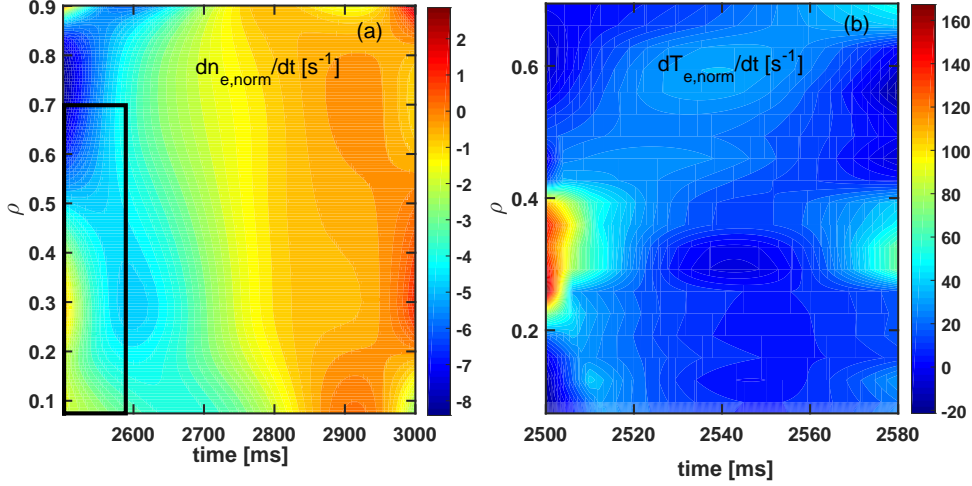


FIG. 6.4: Density and temperature change. (a) 2D plot of electron density changing rate as a function of time during first ECH pulse (2500ms - 3000ms) (b) 2D plot of electron temperature changing rate as a function of time during ECH pulses (2500ms - 3000ms)

(the black box area in Figure 6.4(a) where the outer limit is set by ECE coverage). By comparing the figures of  $\frac{dn_{e,norm}}{dt}$  and  $\frac{dT_{e,norm}}{dt}$ , two interesting observations can be made. First, we can see that the increase of electron temperature occurs on a much shorter time scale when compared to the density pump-out process, indicating a larger diffusive transport in electron energy transport channel than electron particle transport channel. Second, since the ECH power is centrally deposited around  $\rho = 0.2$ , the increase of electron temperature also occurs first in the plasma core. However, for the electron density, the maximum reduction happens outside mid-radius around  $\rho = 0.6 - 0.8$  as highlighted by dark blue in Figure 6.4(a). This density reduction then spreads inward to the plasma core after about 100ms. These features of the electron density pump-out tell us that there is a local change in particle transport to which is triggered by ECH pulse at the plasma edge and that this change is not coupled directly to the change in  $\nabla T_e$  in the core.

### 6.3.2 Change in turbulence drive

Global changes in plasma density, temperature, and rotation profiles alter the local gradients and thus affect the linear stability and turbulence drive. We know from Section 2.2 that the Ion Temperature Gradient (ITG) mode is driven by ion temperature gradient, while the Trapped Electron Mode (TEM) is driven by both the electron density gradient and the electron temperature gradient [158]. Thus we can plot the quotient of  $\frac{R/L_{T_e}}{R/L_{T_i}}$ ,  $\eta_e = \frac{R/L_{T_e}}{R/L_{n_e}}$ , and  $\eta_i = \frac{R/L_{T_i}}{R/L_{n_i}}$  as an indication of the competition between TEM drive and ITG drive, see Figure 6.5. Figure 6.5(a) shows that  $\frac{R/L_{T_e}}{R/L_{T_i}}$  increases by a factor of 2 from

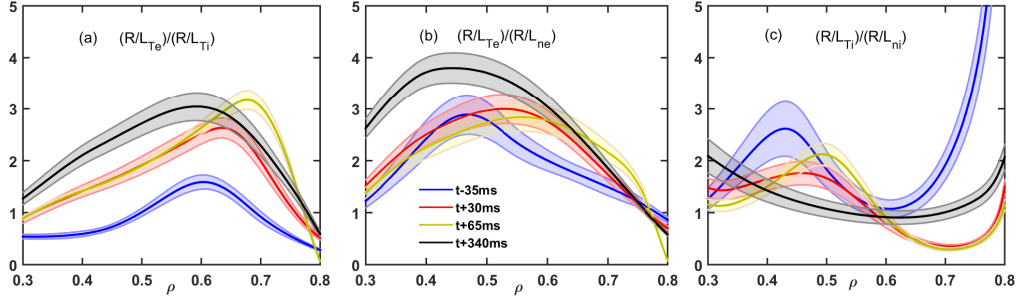


FIG. 6.5: Changes in gradient drive. (a)  $(R/L_{T_e})/(R/L_{T_i})$  profiles at different time slices from  $\rho = 0.3 - 0.8$  (b)  $\eta_e = (R/L_{T_e})/(R/L_{n_e})$  profiles. (c)  $\eta_i = (R/L_{T_i})/(R/L_{n_i})$  profiles.

$t - 35ms$  to  $t + 340ms$ . This increase indicates that the TEM drive gradually overtakes the ITG drive during the ECH pulse. This leads to a change in the instability from ion dominant mode to electron dominant mode. Figure 6.5(b) shows how  $\eta_e = \frac{R/L_{T_e}}{R/L_{n_e}}$  changes after applying the ECH. At  $\rho = 0.4 - 0.5$ ,  $\eta_e$  peaks and the value increases from  $t - 35ms$  to  $t + 340ms$ . However, outside mid-radius where  $\rho = 0.7$ , the magnitude of  $\eta_e$  is small and does not change within experimental errorbar. Thus the potential for a TEM driven instability is larger in plasma core than at the plasma edge and the drive increases as a result of ECH pulse. Finally, in Figure 6.5(c), profile of  $\eta_i = \frac{R/L_{T_i}}{R/L_{n_i}}$  shows little change in plasma core, while it shows a 50% decrease between steady states (blue and black lines)

and dynamic states (red and yellow lines) in plasma edge. These figures illustrate that the turbulence drive in these plasmas is strongly affected by the addition of an ECH pulse.

### 6.3.3 Change in dominant unstable mode

In order to see how turbulence affects the density pump-out as well as to see how instability type changes, we use TGLF (see Section 3.1.2) to calculate the linear growth rate and frequency of the most unstable mode for each of the selected time frames. The experimental profiles from Figure 6.1 and 6.2 are used as input to TGLF. In addition to the previous four time frames, we add two more time frames ( $t+7\text{ms}$ ,  $t+168\text{ms}$ ) to show how the eigenvalues evolve. Figure 6.6(a) shows the growth rate profiles of the most unstable mode from  $0 < k_\theta \rho_s < 1$  for the selected time slices. We can observe that, after turning

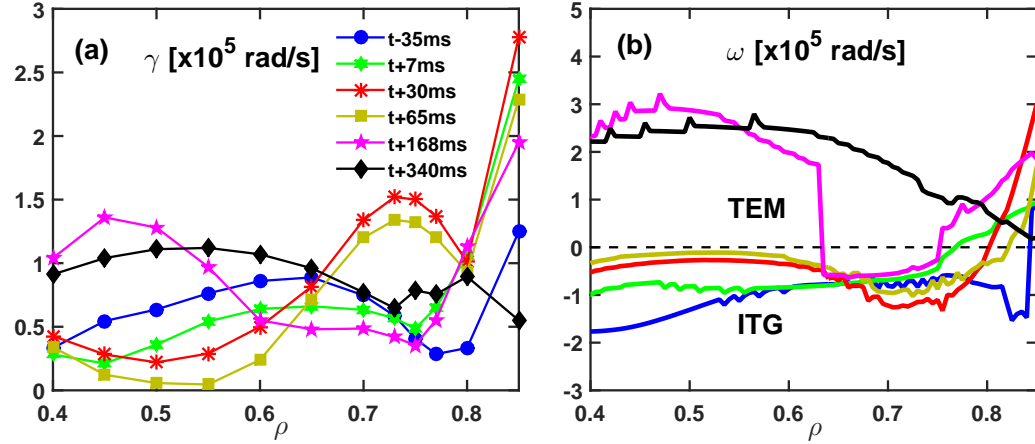


FIG. 6.6: Growth rate and frequency profiles. (a) Growth rate of the most unstable mode for  $0 < k_\theta \rho_s < 1$  by TGLF at different time slices. (b) Frequency of the most unstable mode for  $0 < k_\theta \rho_s < 1$  by TGLF at different time slices.

on the ECH, the linear growth rate of the most unstable mode increases strongly from  $\rho = 0.6 - 0.8$  (red and yellow lines). This increase coincides with the same region where the maximum density pump-out is observed (see in Figure 6.4(a)). Figure 6.7 shows the time evolution of the  $dn/dt$ , the growth rate  $\gamma$  and the frequency  $\omega$  of the most unstable

mode at  $\rho = 0.5$  (red lines) and  $\rho = 0.73$  (blue lines). We can see the decrease in the

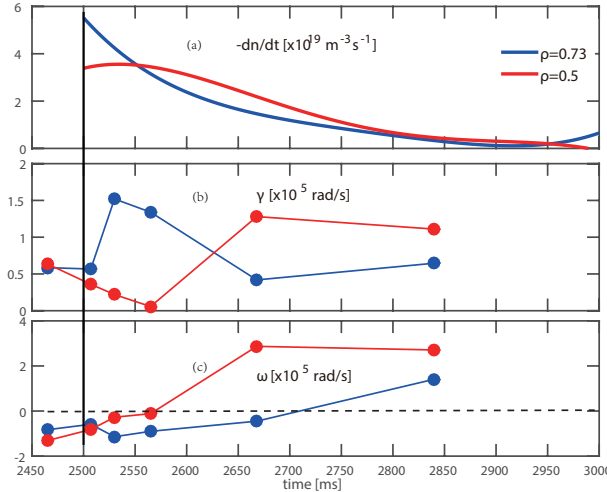


FIG. 6.7: Time evolution of  $dn/dt$ ,  $\gamma$  and  $\omega$  during the pump-out induced by ECH heating.

electron density correlates with a strong increase in the linear growth rate at  $\rho = 0.73$ , while at  $\rho = 0.5$  the turbulence drive first decreases. Therefore, the initial density pump-out induced by ECH heating at the plasma edge is a result of an increase in turbulence drive, not a change in frequency. The turbulence only drifts from the ITG regime to the TEM regime (represented by positive mode frequency) on a much longer time scale, namely, after 160ms at the plasma edge, at which time the growth rate at  $\rho = 0.6 - 0.8$  has decreased again to the same level as before the ECH. We can see that the change from ITG to TEM occurs first in the core and takes even longer to reach the edge. Therefore, it is excluded that the initial of the pump-out is resulted from a change of the ITG to the TEM regime and thus a sign change of the thermo-diffusion pinch [61, 82] (the reversal of the thermo-diffusion pinch can only add to the pump-out at a later time, see Chapter 5).

### 6.3.4 Density fluctuations

To further investigate the changes in turbulence, we compare the density fluctuations measured by the Beam Emission Spectroscopy (BES) and the Doppler BackScattering (DBS). The BES measures density fluctuations at ion-scale (typically  $k_\theta \rho_s < 0.3$ ), while

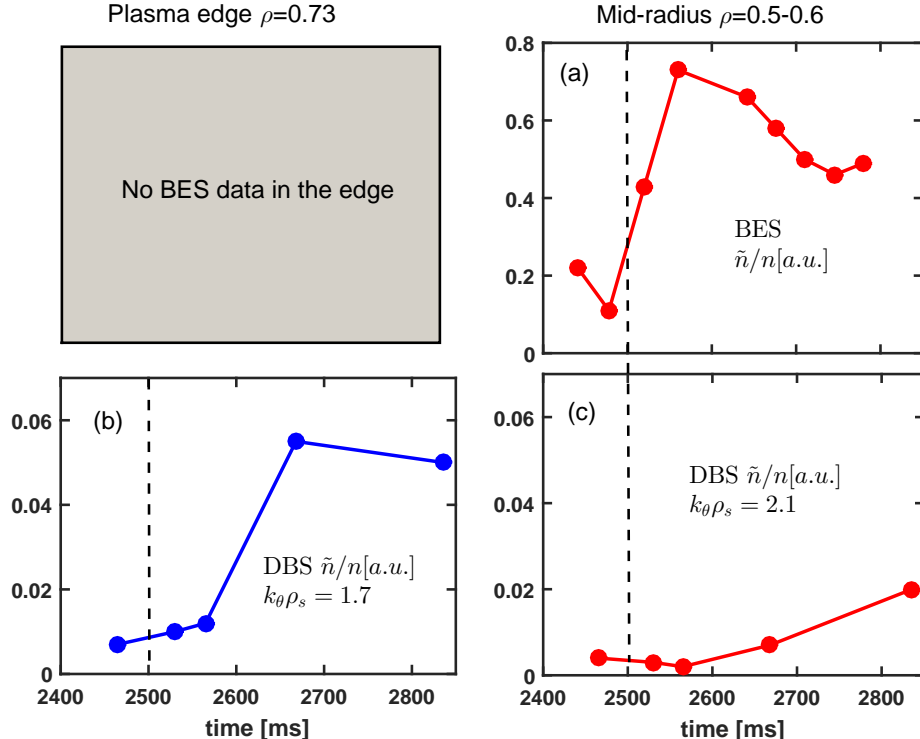


FIG. 6.8: Time evolution of density fluctuation measurement. (a) Density fluctuations measured by BES at  $\rho = 0.55$ . (b) Density fluctuations measured by DBS at  $\rho = 0.73$ . (c) Density fluctuations measured by DBS at  $\rho = 0.6$ .

the DBS measures at intermediate scale ( $k_\theta \rho_s = 1.6 - 2.1$ ) which is typically associated with the TEM unstable regime. More details of these two diagnostics can be found in Section 2.2. Figure 6.8 presents the experimentally measured density fluctuations. We can see that, immediately after the ECH is turned on, there is an increase in density fluctuations at the ion-scale, measured by the BES at  $\rho = 0.55$ , see Figure 6.8(a). However, in Figure 6.8(c) there is nearly no increase in intermediate density fluctuations at  $\rho = 0.6$ . On the other hand, at  $\rho = 0.73$ , we find that the intermediate density fluctuations increase largely after

$170ms$ , which corresponds to the time when the turbulence switches from ITG to TEM regime (see Figure 6.8(b)). In this case, we can validate that the turbulence only changes from ITG to TEM in a much larger time scale than the density pump-out. However, there is no BES data available in plasma edge. We will still need ion-scale density fluctuation measurement around  $\rho = 0.7$  to confirm previous TGLF simulation results, which predicts a large increase of ITG driven turbulence in plasma edge.

## 6.4 Density pump-in

In this section, to verify the features of density pump-out and the instability change during the ECH pulse, we will look at its inverse case – electron density pump-in when the ECH is reduced by 66% of the power during  $2500 - 3000ms$ . We carry out time-dependent analysis for the density pump-in phase after  $3000ms$ , which confirms the correlation between changes in turbulence at plasma edge and particle confinement.

### 6.4.1 Changes in Profiles

As shown in the time evolution figure (Figure 5.1), at  $3000ms$ , we lower the ECH power to  $1MW$  and maintain it for another  $500ms$  so that the plasmas can reach a new steady state. The power of the neutral beam injection is kept at  $3MW$ , which ensures the same level of central beam fueling. Figure 6.9(a)(b) shows the raw data of electron density profiles from the Thomson Scattering system and the Reflectometer system. Here  $t$  represents the time when ECH power is lowered ( $t = 3000ms$ ). The new selected time slices here are: steady state  $3.2MW$  ECH case ( $t - 44ms$ ), two slices during  $1MW$  ECH ( $t + 50ms, t + 188ms$ ) when profiles are still evolving, and a steady state  $1MW$  ECH case ( $t + 402ms$ ). We can see from Figure 5.1 that, there is an increase in electron density profile which takes about  $300ms$  to reach another steady state. But the density pump-in does not

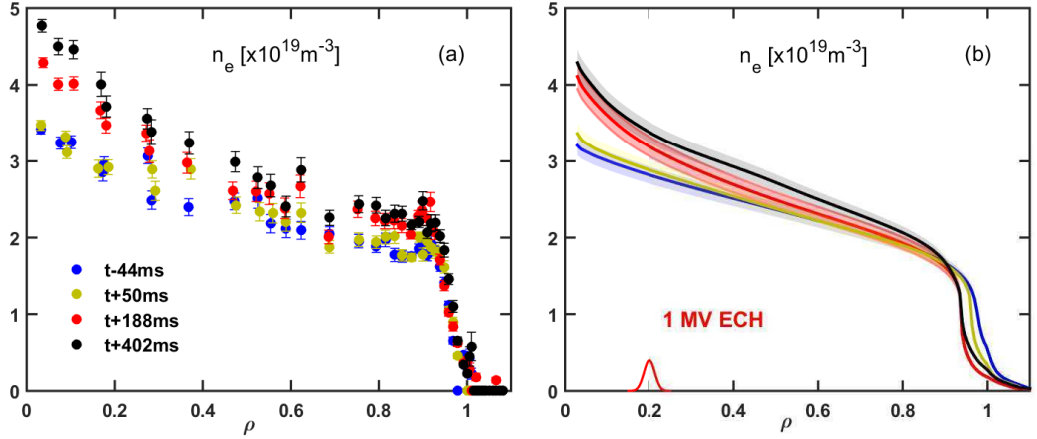


FIG. 6.9: Density profiles in pump-in process. (a) Thomson scattering data shows the electron density increase when reducing the ECH power to 1MW at  $t=3000\text{ms}$ . (b) Reflectometer profiles data also indicate the similar density pump-in.

show a maximum increase at  $\rho = 0.6 - 0.8$  area like in the pump-out case. The pump-in process seems to start from top of the pedestal based on the Thomson Scattering data, see Figure 6.9(a). As discussed in Section 6.2, we can only rely on the Thomson Scattering profiles in density pump-in case due to the measurement inaccuracies in the Reflectometer profiles. However, the Thomson Scattering data doesn't have a high temporal resolution (especially in plasma edge), we will not use polynomial fitting (which gives a large fitting error) to smooth its data and thus no 2D plot is available for  $dn/dt$  in the pump-in case.

As shown in Figure 6.10, the electron temperature decreases on a much shorter time scale than the other plasma parameters. Both the ion temperature and the impurity toroidal rotation increase during this process (Figure 6.10(b)(c)). However, it is still not clear what causes the decrease of ion temperature in the pump-out case ( $t = 2500 - 3000\text{ms}$ ) and the increase in the pump-in case ( $t = 3000 - 3500\text{ms}$ ) since the injected neutral beam power remains the same. One qualitative answer is that the increased total heating power drives more energy transport, which causes the decrease of  $T_i$ .

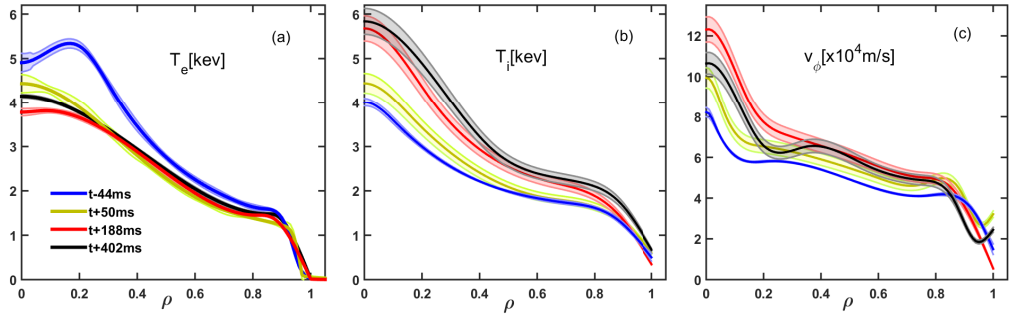


FIG. 6.10: Temperature and rotation profiles in pump-in. (a) Electron temperature profiles decrease fast after we lower the ECH power. While (b) ion temperature profiles and (c) toroidal rotation velocity profiles have an increase.

### 6.4.2 Change in dominant mode

Finally, as we did in the pump-out section, we calculate the most unstable linear mode eigenvalues. The only exception is that here we use electron density profiles from the Thomson Scattering system instead of from Reflectometer system as input to TGLF. Figure 6.11 shows the growth rate as well as the mode frequency profiles of all four selected time slices. Unlike the density pump-out case, the growth rate in pump-in process does not

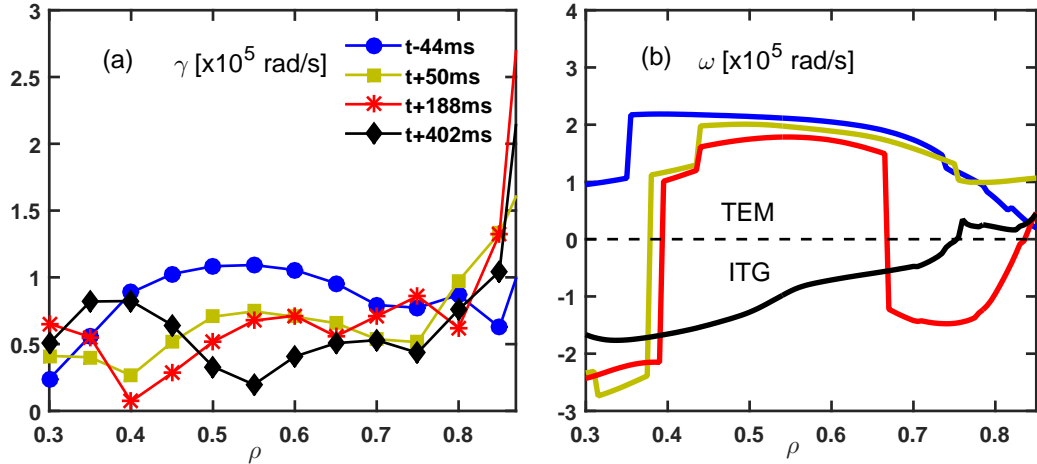


FIG. 6.11: Growth rate and frequency profiles in pump-in. (a) Growth rate of the most unstable mode for  $0 < k_\theta \rho_s < 1$  by TGLF at different time slices. (b) Frequency of the most unstable mode for  $0 < k_\theta \rho_s < 1$  by TGLF at different time slices.

show a sudden change around  $\rho = 0.75$ . Instead, after reducing the ECH at  $t = 3000ms$ , the growth rate decreases from  $\rho = 0.4 - 0.7$  and increases outside  $\rho > 0.8$ . From Figure 6.11(b) we can tell that the turbulence changes gradually from TEM regime (positive  $\omega$  value) back to ITG regime (negative  $\omega$  value). This change in turbulence type again first happens in plasma core and takes more than  $300ms$  to switch fully into ITG regime (black line in Figure 6.11(b)), which is longer than the density pump-in time scale.

## 6.5 Discussion

In this chapter, we study the role of turbulence during the electron density pump-out process when ECH is applied. Where previous research on ASDEX [24], DIII-D [69], and C-Mod [32] has studied the density response to central electron heating during steady state conditions, we investigate for the first time the time evolution of electron density during the ECH pump-out process using high resolution Reflectometer data. We show that the ECH pump-out corresponds to an increase in the unstable mode growth rate in the ITG regime outside mid-radius (see Figure 6.7). The measured density fluctuations from both the BES and the DBS also highlight that the density pump-out is the result of an increase in ITG turbulence. This new result complements the previous non-time dependent analysis, where the pump-out was attributed to a change in turbulence type and the reversal of the thermo-diffusive pinch [82].

In Section 6.3, we have already obtained the changes in dominant mode maximum growth rate and frequency among  $0 < k_\theta \rho_s < 1$ . However, a more comprehensive and more persuasive way is to look at the mode spectrum instead of just the maximum value. In Figure 6.12, a detailed linear gyrokinetic simulation which shows the spectrum of mode growth rate and frequency at each radial location is presented. Where the x-axis repre-

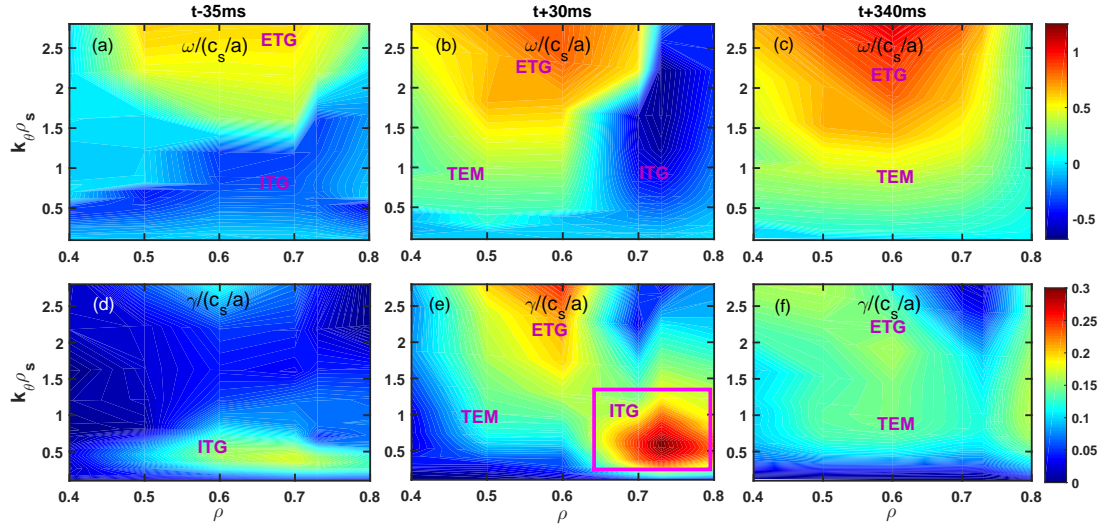


FIG. 6.12: Growth rate and frequency spectrum. 2D plot of the growth rate as a function of  $\rho$  and  $k_\theta \rho_s$  at (a)t-35ms, (b)t+30ms, (c)t+340ms. 2D plot of the frequency as a function of  $\rho$  and  $k_\theta \rho_s$  at (d)t-35ms, (e)t+30ms, (f)t+340ms.

sents the radial locations and the y-axis is the normalized wave number  $k_\theta \rho_s$  which extends from  $0 < k_\theta \rho_s < 2.8$ . We can see that after turning on the ECH, a large increase of the linear growth rate at  $\rho = 0.73$  is observed within  $0 < k_\theta \rho_s < 1$  (Figure 6.12(e)) while the frequency of the unstable mode remains in ITG regime for all  $k_\theta \rho_s$  between  $0.7 < \rho < 0.8$  (purple box in Figure 6.12(b)). Therefore, the effect of changing the thermo-diffusive pinch can be ruled out in the initial of pump-out since the instability mode remains the same. Moreover, comparing Figure 6.12(a)(b)(c), we find that the change from ion drift direction to electron drift direction first starts in the core at large wave number area, then it “spreads” into the plasma edge and drives low wave number turbulence into electron diamagnetic direction as time evolves. The maximum value of the growth rate in steady state ECH case also moves from  $0 < k_\theta \rho_s < 1$  regime in NBI case to  $k_\theta \rho_s \approx 1.5$  regime in TEM case (see Figure 6.12(d)(f)), indicating a shift in turbulence size from ion-scale to intermediate scale.

The correlation between the increased growth rate and the maximum pump-out rate at  $\rho = 0.73$  can be related to the results discussed in Chapter 4 (also see in Ref. [21, 143]). During the experiment reported in Chapter 4, the  $E \times B$  shearing rate is altered by varying the toroidal rotation while all other plasma parameters such as  $T_e$ ,  $T_i$ , and instability type are kept the same. The particle confinement is observed to be strongly reduced in balanced torque injected discharge, where the  $E \times B$  shearing rate is smaller than the low wave number turbulence growth rate from mid-radius to top of the pedestal. On the contrary, the confinement improves when the  $E \times B$  shearing rate at  $\rho = 0.7 - 0.9$  is larger than or equal to the mode growth rate. Similar effects of the  $E \times B$  shear were also found previously during the application of Resonant Magnetic Perturbations (RMPs) [143] and in the QH-mode [151]. Therefore, both the results in this chapter and the one in Chapter 4 indicate that the turbulence drive at outside mid-radius region plays a dominant role in determining the particle confinement and thus the density profiles.

As for other plasma parameters, since the radial expansion of ECE system depends on the optical thickness of plasma and in our case it can only provide electron temperature data of  $\rho < 0.67$ , we are not able to get high temporal resolution  $T_e$  data in the plasma edge. However, the Thomson Scattering system can provide electron temperature data in plasma edge. Finally, the CER diagnostic has more limited spacial resolution and thus prevents us from plotting 2D figures of the ion temperature and the impurity toroidal rotation.

## 6.6 Conclusion

In this chapter we present the first time-dependent analysis of the electron density during the ECH pump-out process. We add centrally deposited ECH pulses into neutral

beam heated H-mode plasmas. A polynomial fitting method is carried out on both the electron density data and the electron temperature data. While the initial increase of the electron temperature occurs in the plasma core, we find that the strongest density reduction occurs outside mid-radius. At the same time, both the linear gyrokinetic calculation and the experimentally measured density fluctuations show that the dominant mode growth rate has a large increase at the same outside mid-radius region ( $\rho = 0.73$ ). However, the turbulence only changes from the ITG regime to the TEM regime in a much longer time scale than the density pump-out. Finally, we show that a density pump-in which starts from top of the pedestal is triggered when the ECH is reduced to 30% of the pulse power. The instability changes fully back from TEM to ITG after about 300ms.

# CHAPTER 7

## Conclusion and Outlook

This chapter summarizes the main results of this thesis. We also outline some possible directions for future research on turbulent particle transport.

### 7.1 Conclusions

The work described in this thesis contributes to both the experimental observations and the theoretical predictions in turbulent particle transport. Our experiments on DIII-D focus on low density, low collisionality H-mode plasmas in the ITER Similar Shape (ISS) [156, 135]. We investigate how different plasma parameters such as toroidal rotation or instability types can affect turbulent particle transport and thus the density profile. Below we outline the main results of the thesis sorted by chapter.

In **Chapter 2**, we show that classical and neoclassical theories predict particle transport which is at least two orders of magnitude smaller than the experimental results. Thus microscopic turbulent particle transport plays an important role in determining density profile. Next, some general concepts of turbulence as well as an intuitive picture of how

shear flow stabilizes turbulence is introduced. Through gyro-kinetic derivation, we show that the ion temperature gradient (ITG) mode is driven by  $\nabla T_i$  while the trapped electron mode (TEM) is driven by both  $\nabla n_e$  and  $\nabla T_e$ . A literature review summarizing current work on particle transport is also presented in this chapter.

In **Chapter 3**, we introduce two simulation codes, namely, ONETWO and TGLF. ONETWO calculates energy, particle, and momentum transport by solving transport balance equations. TGLF solves the linear gyrokinetic equations and thus calculates the linear growth rates and frequencies of unstable modes in plasma. We also briefly introduce the principles of 6 essential diagnostics that are used in our experiments. These diagnostics provide measurements of various plasma parameters such as the electron density, the electron temperature, the ion temperature, the toroidal rotation, and the density fluctuations. The spatial and the temporal resolution of these diagnostics on DIII-D are discussed at the end of each corresponding subsection.

**Chapter 4** discusses how changes in toroidal rotation affect particle transport and confinement. We vary the toroidal rotation by changing the injected torque while keeping the same underlying turbulence drive. A correlation between the normalized density inverse scale length  $R/L_n$  and the  $E \times B$  shearing rate is observed. We find that the electron density profile decreases from outside mid-radius to top of the pedestal when the  $E \times B$  shear is smaller than the linear growth rate of the most unstable mode at small  $k_\theta \rho_s$ . However, when the  $E \times B$  shear is larger than or at least similar to the linear growth rate, the density profile is increased. In addition, the perturbed transport coefficients  $D_p$  and  $v_p$  indicate that changes in transport are not only just related to an increase in outward diffusion, but also related to the changes in inward pinch. We find a substantial increase in the perturbed inward pinch at the plasma edge for the counter-torque injected discharge.

An increase in intermediate scale density fluctuation is also observed at the same radius, which is similar to previous work in Ref [69]. Finally, we show that quasi-linear gyrokinetic simulations of the particle flux do not match experimental observations, which suggests that more work is still needed to improve the quasi-linear gyrokinetic simulations for low rotation and ECH dominantly heated plasmas.

**Chapter 5** discusses how changes in turbulence regime can determine the local density gradient. For the first time on DIII-D, a correlation between the inverse density scale length  $R/L_n$  and the frequency of the most unstable mode is observed. We find that, when the turbulence is driven by the ion temperature gradient (ITG), the local density gradient increases as the absolute frequency of the dominant unstable mode decreases. Once the dominant unstable mode switches over to the trapped electron mode (TEM) regime, the local density gradient decreases again, i.e., the density gradient reaches a maximum when the mode has zero frequency, which corresponds to the crossover from ITG to TEM. This correlation suggests that local density peaking can be controlled through turbulence regime in future large burning plasma devices such as ITER. Furthermore, we find that the time dependent component of electron particle flux  $\int -\frac{dn_e}{dt} d\rho$  shows a similar correlation with the frequency of the unstable mode. This indicates that the effective diffusion coefficient  $D_{eff} = -\Gamma_e / (\partial n_e / \partial r)$  is close to a constant during ITG/TEM switch if we assume the same electron particle source.

In **Chapter 6**, the phenomenon of electron density pump-out caused by ECH heating is studied. We present the first time-dependent analysis on electron density during the central electron heating. We show that, while the electron temperature increases initially from the plasma core, the strongest density reduction occurs outside mid-radius. Linear gyrokinetic analysis using TGLF shows that the onset of the density pump-out is not the

result of a change in turbulence regime, but the result of an increase in turbulence drive, in the ITG regime. Experimental measurement of the density fluctuations from both the Doppler BackScattering (DBS) system and the Beam Emission Spectroscopy (BES) system also support the increase in turbulence drive nature of the ECH pump-out. Finally, we reverse-test all the pump-out results by showing that a density pump-in which starts from top of the pedestal is triggered when the ECH is reduced to 30% of the pulse power.

## 7.2 Future work

This thesis has investigated how some of the plasma parameters such as toroidal rotation or turbulence regime can affect the turbulent particle transport. However, there are still many challenges ahead. In order to get to full predictive capability for particle transport, we will need to perform investigations with more complex simulation models and more precise measurements. Here we present some ideas and directions in our future work.

**Non-linear gyrokinetic simulations** The work presented in this thesis only includes linear or quasi-linear gyrokinetic calculations. As discussed in Chapter 4, the linear or quasi-linear gyrokinetic simulations show a disagreement with experimental observations for the particle flux as well as density fluctuations. One explanation could be that non-linear effects play an important role and that full non-linear gyrokinetic simulations would result in a better agreement. However, it is currently still unclear whether a fully non-linear multi-scale gyrokinetic simulations will result in an increase of the particle flux. Also, full non-linear calculations are too slow (in the aspect of CPU intense) for predictions. Since ongoing recalibration in TGLF has included a saturation model based on benchmarking with non-linear code GYRO [159], our future work will focus in two

aspects. If full scale modelling fixes the disagreement between simulation and experimental observation, an update on the saturation model for TGLF should be implemented. If non-linear calculation doesn't give the right result either, we should consider adding some missing physics such as neoclassical simulations.

**Perturbed transport coefficients** We use a perturbative technique in Chapter 4 to extract the separate contributions of diffusion coefficient  $D_p$  and inward pinch  $v_p$ . However, we need to be careful when interpreting the results from this technique. It is because the perturbed transport coefficients do not include the steady state and perturbed fueling sources. And these coefficients are calculated under circular plasma shape. Also, local electron temperature gradient and ion temperature gradient can be affected by gas puffs, which may cause the perturbed coefficients becoming larger. Currently it is still unclear whether the perturbed coefficients can accurately reflect the physics of steady-state transport. Therefore, improvements on analysis for  $D$  and  $v$  are needed on DIII-D in the future. It can include but not limit to, implementing non-circular geometry into perturbative analysis, controlling  $T_e$  and  $T_i$  during the gas puff, and including a non-linear optimization to extract the steady state transport coefficients as well as the perturbed transport coefficients [148].

**Impurity transport** The original work of this thesis only deals with changes in electron particle transport and electron density profile, it does not study the changes in impurity transport. However, impurity transport is an important topic in particle transport. Impurity ion accumulation in the core of tokamak plasmas can cause a deleterious combination of fuel dilution (mainly by light impurities) and radiation (mainly by heavy impurities) [160, 161], which strongly limits the stable operation as well as the good performance of a fusion power plant. Therefore, a more completed validation of the theoretical

paradigm will require the consideration of both electron and impurities transport. While electron transport is mainly produced by turbulent processes, the calculation of impurities transport is more complicated in that it has to include both turbulent and neoclassical components. There has already been some work of impurities transport on ASDEX [68, 161, 160] which show that impurities are well predicted by neoclassical theory. However, since we need quasi-neutrality in plasmas, we still want to see what changes could impurities bring to electron density and how does the impurity transport affect electron transport.

**Momentum transport** Besides the particle transport, a change of instability from the ITG regime to the TEM regime can also affect the momentum transport. For example, it is been found that the turbulence change can be one of the reasons to cause the reversal of intrinsic rotation (a phenomenon which plasmas can self-rotate toroidally without any external input of momentum) in a tokamak plasma [158, 162, 67, 163, 164]. Although there is no such reversal being observed in our low collisionality H-mode plasma experiments in Chapter 5 and Chapter 6, we can still see a decrease in the toroidal rotation when applying ECH at  $t = 2500ms$ . Thus further work of how turbulence regime affects momentum transport can also be performed using our modulated ECH discharge. In addition, the coupling between momentum and particle transport will be studied. By extracting similar momentum transport coefficients using perturbed technique, we can investigate on questions such as how density increase triggers the reversal of intrinsic rotation [162, 164], and whether the pinch of these two transport channels are the same.

**q-profile peaking** We report a correlation between the normalized density inverse scale length  $R/L_n$  and the frequency of the most unstable mode in chapter 5. Another component in determining the density profile is q-profile ( $q$  is the safety factor), through

the curvature pinch. Density peaking is observed to increase when the value of  $1/q$  increases on JET [66, 77, 78]. A similar correlation between the density peaking and q-profile is also observed on DIII-D, where the correlation is more pronounced when  $T_e = T_i$ , and less pronounced when  $T_e > T_i$  and the plasma is in a TEM turbulence regime. Thus we provide two possible methods (i.e., frequency of turbulent mode and q-profile) to help controlling core density peaking for future burning plasma devices like ITER.

**ITER** To sum up, many future works are still required to get a good predictive capability for ITER. We need a better recalibration in TGLF with ITER like conditions. Experimental scaling as well as simulations need to be validated on multiple devices. The coupling of multi-transport channels needs to be studied. And a detailed study concerning the roles of fueling versus pinch on density peaking should be performed, since both of them can affect core density peaking but have their own limitations (core neutral beam fueling is not desirable on ITER while pinch term is largely depend on different plasma conditions). With ITER aimed at achieving net energy gain from magnetic confinement device, no piece of the transport puzzle is too small to solve. We hope the contributions from this dissertation, although far from a solution to the confinement problem, can serve as an important step in building future improved particle transport predictions.

# APPENDIX A

## Frequently used physical symbols

This appendix lists all physical symbols used in this dissertation as well as their units (except for the dimensionless parameters) following behind.

TABLE A.1: Physical symbols and their units

Symbol	Unit	Quantity
$R_0$	[m]	tokamak major radius
$a$	[m]	tokamak minor radius
$\epsilon$		inverse aspect ratio
$\epsilon_0$	[Farad/m]	vacuum permittivity
$n$	[ $\times 10^{19} m^{-3}$ ]	plasma density
$n_e$	[ $\times 10^{19} m^{-3}$ ]	electron density
$n_{e,norm}$	[ $\times 10^{19} m^{-3}$ ]	normalized electron density
$n_i$	[ $\times 10^{19} m^{-3}$ ]	ion density

$n_0$	$[\times 10^{19} m^{-3}]$	equilibrium plasma density
$\tilde{n}$	$[\times 10^{19} m^{-3}]$	density fluctuation
$\tilde{n}_e$	$[\times 10^{19} m^{-3}]$	perturbed electron density
$\tilde{n}_i$	$[\times 10^{19} m^{-3}]$	perturbed ion density
$\mathbf{k}$	$[m^{-1}]$	wave number
$\mathbf{k}_{\parallel}$	$[m^{-1}]$	parallel wave number
$k_{\theta}$	$[m^{-1}]$	poloidal wave number
$k_B$	$[J/K]$	Boltzmann constant
$\omega$	$[rad/s]$	oscillation frequency
$\omega_{freq}$	$[rad/s]$	instability mode frequency
$\omega_{E \times B}$	$[rad/s]$	$E \times B$ shearing rate
$\omega_{gyro}$	$[rad/s]$	electron gyro-frequency
$\gamma$	$[s^{-1}]$	instability mode growth rate
$\gamma_0$		one photon
$\Gamma_e$	$[m^{-2}s^{-1}]$	electron particle flux
$\Gamma_i$	$[m^{-2}s^{-1}]$	ion particle flux
$\Gamma_n$	$[m^{-2}s^{-1}]$	particle flux
$\Gamma_Q$	$[mJ/s]$	energy flux
$\Gamma_M$	$[kgm^2/s^2]$	momentum flux
$\Psi$	$[T \cdot m^2]$	poloidal magnetic flux
$\tilde{\phi}$	$[V]$	perturbed electric potential
$F(\mathbf{x}, \mathbf{v}, t)$	$[m^{-3}]$	density distribution function
$F_0$	$[m^{-3}]$	equilibrium part of the distribution function
$\tilde{F}$	$[m^{-3}]$	perturbation part of the distribution function
$\tilde{F}_0$	$[m^{-3}]$	perturbation amplitude of the distribution function

$m$	[kg]	general particle mass
$m_e$	[kg]	electron mass
$m_i$	[kg]	ion mass
$m_D$	[kg]	deuterium mass
$q$		safety factor
$e$	[Coulomb]	electron charge
$T$	[KeV]	plasma temperature
$T_e$	[KeV]	electron temperature
$T_i$	[KeV]	ion temperature
$\tau_E$	[s]	energy confinement time
$\tau_e$	[s]	decay time of a turbulence eddy
$\tau_d$	[s]	characteristic time of viscous dissipation
$\tau$	[s]	characteristic collision time of a random walk
$\tau_{fit}$	[s]	exponential decay characteristic time
$\mathbf{E}$	[Volt/m]	electric field
$E$	[J]	particle energy
$E_r$	[Volt/m]	radial electric field
$\mathbf{B}$	[T]	magnetic field
$\mathbf{b}$		unit vector in the direction of $\mathbf{B}$
$\parallel$ and $\perp$		parallel and perpendicular to $\mathbf{b}$
$\theta$ and $\phi$		toroidal and poloidal directions in a tokamak
$B_0$	[T]	magnetic field in the plasma center
$\mathbf{v}$	[m/s]	particle velocity
$\mathbf{v}_{E \times B}$	[m/s]	$E \times B$ drift velocity
$\mathbf{v}_{\nabla B}$	[m/s]	$\nabla B$ drift velocity

$v_{curv}$	[m/s]	curvature drift velocity
$v_{ware}$	[m/s]	ware pinch inward drift velocity
$v_t$	[m/s]	general particle thermal velocity
$v_{th,e}$	[m/s]	electron thermal velocity
$v_{th,i}$	[m/s]	ion thermal velocity
$v_e$	[m/s]	characteristic flow velocity of a turbulence eddy
$v_\phi$	[m/s]	impurity toroidal velocity
$V$	[m <sup>3</sup> ]	volume of a flux surface
$c$	[m/s]	light speed
$\Delta x$	[m]	mean free path length of a random walk
$\Delta_b$	[m]	banana orbit width
$\Delta$	[m]	eddy radial size
$\rho$	[m]	general particle gyro-radius
$\rho_0$	[kg/m <sup>3</sup> ]	plasma mass density
$\rho$		normalized square root of each flux surface
		when shown as axis label in figures
$\rho_e$	[m]	electron gyro-radius
$\rho_s$	[m]	ion gyro-radius
$\rho_\theta$	[m]	gyro-radius in poloidal field
$D$	[m <sup>2</sup> /s]	particle diffusion coefficient
$D_{eff}$	[m <sup>2</sup> /s]	effective diffusion coefficient
$D_{NC}$	[m <sup>2</sup> /s]	neoclassical particle diffusion coefficient
$D_{e\text{lectron}}$	[m <sup>2</sup> /s]	electron diffusion coefficient
$D_{i\text{on}}$	[m <sup>2</sup> /s]	ion diffusion coefficient
$D_n$	[m <sup>2</sup> /s]	diagonal particle diffusion coefficient

$D_T$	$[m^2/s]$	thermal diffusion coefficient
$D_v$	$[m^2/s]$	roto-diffusion coefficient
$\chi_T$	$[m^2/s]$	energy diffusion coefficient
$\chi_{v'}$	$[m^2/s]$	momentum diffusion coefficient
$v_p$	$[m/s]$	pure convection coefficient
$\nu$	$[s^{-1}]$	collisional scattering frequency
$\nu^*$		normalized collisionality
$\nu_{ei}$	$[s^{-1}]$	electron-ion collisional frequency
$\nu$	$[s^{-1}]$	collisional scattering frequency
$\nu_{eff}$		effective plasma collisionality
$\mu$	$[J/T]$	magnetic moment
$\mu_{vis}$	$[m^2/s]$	kinematic viscosity.
$\frac{R}{L_n}$		normalized electron density gradient
$\frac{R}{L_{Te}}$		normalized electron temperature gradient
$\frac{R}{L_{Ti}}$		normalized ion temperature gradient
$ln\Lambda$		dimensionless plasma parameter
$Z_i$		impurity charge number
$p$	$[Pa]$	plasma pressure
$P_i$	$[Pa]$	ion plasma pressure
$P_I$	$[J]$	power of incident laser beam
$I_B$	$[Watt]$	Black Body radiation intensity
$\lambda_I$	$[m]$	incident beam wave length
$\nabla\lambda_{1/e}$	$[m]$	half width of spectrum
$f$	$[Hz]$	wave frequency
$f_{pe}$	$[Hz]$	plasma oscillation frequency

$\lambda$	[m]	scattered beam wave length
$g$	[ $m/s^2$ ]	gravity
$L$	[m]	Characteristic length of inhomogeneity
$L_{mach}$	[m]	tokamak machine size
$d$	[m]	crystal lattice size
$f_t$		fraction of trapped particle
$S$	[ $m^{-3}s^{-1}$ ]	particle source rate
$S_i$	[ $m^{-3}s^{-1}$ ]	ion source rate
$\beta_N$		normalized plasma pressure
$I_p$	[A]	plasma
$\mathbf{J}$	[ $C/m^2$ ]	current density
$J_0$		zero order Bessel function

## BIBLIOGRAPHY

- [1] J. Lawson. Some criteria for a power producing thermonuclear reactor. *Proceedings of the Physical Society. Section B*, 70(1):6–10, 1957.
- [2] U. S. Energy Information Administration. *Annual energy outlook 2015. DOE/EIA-0383(2015)*. U. S. Department of Energy, 2015.
- [3] R. K. Pachauri and L. A. Meyer, editors. *Climate change report 2014: synthesis report*. International Panel on Climate Change, 2014.
- [4] Carbon Dioxide Information Analysis Center. Global Carbon Project. Technical report, Oak Ridge National Lab, 2015.
- [5] Gail Tverberg. Is it really possible to decouple GDP growth from energy growth? *Our Finite World*, Nov 15, 2011.
- [6] U. S. Energy Information Administration. *International energy outlook 2014. DOE/EIA-0484(2014)*. U. S. Department of Energy, 2014.
- [7] Report by the Director General. *The Fukushima Daiichi Accident*. International Atomic Energy Agency, 2014.
- [8] M. Wald. Nuclear 'Renaissance' is short on largess. *The New York Times*, Dec 7, 2010.
- [9] C. Abernethy. NRC approves vogtle reactor construction - first new nuclear plant approvla in 34 years. *Nuclear Street*, Feb 9, 2012.

- [10] International Atomic Energy Agency. Issues relating to safety standards on geological disposal of radiative waste. *Proceedings of a specialists meeting held in Vienna*, IAEA-TECDOC-1282, 2001.
- [11] I. Cook, G. Marbach, L. Di. Pace, C. Girard, and N. P. Taylor. Safety and environmental impact of fusion. *European Fusion Development Agreement report*, EFDA-S-RE-1, 2001.
- [12] W. M. Stacey. *Fusion: an introduction to the physics and technology of magnetic confinement fusion*. Wiley-VCH, 1984.
- [13] Y. Horibe and N. Ogura. deuterium content as a parameter of water mass in the ocean. *Journal of Geophysical Research*, 73:4, 1968.
- [14] International Atomic Energy Agency. Vienna Standard Mean Ocean Water 2 (VS-MOW2) . *Reference sheet for International Measurement Standards*, 2009.
- [15] Oak Ridge National Laboratory. *Transportation energy data book*. U. S. Department of Energy, 2015.
- [16] R. Dendy. *Plasma Dynamics*. Oxford University Press, 1990.
- [17] E. Teller. *Fusion*. New York Academic Press, 1981.
- [18] J. D. Lindl. *Inertial confinement Fusion*. AIP Press, New York, Springer, 1998.
- [19] J. L. Luxon. A design retrospective of the DIII-D tokamak. *Nuclear Fusion*, 42(5):614, 2002.
- [20] G. M. Staebler, J. E. Kinsey, and R. E. Waltz. Gyro-Landau fluid equations for trapped and passing particles. *Physics of Plasmas*, 12:102508, 2005.

- [21] X. Wang, S. Mordijk, L. Zeng, L. Schmitz, T. L. Rhodes, E. J. Doyle, R. Groebner, O. Meneghini, G. M. Staebler, and S. P. Smith. Turbulent particle transport as a function of toroidal rotation in DIII-D H-mode plasmas. *Plasma Physics and Controlled Fusion*, 58:045026, 2016.
- [22] E. Fable, C. Angioni, and O. Sauter. The role of ion and electron electrostatic turbulence in characterizing stationary particle transport in the core of tokamak plasmas. *Plasma Physics and Controlled Fusion*, 52:015007, 2010.
- [23] C. Angioni, R. M. McDermott, F. J. Casson, E. Fable, A. Bortolon, R. Dux, R. Fischer, Y. Podoba, T. Putterich, F. Ryter, E. Viezzer, and ASDEX Upgrade Team. Intrinsic toroidal rotation, density peaking, and turbulence regimes in the core of tokamak plasmas. *Physics Review Letters*, 107:215003, 2011.
- [24] C. Angioni, A.G. Peeters, X. Garbet, A. Manini, F. Ryter, and ASDEX Upgrade Team. Density response to central electron heating: theoretical investigations and experimental observations in ASDEX Upgrade. *Nuclear Fusion*, 44(8):827, 2004.
- [25] Z. S. Hartwig and Y. A. Podpaly. *Magnetic fusion energy formular*. Massachusetts Institute of Technology, Cambridge, Massachusetts, USA, 2011.
- [26] R. O. Dendy. *Plasma Physics: An Introductory Course*. Cambridge University Press, 1995.
- [27] F. L. Hilton and R. D. Hazeltine. Theory of plasma transport in toroidal confinement systems. *Reviews of Modern Physics*, 48:239, 1976.
- [28] S. J. Wukitch, R. L. Boivin, P. T. Bonoli, C. L. Fiore, R. S. Granetz, M. J. Greenwald, A. E. Hubbard, I. H. Hutchinson, Y. In, J. Irby, Y. Lin, E. S. Marmar, D. Mossessian, M. Porkolab, G. Schilling, J. E. Rice, J. A. Snipes, S. M. Wolfe, and the Alcator

- C-Mod group. Double transport barrier experiments on Alcator C-Mod. *Physics of Plasmas*, 9:5, 2002.
- [29] A. A. Ware. Pinch effect for trapped particles in a tokamak. *Physics Review Letters*, 25(1), 1970.
- [30] J. Stober, C. Fuchs, O. Gruber, M. Kaufmann, B. Kurzan, F. Meo, H. W. Muller, F. Ryter, and ASDEX Upgrade Team. Dependence of the density shape on the heat flux profile in ASDEX Upgrade high density H-modes. *Nuclear Fusion*, 41:11, 2001.
- [31] J. Stober, R. Dux, O. Gruber, L. Horton, P. Lang, R. Lorenzini, C. Maggi, F. Meo, R. Neu, J. M. Noterdaeme, A. Peeters, G. Pereverzev, F. Ryter, A. C. C. Sips, A. Stabler, H. Zohm, and the ASDEX Upgrade Team. Dependence of particle transport on heating profiles in ASDEX Upgrade. *Nuclear Fusion*, 43:1265, 2003.
- [32] D. R. Ernst, P. T. Bonoli, P. J. Catto, W. Dorland, C. L. Fiore, R. S. Granetz, M. Greenwald, A. E. Hubbard, M. Porkolab, M. H. Redi, J. E. Rice, K. Zhurovich, and the Alcator C-Mod Group. Role of trapped electron mode turbulence in internal transport barrier control in the Alcator C-Mod Tokamak. *Physics of Plasmas*, 11:5, 2004.
- [33] R. Sabot, F. Clairet, G. D. Conway, L. Cupido, X. Garbet, G. Falchetto, T. Gerbaud, S. Hacquin, P. Hennequin, S. Heuraux, C. Honore, G. Leclert, L. Meneses, A. Sirinelli, L. Vermare, and A. True. Recent results on turbulence and MHD activity achieved by reflectometry. *Plasma Physics and Controlled Fusion*, 48:B421, 2006.
- [34] F. Wagner and U. Stroth. Transport in toroidal devices – the experimentalist's view. *Plasma Physics and Controlled Fusion*, 35:1321, 1993.

- [35] P. C. Efthimion, C. W. Barnes, and et al. Comparison of steady-state and perturbative transport coefficients in TFTR. *Physics of Fluids B*, 3:8, 1991.
- [36] N J Lopes Cardozo. Perturbative transport studies in fusion plasmas. *Plasma Physics and Controlled Fusion*, 37(8):799, 1995.
- [37] M. Greenwald, J. L. Terry, S. M. Wolfe, S. Ejima, M. G. Bell, S. M. Kaye, and G. H. Neilson. A new look at density limits in tokamaks. *Nuclear Fusion*, 28:12, 1988.
- [38] M. Greenwald, C. Angioni, J.W. Hughes, J. Terry, and H. Weisen. Density profile peaking in low collisionality H-modes: comparison of Alcator C-Mod data to ASDEX Upgrade/JET scalings. *Nuclear Fusion*, 47(9):L26, 2007.
- [39] M. Valovic, J. Rapp, J. G. Cordey, R. Budny, D. C. McDonald, L. Garzotti, A. Kallenbach, M. A. Mahdavi, J. Ongena, V. Parail, G. Saibene, R. Sartori, M. Stamp, O. Sauter, J. Strachan, W. Suttrop, and contributors to the EFDA-JET Workprogramme. Long timescale density peaking in JET. *Plasma Physics and Controlled Fusion*, 44:1911, 2002.
- [40] T. H. Osborne, A. W. Leonard, M. A. Mahdavi, M. Chu, M. E. Fenstermacher, R. La Haye, G. McKee, T. W. Petrie, E. Doyle, G. Staebler, M. R. Wade, and The DIII-D Team. Gas puff fueled H-mode discharges with good energy confinement above the Greenwald density limit on DIII-D. *Physics of Plasmas*, 8:5, 2001.
- [41] M. A. Mahdavi, T. H. Osborne, A. W. Leonard, M. S. Chu, E. J. Doyle, M. E. Fenstermacher, G. R. McKee, G. M. Staebler, T. W. Petrie, M. R. Wade, S. L. Allen, J. A. Boedo, N. H. Brooks, R. J. Colchin, T. E. Evans, C. M. Greenfield, G. D. Porter, R. C. Isler, R. J. L. Haye, C. J. Lasnier, R. Maingi, R. A. Moyer, M. J. Schaffer, P. G. Stangeby, J. G. Watkins, W. P. West, D. G. Whyte, and N. S. Wolf.

- High performance H mode plasma at density above the Greenwald limit. *Nuclear Fusion*, 42:52, 2002.
- [42] T. A. Carter, D. Schaffner, B. Friedman, J. Hillesheim, W. A. Peebles, G. Rossi, M. V. Umansky, D. Guice, S. Vincena, J. E. Maggs, L. Schmitz, and DIII-D team. Flow, turbulence and transport in laboratory plasmas. Department of Physics and Astronomy, UCLA.
- [43] P. W. Terry. Suppression of turbulence and transport by shear flow. *Reviews of Modern Physics*, 72:109, 2000.
- [44] A. White. Measurements of plasma turbulence in tokamaks. In *Symposium on Laboratory Astrophysics at the CfA*, April 26, 2013.
- [45] H. Biglari, P. H. Diamond, and P. W. Terry. Influence of sheard poloidal rotation on edge turbulence. *Physics of Fluids B*, 2(1):1–4, 1990.
- [46] E. J. Doyle, C. L. Rettig, K. H. Burrell, P. Gohil, R. J. Groebner, T. K. Kurki-Suonio, R. J. La Haye, R. A. Moyer, T. H. Osborne, W. A. Peebles, R. Philipona, T. L. Rhodes, T. S. Taylor, and J. G. Watkins. Turbulence and transport reduction mechanisms in the edge and interior of DIII-D H-mode plasmas. *Plasma Physics and Controlled Fusion*, 1:235, 1993.
- [47] Ch. P. Ritz, H. Lin, T. L. Rhodes, and A. J. Wootton. Evidence for confinement improvement by velocity-shear suppression of edge turbulence. *Physics Review Letters*, 65:20, 1990.
- [48] R. E. Waltz, G. D. Kerbel, and J. Milovich. Toroidal gyro-Landau fluid model turbulence simulations in a nonlinear ballooning mode representation with radial modes. *Physics of Plasmas*, 1:2229, 1994.

- [49] K. H. Burrell. Effects of ExB velocity shear and magnetic shear on turbulence and transport in magnetic confinement devices. *Physics of Plasmas*, 4:1499, 1997.
- [50] T. S. Hahm and K. H. Burrell. Flow shear induced fluctuation suppression in finite aspect ratio shaped tokamak plasma. *Physics of Plasmas*, 2:1648, 1995.
- [51] J. Weiland. *Collective modes in inhomogeneous plasma:kinetic and advanced fluid theory*. Bristol, UK; Philadelphia: Institute of physics, c2000, 2000.
- [52] G. W. Hammett. The ion temperature gradient (ITG) instability. In *CMPD/CMSO winter school, UCLA*, Jan. 09, 2007.
- [53] A. A. Vlasov. the vibrational properties of an electron gas. *Soviet Physics Uspekhi*, 10:721, 1968.
- [54] M. Henon. Vlasov equation. *Astronomy and Astrophysics*, 114:211, 1982.
- [55] Thomas M. Antonsen Jr. and Barton Lane. Kinetic equations for low frequency instabilities in inhomogeneous plasmas. *Physics of Fluids*, 23:6, June 1980.
- [56] G. W. Hammett. Properties of ITG/TEM instabilities, and key results from GK/GF codes. In *AST559: Plasma & Fluid turbulence*, Dec. 7, 2011.
- [57] A. Casati, C. Bourdelle, X. Garbet, and F. Imbeaux. Temperature ratio dependence of ion temperature gradient and trapped electron mode instability thresholds. *Physics of Plasmas*, 15:042310, 2008.
- [58] W. Horton. Drift wave and transport. *Reviews of Modern Physics*, 71:3, 1999.
- [59] S. C. Guo and J. Weiland. Analysis of the i mode by reactive and dissipative descriptions and the effects of magnetic q and negative shear on the transport. *Nuclear Fusion*, 37:8, 1997.

- [60] S. S. Henderson, L. Garzotti, F. J. Casson, D. Dickinson, M. F. J. Fox, M. O'Mullane, A. Patel, C. M. Roach, H. P. Summers, M. Valovic, and The MAST Team. Neoclassical model and gyrokinetic analysis of time-dependent helium transport experiments on MAST. *Nuclear Fusion*, 54:093013, 2014.
- [61] C. Angioni, E. Fable, M. Greenwald, M. Maslov, A. G. Peeters, H. Takenaga, and H. Weisen. Particle transport in tokamak plasmas, theory and experiment. *Plasma Physics and Controlled Fusion*, 51:124017, 2009.
- [62] G. T. Hoang, C. Bourdelle, B. Pegourie, B. Schunke, J. F. Artaud, J. Bucalossi, F. Clairet, C. Fenzi-Bonizec, X. Garbet, C. Gil, R. Guirlet, F. Imbeaux, J. Lasalle, T. Loarer, C. Lowry, J. M. Travere, E. Tsitrone, and Tore Supra Team. Particle pinch with fully noninductive lower hybrid current drive in Tore Supra. *Physics Review Letters*, 90:15, 2003.
- [63] G. T. Hoang, C. Bourdelle, X. Garbet, J. F. Artaud, V. Basiuk, J. Bucalossi, F. Clairet, C. Fenzi-Bonizec, C. Gil, J. L. Segui, J. M. Travere, and E. Tsitrone. Vermare. Parametric dependence of turbulent particle transport in Tore Supra plasmas. *Physics Review Letters*, 93:13, 2004.
- [64] A. Zabolotsky, H. Weisen, and TCV Team. Observation and empirical modelling of the anomalous particle pinch in TCV. *Plasma Physics and Controlled Fusion*, 45:735, 2003.
- [65] M. Romanelli, G. T. G. T. Hoang, C. Bourdelle, C. Gormezano, E. Giovannozzi, M. Leigheb, M. Marinucci, D. Marocco, C. Mazzotta, L. Panaccione, V. Pericoli, G. Regnoli, O. Tudisco, and the FTU Team. Parametric dependence of turbulent particle transport in high density electron heated FTU plasmas. *Plasma Physics and Controlled Fusion*, 49:935, 2007.

- [66] H. Weison, A. Zabolotsky, X. Garbet, D. Mazon, L. Zabeo, C. Giroud., H. Leggate, M Valovic, K-D. Zastrow, and contributors to the JET-EFDA Workprogramme. Shear and collisionality dependences of particle pinch in JET L-mode plasmas. *Plasma Physics and Controlled Fusion*, 46:751, 2004.
- [67] R. M. McDermott, C. Angioni, R. Dux, E. Fable, T. Putterich, F. Ryter, A. Salmi, T. Tala, G. Tardini, E. Viezzer, and the ASDEX Upgrade Team. Core momentum and particle transport studies in the ASDEX Upgrade tokamak. *Plasma Physics and Controlled Fusion*, 53:124013, 2011.
- [68] C. Angioni, R.M. McDermott, E. Fable, R. Fischer, T. Ptterich, F. Ryter, G. Tardini, and the ASDEX Upgrade Team. Gyrokinetic modelling of electron and boron density profiles of H-mode plasmas in ASDEX upgrade. *Nuclear Fusion*, 51(2):023006, 2011.
- [69] S. Mordijk, X. Wang, E. J. Doyle, T. L. Rhodes, L. Schmitz, L. Zeng, G. Staebler, C. C. Petty, W-H. Ko, B. Grierson, W. Solomon, T. Tala, A. Salmi, P. H. Diamond, and G. R. McKee. Particle transport in low-collisionality H-mode plasma on DIII-D. *Nuclear Fusion*, 55:113025, 2015.
- [70] L. Cui, G. R. Tynan, P. H. Diamond, S. C. Thakur, and C. Brandt. Up-gradient particle flux in a drift wave-zonal flow system. *Physics of Plasmas*, 22:050704, 2015.
- [71] H. Weisen, I. Furno, and TCV Team. Particle transport with high power central ECH and ECCD in TCV. *Nuclear Fusion*, 41:9, 2001.
- [72] A. Zabolotsky, H. Weisen, and TCV Team. Density profile peaking in the presence of ecrh heating in TCV. *Plasma Physics and Controlled Fusion*, 48:369, 2006.
- [73] A. G. Peeters, C. Angioni, M. Apostoliceanu, G. V. Pereverzev, E. Quigley, F. Ryter, D. Strintzi, F. Jenko, U. Fahrbach, C. Fuchs, O. Gehre, J. Hobirk, B. Kurzan, C. F.

- Maggi, A. Manimi, P. J. McCarthy, H. Meister, J. Schweinzer, J. Stober, W. Suttrop, G. Tardini, and ASDEX Upgrade Team. Understanding of the density profile shape, electron heat transport and internal transport barriers observed in ASDEX Upgrade. *Nuclear Fusion*, 45:1140, 2005.
- [74] K. A. Razumova, V. F. Andreev, A. Ya. Kislov, N. A. Kirneva, S. E. Lysenko, Yu. D. Pavlov, T.V. Shafranov, the T-10 Team, A. J. H. Donne, G. M. D. Hogeweij, G. W. Spakman, R. Jaspers, the TEXTOR Team, M. Kantor, and M. Walsh. Tokamak plasma self-organized and the possibility to have the peaked density profile in ITER. *Nuclear Fusion*, 49:065011, 2009.
- [75] R. Raman, T. R. Jarboe, J. E. Menard, and M. Ono. Need for momentum injection and core fueling in reactor grade fusion plasmas. DOE plasma frontiers workshop, Virtual Town Hall, August 12, 2015.
- [76] M. J. Gouge, K. D. S. Onge, S. L. Milora, P. W. Fisher, and S. K. Combs. Fueling of ITER scale fusion plasmas. *Fusion Technol.*, 34:435, 1998.
- [77] H. Weisen, A. Zabolotsky, C. Angioni, I. Furno, X. Garbet, C. Giroud, H. Leggate, P. Mantica, D. Mazon, J. Weiland, L. Zabeo, K-D. Zastrow, and JET EFDA. Contributors. Collisionality and shear dependences of density peaking in JET and extrapolation to ITER. *Nuclear Fusion*, 45:L1, 2005.
- [78] H. Weisen, A. Zabolotsky, M. Maslov, M. Beurskens, C. Giroud, D. Mazon, and JET-EFDA contributors. Scaling of density peaking in JET H-modes and implications for ITER. *Plasma Physics and Controlled Fusion*, 48(5A):A457, 2006.
- [79] M. Maslov, C. Angioni, H. Weisen, and JET-EFDA Contributors. Density profile peaking in JET H-mode plasmas: experiments versus linear gyrokinetic predictions. *Nuclear Fusion*, 49:075037, 2009.

- [80] H. Takenaga, K. Tanaka, K. Muraoka, H. Urano, N. Oyama, Y. Kamada, M. Yokoyama, H. Yamada, T. Tokuzawa, and I. Yamada. Comparisons of density profiles in JT-60U tokamak and LHD helica plasmas with low collisionality. *Nuclear Fusion*, 48:075004, 2008.
- [81] C. Angioni, H. Weisen, O.J.W.F. Kardaun, M. Maslov, A. Zabolotsky, C. Fuchs, L. Garzotti, C. Giroud, B. Kurzan, P. Mantica, A.G. Peeters, J. Stober, the ASDEX Upgrade Team, and contributors to the EFDA-JET Workprogramme. Scaling of density peaking in H-mode plasmas based on a combined database of AUG and JET observations. *Nuclear Fusion*, 47(9):1326, 2007.
- [82] C. Angioni, Y. Camenen, F. J. Casson, E. Fable, R. M. McDermott, A. G. Peeters, and J. E. Rice. Off-diagonal particle and toroidal momentum transport: a survey of experimental, theoretical and modelling aspects. *Nuclear Fusion*, 52:114003, 2012.
- [83] X. Garbet, P. Mantica, C. Angioni, E. Asp, Y. Baranov, C. Bourdelle, and et al. Physics of transport in tokamak. *Plasma Physics and Controlled Fusion*, 46:B557, 2004.
- [84] T. Hein, C. Angioni, E. Fable, and J. Candy. Gyrokinetic study of the role of beta on electron particle transport intokamaks. *Physics of Plasmas*, 17:102309, 2010.
- [85] E. Fable, C. Angioni, and O. Sauter. Gyrokinetic calculations of steady state particle transport in electron internal transport barriers. *Plasma Physics and Controlled Fusion*, 50:115005, 2008.
- [86] A. G. Peeters, C. Angioni, A. Bortolon, Y. Camenen, F. J. Casson, B. Duval, L. Fiederspiel, W. A. Hornsby, Y. Idomura, T. Hein, N. Kluy, P. Mantica, F. I. Parra, A. P. Snodin, G. Szepesi, D. Strintzi, T. Tala, G. Tardini, P. de Vries, and

- J. Weiland. Overview of toroidal momentum transport. *Nuclear Fusion*, 51:094027, 2011.
- [87] F. Sommer, J. Stober, C. Angioni, E. Fable, M. Bernert, A. Burckhart, V. Bobkov, R. Fischer, C. Fuchs, R. M. McDermott, W. Suttrop, E. Viezzer, and the ASDEX Upgrade Team. Transport properties of H-mode plasmas with dominant electron heating in comparison to dominant ion heating at ASDEX Upgrade. *Nuclear Fusion*, 55:033006, 2015.
- [88] X. Garbet, L. Garzotti, P. Mantica, H. Nordman, M. Valovic, H. Weisen, and C. Angioni. Turbulent particle transport in magnetized plasmas. *Physics Review Letters*, 91:035001, 2003.
- [89] Y. Camenen, A. G. Peeters, C. Angioni, F. J. Casson, W. A. Hornsby, A. P. Snodin, and D. Strintzi. Impact of the background toroidal rotation on particle and heat transport in tokamak plasmas. *Physics of Plasmas*, 16:012503, 2009.
- [90] F. J. Casson, R. M. McDermott, C. Angioni, Y. Camenen, R. Dux, E. Fable, R. Fischer, B. Geiger, P. Manas, L. Menchero, G. Tardini, and the ASDEX Upgrade Team. Validation of gyrokinetic modelling of light impurity transport including rotation in ASDEX Upgrade. *Nuclear Fusion*, 53:063026, 2013.
- [91] G. M. Staebler, J. E. Kinsey, and R. E. Waltz. A theory-based transport model with comprehensive physics. *Physics of Plasmas*, 14(055909), 2007.
- [92] H. St. John. Equations and associated definitions used in onetwo. ONETWO code documentation.
- [93] W. W. Pfeiffer, R. H. Davidson, R. L. Miller, and R. E. Waltz. *ONETWO: a*

- computer code for modeling plasma transport in tokamaks.* General Atomic Project 3235, 1980.
- [94] H. Grad and H. Rubin. Hydromagnetic equilibrium and force-free fields. *Proceedings of the 2nd UN conference. On the peaceful use of Atomic Energy. Geneva: IAEA*, 31:190, 1958.
- [95] V. D. Shafranov. Plasma equilibrium in a magnetic field. *Reviews of Plasma Physics*, 2:103, 1966.
- [96] R. H. Fowler, J. A. Holmes, and J. A. Rome. *NFREYA: a Monte Carlo beam deposition code for noncircular tokamak plasmas.* Oak Ridge National Lab, TN (USA). ORNL/TM-6845. TRN: 79-018994, 1979.
- [97] A. Pankin, D. McCune, R. Andre, and et al. The tokamak Monte Carlo fast ion module NUBEAM in the national transport code collaboration library. *Computer Physics Communications*, 159:157, 2004.
- [98] G. W. Hammett and F. W. Perkins. Fluid moment models for Landau damping with application to the ion-temperature-gradient instability. *Physics Review Letters*, 64:3019, 1990.
- [99] R. E. Waltz, R. R. Dominguez, and G. W. Hammett. Gyro-Landau fluid models for toroidal geometry. *Physics of Fluids B*, 4:3138, 1992.
- [100] R. E. Waltz, G. D. G. D. Kerbel, Milovich, and G. W. Hammett. Advances in the simulation of toroidal gyro-Landau fluid model turbulence. *Physics of Plasmas*, 2:2408, 1995.
- [101] M. A. Beer and G. W. Hammett. Toroidal gyrofluid equations for simulations of tokamak turbulence. *Physics of Plasmas*, 3:4046, 1996.

- [102] M. A. Beer and G. W. Hammett. Bounce averaged trapped electron fluid equations for plasma turbulence. *Physics of Plasmas*, 3:4018, 1996.
- [103] R. E. Waltz, G. M. Staebler, W. Dorland, G. W. Hammett, M. Kotschenreuther, and J. A. Konings. A gyro-Landau-fluid transport model. *Physics of Plasmas*, 4:2482, 1997.
- [104] J. Candy and R. E. Waltz. An Eulerian gyrokinetic-Maxwell solver. *Journal of Computational Physics*, 186:545–581, 2003.
- [105] G. M. Staebler and J. E. Kinsey. Electron collisions in the trapped gyro-Landau fluid transport model. *Physics of Plasmas*, 17:122309, 2010.
- [106] S. P. Hirshman and D. J. Sigmar. Approximate Fokker-Planck collision operator for transport theory applications. *Physics of Fluids*, 19:1532, 1976.
- [107] G. M. Staebler, J. E. Kinsey, E. A. Belli, J. Candy, R. E. Waltz, C. M. Greenfield, L. L. Lao, S. P. Smith, B. A. Grierson, and C. Chrystal. Resolving the mystery of transport within internal transport barriers. *Physics of Plasmas*, 21:055902, 2014.
- [108] J. R. Danielson. *Measurement of Landau damping of electron plasma waves in the linear and trapping regimes*. PhD thesis, Univeristy of California, San Diego, 2002.
- [109] T. O’Neil. Collisionless damping of nonlinear plasma oscillations. *Physics of Fluids*, 8:2255, 1965.
- [110] R. L. Miller, M. S. Chu, J. M. Greene, Y. R. Lin-Liu, and R. E. Waltz. Noncircular, finite aspect ratio, local equilibrium model. *Physics of Plasmas*, 5:4, 1998.
- [111] J. A. Wesson. *Tokamak, 2nd edition*. Oxford University Press, 1997.

- [112] I. H. Hutchinson. *Principles of plasma diagnostics.* Cambridge University Press, 1987.
- [113] N. C. Luhmann. Jr and W. A. Peebles. Instrumentation for magnetically confined fusion plasma diagnostics. *Review of Scientific Instruments*, 55:279, 1984.
- [114] D. M. Ponce-Marquez, B. D. Bray, T. M. Deterly, C. Liu, and D. Eldon. Thomson scattering diagnostic upgrade on DIII-D. *Review of Scientific Instruments*, 81:10D525, 2010.
- [115] A. C. Selden. Simple analytical form of the relativistic thomson scatering spectrum. *Physics Letters*, 79A:405, 1980.
- [116] T. N. Carlstrom, G. L. Campbell, J. C. DeBoo, R. Evanko, J. Evans, C. M. Greenfield, J. Haskovec, C. L. Hsieh, E. McKee, R. T. Snider, R. Stockdale, P. K. Trost, and M. P. Thomas. Design and operation of the multipulse thomson scattering diagnostic on DIII-D. *Review of Scientific Instruments*, 63:4901, 1992.
- [117] T. N. Carlstrom, C. L. Hsieh, R. Stockdale, D. G. Nilson, and D. N. Hill. Initial operation of the divertor thomson scattering diagnostic on DIII-D. *Review of Scientific Instruments*, 68:1195, 1997.
- [118] E Mazzucato. Microwave reflectometry for magnetically confined plasmas. *Review of Scientific Instruments*, 69:2201, 1998.
- [119] H. J. Hartfuss, T. Geist, and M. Hirsch. Heterodyne methods in millimeter wave plasma diagnostics with application to ECE, interferometry and reflectometry. *Plasma Physics and Controlled Fusion*, 39:1693, 1997.
- [120] L. Zeng, G. Wang, E. J. Doyle, T. L. Rhodes, W. A. Peebles, and Q. Peng. Fast au-

- tomated analysis of high-resolution reflectometer density profiles on DIII-D. *Nuclear Fusion*, 46:S677, 2006.
- [121] A. E. Costley, R. J. Hastie, J. W. M. Paul, and J. Chamberlain. Electron cyclotron emission from a tokamak plasma: experiment and theory. *Physics Review Letters*, 33:758, 1974.
- [122] M. Bornatici, R. Cano, O. de Barbiere, and F. Engelmann. Electron cyclotron emission and absorption in fusion plasmas. *Nuclear Fusion*, 23:1153, 1983.
- [123] D. D. Truong and M. E. Austin. High spatial resolution upgrade of the electron cyclotron emission radiometer for DIII-D tokamak. *Review of Scientific Instruments*, 85:11D814, 2014.
- [124] R. J. Groebner, N. H. Brooks, K. H. Burrell, and L. Rottler. Measurements of plasma ion temperature and rotation velocity using the He II 4686-A line produced by charge transfer. *Applied Physics Letters*, 43:920, 1983.
- [125] R. P. Seraydarian, K. H. Burrell, N. H. Brooks, R. J. Groebner, and C. Kahn. Multichordal charge exchange recombination spectroscopy on the Doublet III tokamak. *Review of Scientific Instruments*, 57:155, 1986.
- [126] R. C. Isler. An overview of charge-exchange spectroscopy as a plasma diagnostic. *Plasma Physics and Controlled Fusion*, 36:171, 1994.
- [127] G. McKee, R. Ashley, R. Durst, R. Fonck, M. Jakubowski, and K. Tritz. The beam emission spectroscopy diagnostic on DIII-D tokamak. *Review of Scientific Instruments*, 70:913, 1999.
- [128] W. Mandl, R. C. Wolf, M. G. von Hellermann, and H. P. Summers. Beam emis-

- sion spectroscopy as a comprehensive plasma diagnostic tool. *Plasma Physics and Controlled Fusion*, 35:1373, 1993.
- [129] J. C. Hillesheim, W. A. Peebles, T. L. Rhodes, L. Schmitz, T. A. Carter, P. A. Gourdain, and G. Wang. A multichannel, frequency-modulated, tunable Doppler backscattering and reflectometry system. *Review of Scientific Instruments*, 80:083507, 2009.
- [130] E. Holzhauer, M. Hirsch, T. Grossmann, B. Branas, and F. Serra. Theoretical and experimental investigation of the phase-runaway in microwave reflectometry. *Plasma Physics and Controlled Fusion*, 40:1869, 1998.
- [131] M. Hirsch, E. Holzhauer, J. Baldzuhn, B. Kurzan, and B. Scott. Doppler reflectometry for the investigations of propagating density perturbations. *Plasma Physics and Controlled Fusion*, 43:1641, 2001.
- [132] N Aiba, J Shiraishi, and M Hirota. Impact of plasma rotation on the linear physics of resistive wall modes in tokamaks. *Plasma Physics and Controlled Fusion*, 55(7):074002, 2013.
- [133] I T Chapman, S D Pinches, J P Graves, R J Akers, L C Appel, R V Budny, S Coda, N J Conway, M de Bock, L-G Eriksson, R J Hastie, T C Hender, G T A Huysmans, T Johnson, H R Koslowski, A Krmer-Flecken, M Lennholm, Y Liang, S Saarelma, S E Sharapov, I Voitsekhouitch, the MAST, TEXTOR Teams, and JET EFDA Contributors. The physics of sawtooth stabilization. *Plasma Physics and Controlled Fusion*, 49(12B):B385, 2007.
- [134] R. Fitzpatrick and T. C. Hender. The interaction of resonant magnetic perturbations with rotating plasmas. *Physics of Fluids B: Plasma Physics (1989-1993)*, 3(3):644–673, 1991.

- [135] L. Garzotti, P. Belo, G. Corrigan, F. Kochl, J. Lonnroth, V. Parail, G. Pereverzev, S. Saarelma, G. Tardini, and M. Valovic. Simulation of density profiles, pellet fueling and density control in ITER. *Nuclear Fusion*, 52:013002, 2012.
- [136] C. Angioni, J. Candy, E. Fable, M. Maslov, A. G. Peeters, R. E. Waltz, and H. Weisen. Particle pinch and collisionality in gyrokinetic simulations of tokamak plasma turbulence. *Physics of Plasmas*, 16(6):060702, 2009.
- [137] E. J. Doyle, L. Zeng, G. M. Staebler, T. E. Evans, T. C. Luce, G. R. McKee, S. Mordijk, R. A. Moyer, W. A. Peebles, C. C. Petty, and T. L. Rhodes. Particle transport results from collisionality scans and perturbative experiments on DIII-D. In *Conference proceeding of 24th IAEA Fusion Energy Conference San Diego, USA*, 2012.
- [138] A. W. Leonard. The edge-localized-mode (ELM) in tokamaks. *55th annual APS meeting, Division of Plasma Physics*, Nov 11, 2013.
- [139] R. Scannell, A. Kirk, N. Ben Ayed, P. G. Carolan, G. Cunningham, J. McCone, S. L. Prunty, and M. J. Walsh. Experimental investigation into ELM filament formation on MAST. *Plasma Physics and Controlled Fusion*, 49:1431, 2007.
- [140] B. A. Grierson, K. H. Burrell, W. M. Solomon, and N. A. Pablant. Deuterium velocity and temperature measurement on the DIII-D tokamak. *Review of Scientific Instruments*, 81:10D735, 2010.
- [141] W. M. Solomon, K. H. Burrell, A. M. Garofalo, S. M. Kaye, R. E. Bell, A. J. Cole, J. S. deGrassie, P. H. Diamond, T. S. Hahm, G. L. Jackson, M. J. Lanctot, C. C. Petty, H. Reimerdes, S. A. Sabbagh, E. J. Strait, T. Tala, and R. E. Waltz. Mechanisms for generating toroidal rotation in tokamaks with external momentum input. *Physics of Plasmas*, 17:056108, 2010.

- [142] N. T. Howard, A. E. White, M. Greenwald, C. Holland, and J. Candy. Multi-scale gyrokinetic simulation of Alcator C-Mod tokamak discharges. *Physics of Plasmas*, 21:032308, 2014.
- [143] S. Mordijk, E. J. Doyle, G. R. McKee, R. A. Moyer, T. L. Rhodes, L. Zeng, N. Commaux, M. E. Fenstermacher, K. W. Gentle, H. Reimerdes, O. Schmitz, W. M. Solomon, G. M. Staebler, and G. Wang. Changes in particle transport as a result of resonant magnetic perturbations in DIII-D. *Physics of Plasmas*, 19:056503, 2012.
- [144] J. O'Rourke, F.G. Rimini, and D.F.H. Start. Perturbative measurements of the electron transport matrix using ICRF power modulation. *Nuclear Fusion*, 32(10):1861, 1992.
- [145] K W Gentle, G Cima, H Gasquet, G A Hallock, P E Phillips, W L Rowan, C Watts, O Gehre, and the ASDEX-U Team. Characteristics of equilibrium and perturbed transport coefficients in tokamaks. *Physica Scripta*, 52(4):411, 1995.
- [146] A. Jacchia, P. Mantica, F. De Luca, and G. Gorini. Determination of diffusive and nondiffusive transport in modulation experiments in plasmas. *Physics of Fluids B*, 3(11):3033–3040, 1991.
- [147] H. Takenaga, K. Nagashima, A. Sakasai, T. Oikawa, and T. Fujita. Determine of particle transport coefficients in reversed shear plasma of JT-60U. *Plasma Physics and Controlled Fusion*, 40:183, 1998.
- [148] A. Salmi and et al. Particle source and edge transport studies in JET H-mode gas puff modulation experiments. *41st EPS Conference*, 2015.
- [149] R. M. McDermott, B. Lipschultz, J. W. Hughes, P. J. Catto, A. E. Hubbard, I. H. Hutchinson, R. S. Granetz, M. Greenwald, B. LaBombard, K. Marr, M. L. Reinke,

- J. E. Rice, D. Whyte, and Alcator C-Mod Team. Edge radial electric field structure and its connections to H-mode confinement in Alcator C-Mod plasmasa. *Physics of Plasmas*, 16(5):056103, 2009.
- [150] N. T. Howard, A. E. White, M. L. Reinke, M. Greenwald, C. Holland, J. Candy, and J. R. Walk. Validation of the gyrokinetic model in ITG and TEM dominated L-mode plasmas. *Nuclear Fusion*, 53:123011, 2013.
- [151] A.M. Garofalo, W.M. Solomon, J.-K. Park, K.H. Burrell, J.C. DeBoo, M.J. Lanctot, G.R. McKee, H. Reimerdes, L. Schmitz, M.J. Schaffer, and P.B. Snyder. Advances towards QH-mode viability for ELM-stable operation in ITER. *Nuclear Fusion*, 51(8):083018, 2011.
- [152] K. H. Burrell, M. E. Austin, D. P. Brennan, J. C. DeBoo, E. J. Doyle, P. Gohil, C. M. Greenfield, R. J. Groebner, L. L. Lao, and T. C. Luce. Quiescent H-mode plasmas in the DIII-D tokamak. *Plasma Physics and Controlled Fusion*, 44:A253, 2002.
- [153] E. Mazzucato, S. H. Batha, M. Beer, M. Bell, R. E. Bell, R. V. Budny, C. Bush, T. S. Hahm, G. W. Hammett, F. M. Levinton, R. Nazikian, H. Park, G. Rewoldt, G. L. Schmidt, E. J. Synakowski, W. M. Tang, G. Taylor, and M. C. Zarnstorff. Turbulent fluctuations in TFTR configurations with reversed magnetic shear. *Physics Review Letters*, 77:15, 1996.
- [154] L. Schmitz, L. Zeng, T. L. Rhodes, J. C. Hillesheim, W. A. Peebles, R. J. Groebner, K. H. Burrell, G. R. McKee, Z. Yan, G. R. Tynan, P. H. Diamond, J. A. Boedo, E. J. Doyle, B. A. Grierson, C. Chrystal, M. E. Austin, W. M. Solomon, and G. Wang. The role of zonal fflow and predator-prey oscillations in triggering the formation of edge and core transport barriers. *Nuclear Fusion*, 54:073012, 2014.

- [155] The ITER project. Technical report, European Fusion Development Agreement (EFDA), 2006.
- [156] R.J. Hawryluk, D.J. Campbell, G. Janeschitz, P.R. Thomas, R. Albanese, R. Ambrosino, C. Bachmann, L. Baylor, M. Becoulet, I. Benfatto, J. Bialek, A. Boozer, A. Brooks, R. Budny, T. Casper, M. Cavinato, J.-J. Cordier, V. Chuyanov, E. Doyle, T. Evans, G. Federici, M. Fenstermacher, H. Fujieda, K. Gal, A. Garofalo, L. Garzotti, D. Gates, Y. Gribov, P. Heitzenroeder, T.C. Hender, N. Holtkamp, D. Humphreys, I. Hutchinson, K. Ioki, J. Johner, G. Johnson, Y. Kamada, A. Kavin, C. Kessel, R. Khayrutdinov, G. Kramer, A. Kukushkin, K. Lackner, I. Landman, P. Lang, Y. Liang, J. Linke, B. Lipschultz, A. Loarte, G.D. Loesser, C. Lowry, T. Luce, V. Lukash, S. Maruyama, M. Mattei, J. Menard, M. Merola, A. Minneev, N. Mitchell, E. Nardon, R. Nazikian, B. Nelson, C. Neumeyer, J.-K. Park, R. Pearce, R.A. Pitts, A. Polevoi, A. Portone, M. Okabayashi, P.H. Rebut, V. Riccardo, J. Roth, S. Sabbagh, G. Saibene, G. Sannazzaro, M. Schaffer, M. Shimada, A. Sen, A. Sips, C.H. Skinner, P. Snyder, R. Stambaugh, E. Strait, M. Sugihara, E. Tsitrone, J. Urano, M. Valovic, M. Wade, J. Wesley, R. White, D.G. Whyte, S. Wu, M. Wykes, and L. Zakharov. Principal physics developments evaluated in the ITER design review. *Nuclear Fusion*, 49:065021, 2009.
- [157] G. Bosia, K. Ioki, N. Kobaya, P. Bibet, R. Koch, R. Chavan, M. Q. Tran, K. Takahashi, S. Kuzikov, and V. Vdovin. Design of iter-feat rf heating and current drive systems. *18th IAEA Fusion Energy Conference, Sorrento, Italy.*, IAEA-CN-77:243, 2000.
- [158] P. H. Diamond, Y. Kosuga, O. D. Gurcan, C. J. McDevitt, T. S. Hahm, N. Fedorczac, J. E. Rice, W. X. Wang, S. Ku, J. M. Kwon, G. Dif-Pradalier, J. Abiteboul, L. Wang, W. H. Ko, Y. J. Shi, K. Ida, W. Solomon, H. Jhang, S. S. Kim, S. Yi,

- S. H. Ko, Y. Sarazin, R. Singh, and C. S. Chang. An overview of intrinsic torque and momentum transport bifurcations in toroidal plasmas. *Nuclear Fusion*, 53:104019, 2013.
- [159] J. Candy. Tglf recalibration for ITER standard case pparameter FY2015. Technical report, General Atomics, US Department of Energy DE-FG02-95ER54309, Dec. 2015.
- [160] F. J. Casson, C. Angioni, E. A. Belli, R. Bilato, P. Mantica, T. Odstrcil, T. Putterich, M. Valisa, L. Garzotti, C. Girard, J. Hobirk, C. F. Maggi, J. Mlynar, M. L. Reinke, JET EFDA Contributors, and ASDEX Upgrade Team. Theoretical description of heavy impurity transport and its application to the modeling of tungsten in JET and ASDEX upgrade. *Plasma Physics and Controlled Fusion*, 57:014031, 2015.
- [161] C. Angioni and P. Helander. Neoclassical transport of heavy impurities with poloidal asymmetric density distribution in tokamaks. *Plasma Physics and Controlled Fusion*, 56:124001, 2014.
- [162] J. E. Rice, A. Ince-Cushman, J. S. deGrassie, L. G. Eriksson, Y. Sakamoto, A. Scarbosio, A. Bortolon, K. H. Burrell, B. P. Duval, C. Fenzi-Bonizec, M. J. Greenwald, R. J. Groebner, G. T. Hoang, Y. Koide, E. S. Marmar, A. Pochelon, and Y. Podpaly. Inter-machine comparison of intrinsic toroidal rotation in tokamaks. *Nuclear Fusion*, 47:1618–1624, 2007.
- [163] L-G. Eriksson, E. Righi, and K-D. Zastrow. Toroidal rotation in ICRF-heated H-mode on JET. *Nuclear Fusion*, 39:27, 1997.
- [164] A. E. White, N. T. Howard, M. J. Greenwald, M. L. Reinke, C. Sung, S. Baek, M. Barnes, J. Candy, A. Domingues, D. Ernst, C. Gao, A. E. Hubbard, J. W. Hughes,

Y. Lin, D. Mikkelsen, F. Parra, M. Porkolab, J. E. Rice, J. Walk, S. J. Wukitch, and Alcator C-Mod Team. Multi-channel transport experiments at Alcator C-Mod and comparison with gyrokinetic simulations. *Physics of Plasmas*, 20:056106, 2013.

## VITA

### Xin Wang

Xin Wang grew up in Changzhou, China. He graduated from the University of Science and Technology of China in 2012 with a Bachelor of Science degree in applied physics. That same year he began his graduate studies at the College of William and Mary, where he started working with Dr. Saskia Mordijk. His research focuses on studying how different plasma conditions such as toroidal rotation or instability types can affect the turbulent particle transport in magnetic confined burning plasmas. After graduating, Xin will begin working as a Quantitative Associate at Wells Fargo.